6. Chapter 6 SIMULATING THE RAIL-REPAIR PROCESS USING FINITE ELEMENT ANALYSIS (FEA)

The repetitive experimental evaluation of all of the involved parameters until finding the optimum condition will cost a lot of materials and time. Therefore, to avoid considerable costs associated with the experimental lab tests, a finite element (FE) model is developed in which the full LPD rail repair process is simulated; further investigations on the process parameters can be conducted numerically after the thorough validation of the model.

Sec. 6.1 will describe the established FE model regarding the geometry, solution domain, and the incorporated elements and equations. Then, in Sec. 6.2, the developed FE model for repairing the light rail will be validated by comparing the calculated results against the experimental results of an LPD-repaired light rail using 304L, i.e., the results that were presented in Secs. 3.1.2, 4.1.2, and 5.1.1. At this time, the developed FE model is considered for LPD-repairing of the light rails only. The process simulation of SAW-repairing and also that for the heavy rails will be carried out in the near future.

6.1. Finite element (FE) model development

A coupled thermal-kinetic-mechanical FE model that simulates the AM rail repair process is developed. A flowchart representing the general work plan of the FE model is given in Fig. 1. For the sequential thermal-mechanical calculation, thermal calculation feeds its output to the mechanical calculation as the initial nodal thermal loads. On one hand, calculation of the thermal field for every single time step is reliant on the material properties, and on the other hand, material properties calculation at any time is dependent on the thermal field. This fact necessitates adding a thermal-kinetic calculation chain to the model, which is schematically shown as the connection between thermal and kinetic calculation in Fig. 1. The hardness and microstructure properties are updated at every time step through the user-defined relationships for microstructures and material properties. Thermal-kinetic analysis accounts for heat and mass transfer and also phase transformation, which are given to the model through a set of conjugate equations. It is indeed obvious that these equations cannot get solved via analytic methods. To attain more accurate numbers out of thermal calculation, a set of mathematical expressions are given to the model as an external user-defined subroutine, where the element activation temperature, phase transformation latent heat, and laser power attenuation are considered.

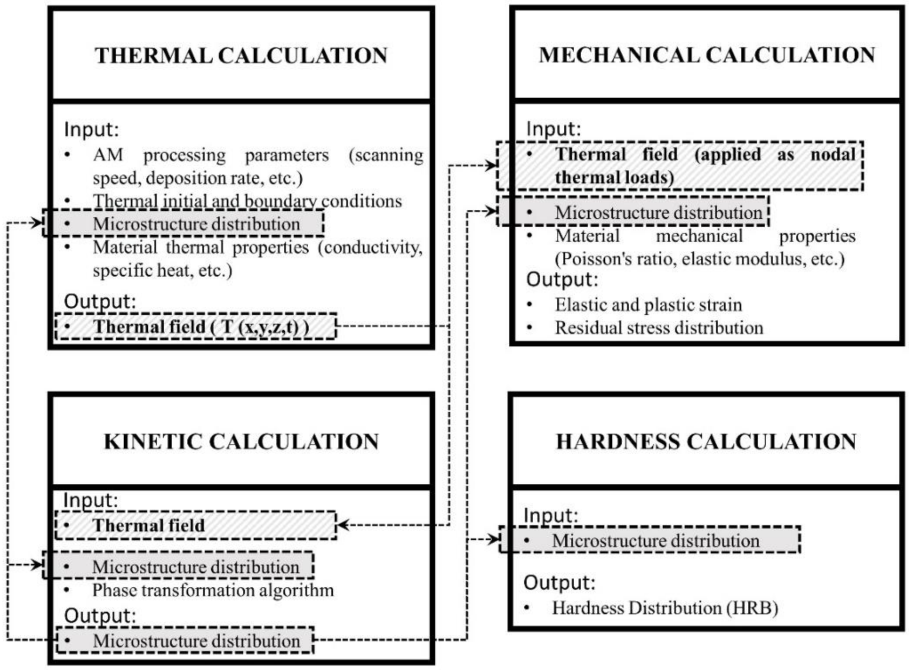

Fig. 6.1 A flowchart illustrating the designated work plan for coupled thermal-kinetic-mechanical calculations in the developed FE model for simulating AM rail repair process.

Referring to Fig. 1, the analysis cycle starts with thermal calculation. The problem solution domain along with all the initial and boundary conditions are fed to the thermal model to give the resulting T(x,y,z,t) as the output file. The thermal field outcome is inserted into the kinetic model for every single time step in order to predict the microstructure distribution. The microstructure outcome is: first, imported to the thermal model input to update the thermal problem initial values; second, given back to the kinetic calculation itself to update the input; third, put into the developed equations for hardness calculation; and fourth, along with the thermal output, is fed to the mechanical calculation input. It is evident in Fig. 1 that mechanical and hardness calculation give residual stress and hardness distribution, respectively, in the output file. All the mentioned calculations above repeat for each time step.

6.1.1. Thermal calculation

All the involved heat transfer mechanisms during the AM process should be considered in the model to attain an accurate thermal field.

The following equation calculates the conduction heat transfer:

$$\rho c \frac{\partial T}{\partial t} = \nabla . (k . \nabla \mathrm{T}) + \Gamma \tag{1}$$

where ρ, c, and k represent the density, specific heat, and conductivity, respectively, and T represents the local temperature at any specific time of t. An amount of 260 kJ/kg is considered for the latent heat of phase transformation (Γ) [1].

The bulk rail and deposition materials, as the solid domain, lose and gain heat through their interfaces with ambient. This loss/gain of heat is carried out via convection and radiation heat transfer mechanisms. Hence, the convection and radiation equations are applied as problem boundary conditions, because they occur as a result of the surface-ambient interactions.

The most important surface-ambient interaction to consider is the ultimate laser power that strikes on the surface. The ultimate laser power that reaches the substrate to create the molten pool is lower than the laser source power due to the laser power attenuation. To take this effect into consideration, the laser beam is regarded to be distributed in Gaussian form. Utilizing the analytical CFD model of Tabernero et al. [2], the ultimate laser power is expressed as:

$$P_u = \frac{2P_s}{\pi R_t^2} \times exp\left(-2\left(\frac{R_l}{R_t}\right)^2\right) \tag{2}$$

where P_u and P_s give the laser ultimate and source power, respectively. The parameter R_t is the total beam radius, while R_l gives the local radius through the following definition:

$$R_l = ((x - Vt)^2 + y^2)^{1/2} \tag{3}$$

where V is the laser travel speed. The following assumptions are made for deriving the attenuated power of the laser source:

- The powder particles shadow effect is neglected.
- Powder particles are assumed as perfect sphere of 75 µm diameter that hit the melt pool with a blowing velocity of 4 m/s.
- Based on the published data by Liu and Lin [3], for a laser power of 1.8 kW, powder diameter of 75 µm, and 4m/s blowing velocity, the percentage of the evaporated mass of powder is low enough to be neglected. Accordingly, particle evaporation is not considered here.
- Heat transfer through the carrier gas is low enough to be omitted.
- The powder distribution profile is also considered to be Gaussian based on the Lin's suggestion [4].

According to the recommended methods in [5,6], Beer-Lambert method is employed to calculate the attenuated laser power, P_a. By integrating along the stand-off distance of the laser beam, from laser aperture ((x', y') = (0, 0) in Sec. 2.2.2, Fig. 3) down to the railhead surface ((x', y') = (0, S) in Sec. 2.2.2, Fig. 3, where S = 11 mm), the following expression is established:

$$\int_{P_0}^{P_s} \frac{dP}{P} = -\epsilon \int_{0}^{11} \left(\frac{C_m}{\pi R_{jt}^2}\right) exp\left(-2\left(\frac{R_{jl}}{R_{jt}}\right)^2\right) dy' \tag{4}$$

where R_{jl} and R_{jt} are local and total powder jet radius, respectively. The Mie's optical factor, ϵ, is equal to $\pi d_p^2/4$ (d_p is powder particle diameter), based on the recommendation from Frenk et al. [7]. C_m is the maximum powder concentration, which is formulated as:

$$C_m = \left(\frac{6\sqrt{2}}{\pi^{3/2}}\right)\left(\frac{\dot{m}}{\rho_p \nu_p d_p^3 R_{jt}}\right) \tag{5}$$

where ρ_p and ν_p represent the powder density and velocity, respectively. Powder density is considered to be of the constant value of 7955 kg/m^3 [3]. Powder feeding rate, $\dot{m}$, is defined as:

$$\dot{m} = \frac{\pi}{6}\left(d_p^3 \rho_p \nu_p\right) \int_{-\infty}^{\infty} \left(\frac{C_m}{\pi R_{jt}^2}\right) exp\left(-2\left(\frac{R_{jl}}{R_{jt}}\right)^2\right) dR_{jl} \quad (6).$$

Relying on the outcomes of Liu and Lin [3], it can be logically assumed that the powder particles will not melt before joining the melt pool. Another presumed fact is that if any powder particle does not successfully enter the melt pool, it will be rebounded or driven away, i.e., none of the powder particles will adhere on the bed surface. Melt pool temperature is estimated as equal to the railhead's liquidus temperature, T_{liq}. Thus, the powder particles melt and reach T_{liq} right at the moment of their entrance into the melt pool. Consequently, the ultimate laser power that hits the substrate is developed as follows:

$$P_u = \alpha_{sub}\left(\frac{2P_s}{\pi R_t^2} \times exp\left(-2\left(\frac{R_l}{R_t}\right)^2\right) - P_a\right) - \frac{\eta \dot{m}}{\pi R_t^2}\left(\Gamma + \bar{c}\left(T_{liq} - T_p\right)\right) \tag{7}$$

where α_{sub} stands for the substrate absorptivity, η gives the powder efficiency, and $\bar{c}$ represents the average specific heat of the powder particles, which is considered equal to 740 J/kg°C. For the immediate temperature of powder particles before entering the molten pool, T_p, an average value of 224°C is taken into account [6]. Solution of the numerical integrals in Eqs. 4 and 7 gives the Gaussian power distribution of both the laser source and ultimate laser power, which is shown in Fig. 2. It is hence concluded based on the figure that an average amount of 130 W of the laser source power is attenuated, i.e., P_a = 130 W. In this way, thermal problem boundary condition can be defined as:

$$-k(\nabla \mathrm{T}.\vec{n}) = P_u - U(T - T_a) \quad (8).$$

The term $U(T-T_a)$ expresses the total heat loss from the solid body to the ambient through convection and radiation mechanisms. The overall film coefficient, U, is equal to $2.4\times10^{-3}\varepsilon T^{1.6}$, where the value of the radiative emissivity, ε, is taken as 0.85 [6]. The ambient temperature, T_a, is 25°C.

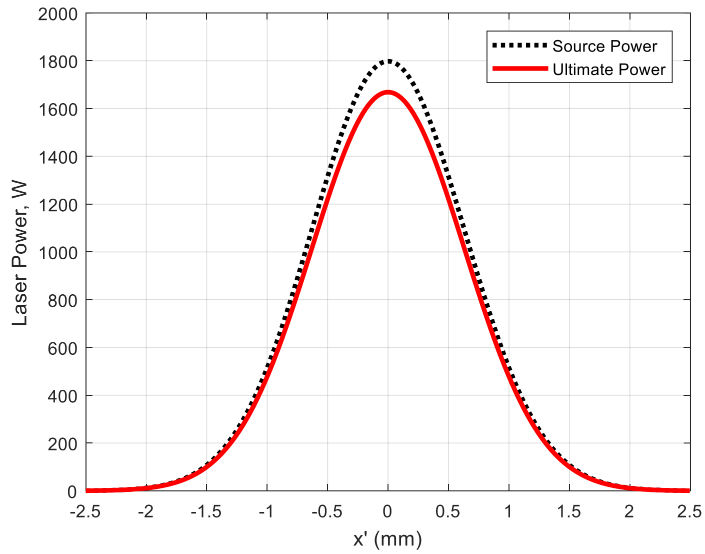

Fig. 6.2 Distribution of laser source power and laser ultimate power along the laser strike diameter at y' = S = 11 mm (refer to Sec. 2.2.2, Fig. 3 for (x',y') coordination).

In order to build up the worn part of the railhead in the FE model based on the defined LPD strategy, the element birth-and-kill technique is incorporated. The steps involved in this technique are described as follows:

a) Modeling the solution domain, including worn rail geometry and the deposition part (Fig. 3a).
b) Discretizing the solution domain into finite elements (Fig. 3b). The employed three-dimensional solid element is the 10-node coupled field type, referred to as "SOLID227" in ANSYS. The element mesh mapping of the deposition domain is done manually in order to scrutinize the 50% overlap of the adjacent clads.
c) Deactivating, i.e., killing, the deposition domain at the beginning (Fig. 3c). In this step, all of the elements of the deposition domain are deactivated at t = 0. Therefore, the problem is initiated with a sole worn rail, the initial temperature of which is defined as:

$$T(x, y, z, t = 0) = T_i \tag{9a}$$

where, based on the selected preheating case, T_i has various values. In this study, in order to investigate the effect of bed preheating on residual stresses, five different cases are examined, i.e., T_i = 25°C (no preheating), 400°C, 600°C, 800°C, and 900°C. The model will be verified based on the no-preheating condition (T_i = 25°C). Investigation of the effect of preheating will be analyzed and discussed in great details in Chapter 7.

d) Stepwise activating, i.e., bearing, the deactivated deposition elements (Fig. 3d). Here, the elements of the deposition domain start to activate at the same pace as the actual powder feeding rate. Technically, the laser power has to be high enough to melt the deposition bed, i.e., the railhead, and ensure perfect bonding. Thus, the second initial condition is to set the initial temperature of the activated elements at the melting temperature of the railhead:

$$T(x,y,z,t=t_{activation}) = T_{melt} = 1500°C \quad (9b).$$

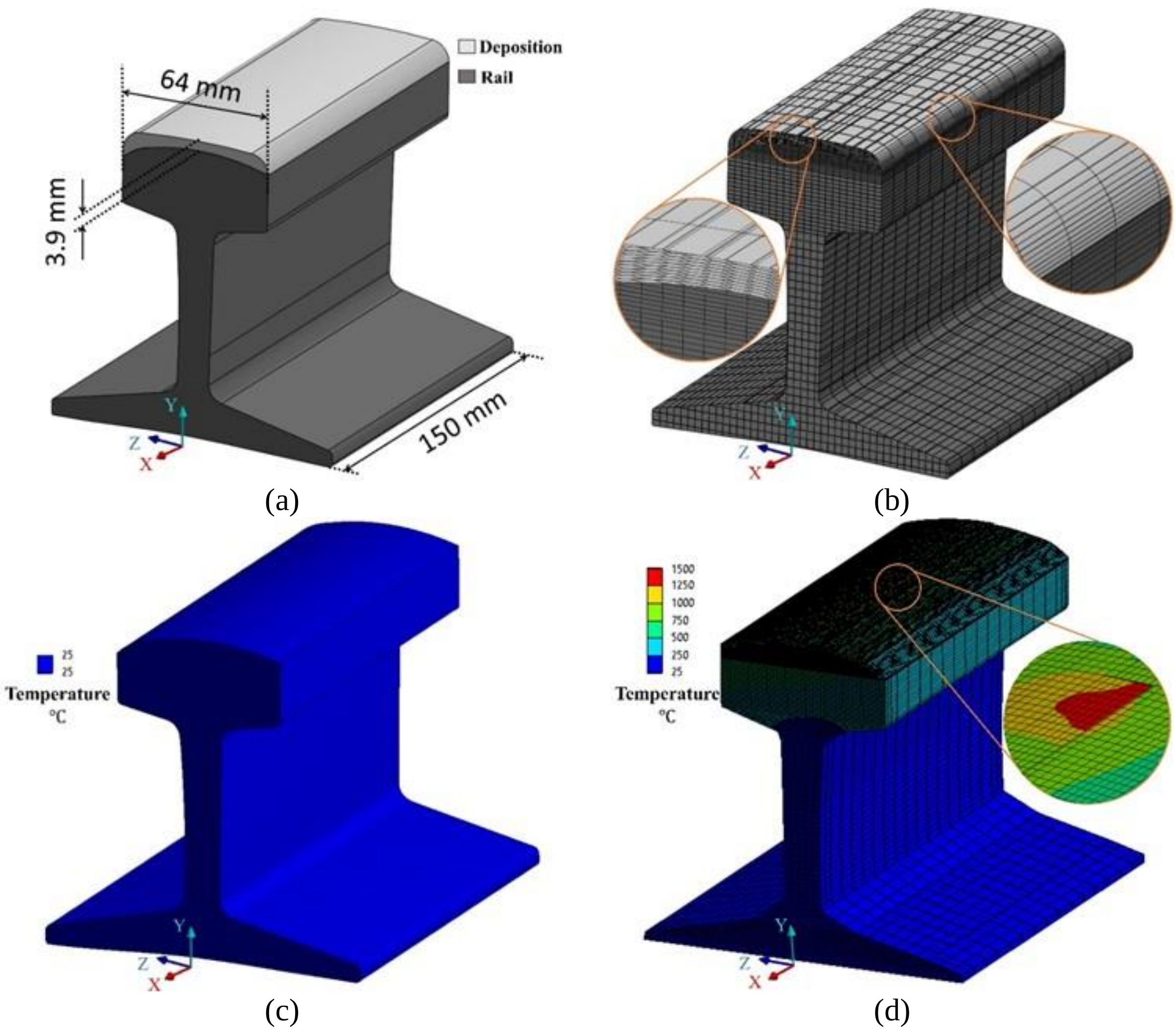

Fig. 6.3 Graphical illustration of the element-birth-and-kill method that is used to simulate the LPD process in the FE model in 4 steps, i.e., (a) modeling the solution domain, (b) discretizing the solution domain into finite elements, (c) killing the deposition elements at the beginning (here shown for the T_i = 25°C), and (d) bearing the killed deposition elements step by step.

Regarding the tool path, the laser heat source, in tandem with the element activation process, travels back and forth along the +/-x axis. There is 9s of idle time between finishing the activation of the last element of a completed deposition row and starting the activation of the first element of the consecutive row. The deposition layers are built upward along the +y axis.

As regards to guarantee the calculation accuracy with minimum computational time, a grid independence test is carried out for the thermal model. To perform this test, five grid densities are tested and the temperature parameter, T(x,y,z,t), at the very last time step right after the activation of the last deposition element (t_{final}) and two selected locations, i.e., (x,y,z) = (-50,2,0) mm and (x,y,z) = (-100,-100,0) mm (refer to Sec. 5.1.1, Fig. 1 for configuration of the coordination system), is used as the test criteria. Table 1 lists the results of the grid independence test. The Grid no. 4 with 475,646 elements and 586,592 nodes is finally picked for the numerical model. Selecting the denser Grid no. 5 with 868,023 elements and 954,825 nodes results in only ≤ 2% modification in the predicted temperature values. In the matter of the dependent variables, their residual sum are monitored after each iteration. Based on the assigned convergence criterion, the maximum relative mass residual depending on the input mass has to be lower than 10^{-4}.

Table 1 Grid Independence Test.

Grid no.	Elements	Nodes	T (-50,2,0,t_{final}) (°C)	T (-100,-100,0,t_{final}) (°C)
1	12,334	20,628	449	147
2	142,018	215,553	489	159
3	229,055	302,515	548	183
4	475,646	586,592	573	194
5	868,023	954,825	579	197

6.1.2. Kinetic calculation

Four candidate steels, including 304L stainless steel, 410L stainless steel, Stellite 6, and Stellite 21, are chosen to investigate the best option, i.e., the option in which the lowest residual stress and highest strength are attained simultaneously. The leading motivation for choosing 410L, Stellite 6, and Stellite 21 is their remarkable tribological and mechanical properties based on the reports in [8,9], which make them notably applicable for rail repair. Since the guidelines of the AREMA [10] have restricted the martensite occupation in the microstructure of any standard U.S. rail, the selection of 304L is made mainly due to its austenitic nature, which essentially allows the avoidance of martensite in the finally established microstructure of the repaired rail. It also should be noted that the other reason for selecting these four materials is that they are commercially available as powders that are specifically intended for LPD applications.

A phase-transformation paradigm for each of the four tool steels is developed and applied to the model in a way to predict the microstructural phase evolutions during the heating-cooling cycles of the LPD process. Fig. 4 shows these paradigms in the form of schematic diagrams. A brief description of the analytical procedure, through which each of the phase-transformation diagrams and the reciprocal phase-volume-fraction equations were obtained, is presented in the following.

Since 304L is an austenitic stainless steel, its Ni_{eq}-Cr_{eq} system must be authenticated first in order to determine its phase transformation procedure [11]:

$$\begin{aligned} Ni_{eq} &= 0.5(Mn) + (Ni) + 30(C + N) \\ Cr_{eq} &= 0.5(Nb) + (Cr + Mo) + 1.5(Si) \end{aligned} \tag{10}$$

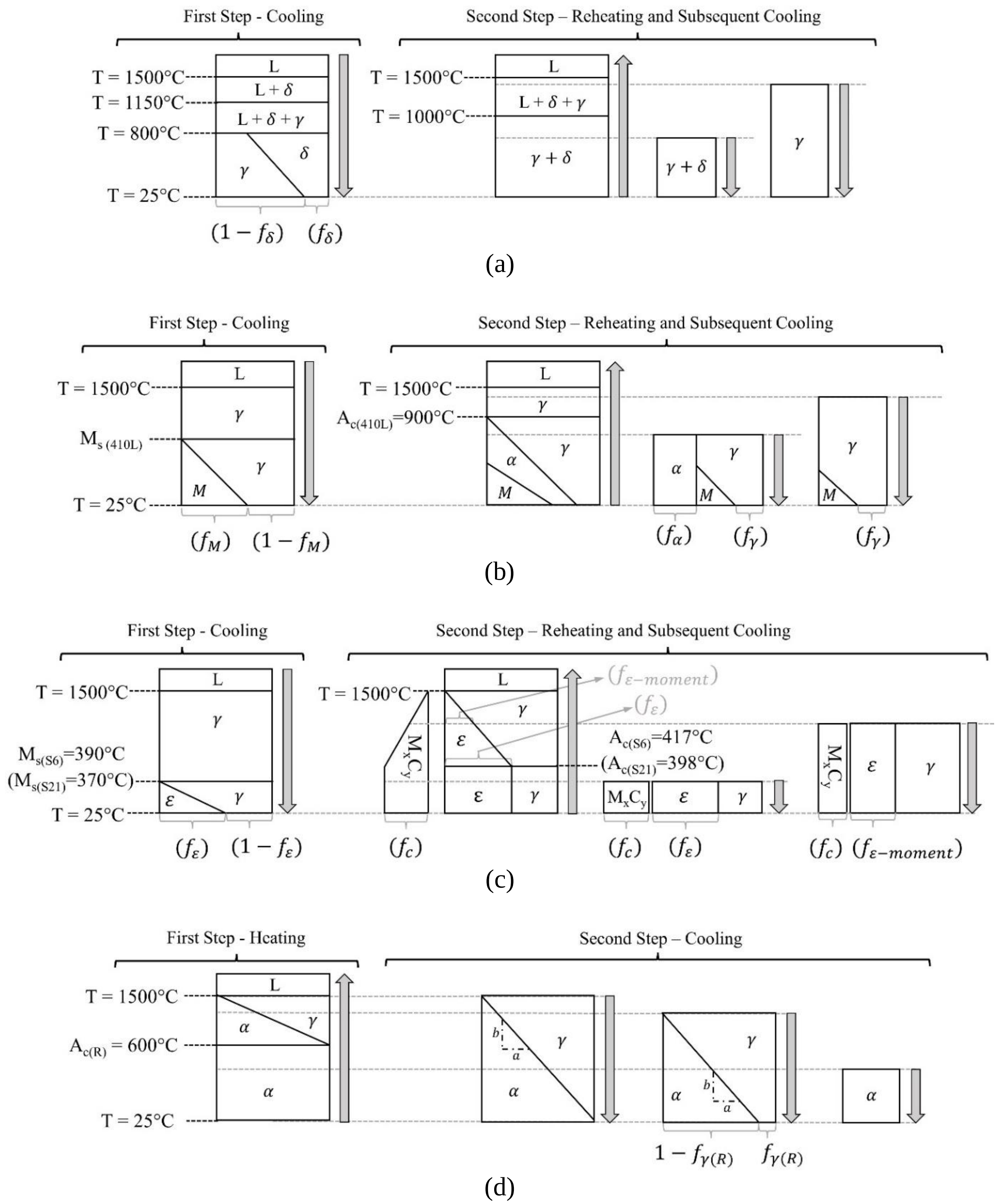

Fig. 6.4 Schematic diagrams showing the defined phase-transformation paradigms applied to the kinetic analysis of the FE model for each of the deposition tool steels, i.e., (a) 304L stainless steel and (b) 410L stainless steel, (c) Stellite 6 and Stellite 21 ($M_{s(S6)}$ and $A_{c(S6)}$ correspond to the Stellite 6 case, and $M_{s(S21)}$ and $A_{c(S21)}$ correspond to the Stellite 21 case), and (d) rail.

where every element mentioned in the equations represents the corresponding weight percentage.

For the powder 304L deposition steel, where $1.5 < Cr_{eq}/Ni_{eq} < 2.0$, the phase transformation process is proposed as follows:

$$L \text{ @ } T \geq 1500°C \rightarrow L + \delta \rightarrow L + \gamma + \delta \rightarrow \gamma + \delta \rightarrow \gamma \text{ @ } T{\sim}25°C \tag{11}$$

where L, δ, and γ are the liquid phase, the δ-ferrite phase, and the austenite phase, respectively. Fig. 4a shows a schematic depiction of the aforementioned phase transformation prediction. A combination of austenite and δ-ferrite is the main product of 304L solidification. The final volume fraction of δ-ferrite is correlated directly with the solidification rate. The lower the solidification rate, the longer time the δ→γ transformation takes, which subsequently leads to a lower volume fraction of δ-ferrite. The cooling rate of every deposition layer is related to the bed temperature, where the bed refers to the railhead and the formerly deposited layer for the first deposition layer and successive deposition layers, respectively. Considering the bed temperature, defined as parameter T, and the standards developed by ASTM A800 [12], the δ-ferrite volume fraction for 304L tool steel is expressed as:

$$f_\delta = \begin{cases} 1 - exp(6.65 \times 10^{-5} \times T - 0.1142), & T \leq 800 \\ 0, & T > 800 \end{cases} \tag{12}$$

where f_δ is the volume fraction of retained δ-ferrite after complete cooling to room temperature. Also, Fig. 4a shows that when the reheating exceeds 1000°C, the subsequent cooling to room temperature results in a pure austenite microstructure.

Fig. 4b shows a phase transformation diagram of 410L stainless martensite steel, which technically undergoes an γ→α→γ→L transformation during the first heating and a L→γ→γ+α+M transformation during the cooling that follows [13]. Therefore, as can be seen in Fig. 4b, the initial cooling process starts with a L→γ transition process, where, at the given range of cooling rates (0.5-100 °C/s), the diffusion of austenite essentially is restrained with the only exception being a minor γ→M transformation that starts at the $M_{s(410L)}$ temperature. Depending on the rate of cooling, $M_{s(410L)}$ may vary over a wide range of temperatures, i.e., 245 - 375°C [14]. Based on the findings of Lima et al. [14], $M_{s(410L)}$ has an inverse correlation with the cooling rate and its austenization temperature ($A_{c(410L)}$). In consonance with the dilatometry findings of Deev et al. [13], the $A_{c(410L)}$ is considered equal to 900°C in the ongoing calculations. Thus, for a constant $A_{c(410L)}$, the variation of $M_{s(410L)}$ as a function of cooling rate can be formulated as follows:

$$M_{s(410L)} = 375 - 0.56(CR) \tag{13}$$

where CR is the cooling rate (°C/s). The Koistinen and Marburger equation [15], which is applicable to an extensive selection of ferrous alloys, is used in the kinetic model in order to predict the volume fraction of the martensite being formed below $M_{s(410L)}$:

$$f_M = \begin{cases} 1 - f_{\gamma_1}, & T \geq M_{s(410L)} \\ 1 - f_{\gamma_1} \times \exp\left(-0.011\left(M_{s(410L)} - T\right)\right), & T < M_{s(410L)} \end{cases} \tag{14}$$

where f_M is the martensite volume fraction at temperature T, and $f_{\gamma 1}$ is the initial volume fraction of austenite. Fig. 4b shows that after the initial cooling of 410L and during the reheating process, the volume fractions of austenite and α-ferrite are increased and decreased linearly with the temperature, respectively, until the α-ferrite is completely transformed to austenite at $A_{c(410L)}$. Fig. 4b shows that if the subsequent cooling occurs before reaching $A_{c(410L)}$, there will be a partially or fully γ→M transformation, along with the formation of α-ferrite. The formulated volume fraction of the retained austenite for 410L steel is expressed and inserted into the model:

$$f_\gamma = f_{\gamma_1} \times exp\left(-\left(M_{s(410L)} - T\right)/91\right) \quad (15)$$

where f_γ is the retained austenite volume fraction at temperature T. Accordingly, the α-ferrite volume fraction is equal to:

$$f_\alpha = 1 - f_M - f_\gamma \quad (16).$$

However, if the cooling process starts after exceeding $A_{c(410L)}$, there would be only an γ→M transformation, and no formation of α-ferrite would occur.

The phase-transformation paradigm in Fig. 4c illustrates the misroctructural evolutions of Stellite 6. The Co-based Stellite 6 alloy generally consists of two allotropes, i.e., 1) a high-temperature γ allotrope that has a face-centered-cubic (fcc) crystal structure and is strongly stable up to the melting temperature of 1500°C and 2) a low-temperature allotrope, ε, with hexagonal-close-packed (hcp) crystallite, which gains stability at temperatures lower than 417°C [16]. Under various circumstances, these two allotropes can transform into each other. The γ→ε is referred to as the martensitic transformation. At the cooling step, it undergoes an γ→ε transition starting at $M_{s(S6)}$ = 390°C, as shown in Fig. 4c, during the first step of cooling. The martensite starts to develop linearly below $M_{s(S6)}$ until its volume fraction reaches f_ε at room temperature, i.e., 25°C. When the bed temperature, T, and the cooling rate, CR, are known, the equations developed by Yang et al. [16] can be used to calculate the volume fraction of the transformed martensite at each time step by solving the following equation for f_ε:

$$\frac{CR}{\vartheta . exp(-Q/RT)} = \left(\frac{1}{s_g^2 . a_{hcp}} + (10^{15.532-3.897.f_\varepsilon}). f_\varepsilon\right).(1 - f_\varepsilon) \quad (17)$$

where Q is the active energy required for nucleation, which, according to the results of Turrubiates-Estrada et al. [17], is 164 kJ/mol; R is the gas constant, i.e., 8.314 J/mol.K; s_g is the grain size of the matrix, i.e., 18.3 μm [16]; and a_{hcp} is the lattice constant of the hcp crystal structure, which is set equal to 4.113 Å [16]. During the reheating, the reverse transition of ε→γ occurs at $A_{c(S6)}$ = 417°C. Regarding the precipitated M_xC_y carbides, there is a linear relationship between the martensitic transformation and carbide precipitation. Hence, the kinetic calculations of the current model for Stellite 6 are set such that the momentary volume fraction of the precipitated carbides, f_c, at any given time is equal to:

$$f_c = 0.15(f_{\varepsilon-moment}) \quad (18)$$

where, according to Fig. 4c, during the reheating process, $f_{\varepsilon\text{-moment}}$ is equal to f_ε at temperatures below $A_{c(S6)}$, and then begins to decrease linearly from f_ε at $A_{c(S6)}$ = 417°C to 0 at T_{melt} = 1500°C. Fig. 4c shows that the retained volume fraction of each phase during the subsequent cooling after reheating is defined to remain exactly the same as the momentary volume fraction at the time step when reheating is finished and subsequent cooling begins.

The other Co-based deposition alloy is Stellite 21, which has the same phase-transformation protocol as that defined for Stellite 6 [18]. However, conforming to the calculations for the Co-Cr binary system [19], there is a slight shifting of the M_s and A_c temperatures for Stellite 21, compared to those for Stellite 6. Therefore, the phase-transformation paradigm presented in Fig. 4c for Stellite 6 is repeated almost identically for Stellite 21, with the only exception being that $M_{s(S21)}$ = 370°C and $A_{c(S21)}$ = 398°C. This will cause changes to the amounts that are calculated for $f_{\varepsilon\text{-moment}}$, and subsequently, f_c.

In accordance with the phase-transformation diagram shown for the rail material in Fig. 4d, for the upper regions of the railhead that are close to the deposition area and that heat up to 1500°C, the subsequent cooling process undergoes a full $\gamma \rightarrow \alpha$ transformation and revives the complete pearlite structure at room temperature [20]. In this way, the volume fraction of austenite, $f_{\gamma(R)}$, is designed to decrease linearly from 1 at T = 1500°C to 0 at T = 25°C, a slope that is shown as b/a in Fig. 4d. For the regions of the rail that are heated initially to temperatures lower than 1500°C, but higher than the rail's austenization temperature, i.e., $A_{c(R)}$ = 600°C, a partial $\gamma \rightarrow \alpha$ transition occurs, and a portion of the austenite remains in the microstructure after cooling to room temperature. In Fig. 4d, at any temperature between 600°C and 1500°C that the cooling starts, $f_{\gamma(R)}$ decreases linearly with the same slope as b/a until it intercepts the T = 25°C line, where the right side of the intercepted T = 25°C line gives the amount of $f_{\gamma(R)}$. For the regions that are quite far from the deposition area and heat up only to temperatures below 600°C, the subsequent cooling produces pure α-ferrite without any austenite. It is worth mentioning that the presence of cementite in the pearlitic rail steel was low enough to be neglected.

6.1.3. Mechanical calculation

The element network in mechanical calculation is identical to that used for thermal calculation. According to the developed model in [21], a feed-forward artificial neural network (ANN) model of the back-propagation learning algorithm for training set with mean square error criteria is engaged for modeling elastic-plastic constitutive material to predict residual strain and stress. This model represents a combined isotropic-kinematic model of the infinitesimal theory of plasticity that is extended to large ranges of strain at elevated temperatures. It technically consists of three input variables of ANN including strain, strain rate, and temperature. The output variable is flow stress with eight neurons in the intermediate layers. More details regarding this utilized model can be found in the comprehensive study by Gupta et al. [21]. Table 2 gives the temperature- and microstructure-dependent mechanical and thermal properties of the deposition and rail materials for different microstructural phases and different temperatures that are inserted into the FE model.

The same element-birth-and-kill technique with equivalent activation rate in thermal calculation is employed here. Activation of each element occurs when the element's temperature drops below T_{liq}, and the corresponding thermal field is applied on the element as the initial thermal load. The activated element then starts to cool down while residing some elastic and plastic strain. Nevertheless, even the deactivated elements are technically alive but with a degrading stiffness. The stiffness starts to recover once the element is activated. Boundary conditions are applied only as to restrain the solid body from any probable rigid body motion.

Table 2 Temperature/microstructure-dependent mechanical and thermal properties of the rail and deposition tool steels used in FE modeling of the LPD-rail-repair process.

Material		T (°C)	E (GPa)	ν	Yield Strength, Y_s (MPa)	α (10^{-5}/°C)	c_p (J/kg°C)	k (W/m°C)
Rail (880-grade steel) [20]	α	25	203	0.26	460	1.20	434	60.5
		600	110	0.33	308	1.40	638	41.6
		1000	-	-	156	-	-	-
		1500	-	-	66	-	-	-
	γ	25	-	-	511	-	-	-
		600	-	-	358	-	-	-
		1000	19	0.40	204	1.47	886	12.6
		1500	19	0.40	61	1.47	886	12.6
304L stainless steel [22]	δ	25	-	-	215	-	-	-
		600	134	0.34	144	1.73	745	18.9
		1000	19	0.41	90	1.82	984	15.5
		1500	19	0.41	31	1.82	971	13.2
	γ	25	200	0.29	276	1.73	510	15.5
		600	141	0.37	211	1.87	687	22.4
		1000	19	0.45	94	1.97	953	28.7
		1500	-	-	39	-	-	-
410L stainless steel [22,23]	M	25	172	0.21	275	1.01	420	56.5
		600	-	-	211	-	-	-
		1000	-	-	93	-	-	-
		1500	-	-	28	-	-	-
	γ	25	207	0.29	415	1.58	502	20.5
		600	152	0.35	279	1.62	668	24.2
		1000	20	0.45	174	1.66	863	26.6
		1500	20	0.45	70	1.66	863	26.6
	α	25	200	0.27	360	1.08	460	18.2
		600	129	0.30	252	1.11	619	14.4
		1000	-	-	140	-	-	-
		1500	-	-	49	-	-	-
Stellite 6 [23,24]	ε	25	210	0.26	483	0.73	400	13.1
		600	152	0.29	370	0.93	553	21.6
		1000	21	0.36	203	1.12	565	24.7
		1500	21	0.36	69	1.12	565	24.7
	γ	25	237	0.28	750	1.14	444	14.8
		600	172	0.32	504	1.45	615	24.3
		1000	24	0.39	255	1.65	628	27.8
		1500	24	0.39	82	1.65	628	27.8
M_xC_y (Carbides)		25	190	0.20	313	0.68	373	40.8
		600	137	0.22	218	0.87	517	57.1
		1000	19	0.27	124	1.05	527	61.7
		1500	19	0.27	60	1.05	527	61.7
Stellite 21 [18,25]	ε	25	217	0.26	565	0.70	384	11.4
		600	160	0.30	379	0.89	512	19.5
		1000	21	0.34	192	1.08	553	22.7
		1500	21	0.34	58	1.08	553	22.7
	γ	25	245	0.28	650	1.10	427	13.0
		600	181	0.32	422	1.36	569	22.2
		1000	24	0.40	195	1.52	615	25.8
		1500	24	0.40	66	1.54	615	25.8

M_xC_y (Carbides)	25	196	0.19	517	0.66	359	35.9
	600	145	0.21	310	0.82	478	50.3
	1000	19	0.25	176	0.91	517	54.3
	1500	19	0.25	56	0.92	517	54.3

6.2. FE model validation

The predicted temperature, microstructure, hardness, and residual stress distribution in the LPD-repaired light rail are presented based upon the coordinate system shown in Sec. 5.1.1, Fig. 1. The predicted numerical results are analyzed and also compared against the measured experimental data to validate the developed FE model.

6.2.1. Thermal field

Validation of thermal calculation is executed through comparing the measured and predicted dilution region size. Optical microscope (OM) macrographs from the etched sample are used for measuring the dilution depth at different regions. In numerical regard, the immediate depth of the ≥1500°C thermal contours at the end of the activation course of a single element gives the predicted depth of the melted substrate, i.e., dilution depth. The OM macrographs from different locations of the deposition materials are put against the captured thermal contour at the corresponding location for comparison purposes. Fig. 5 maps the regions where the dimensional correlation between the measured and predicted dilution depth is performed; close-up inspection of these areas is depicted in Fig. 6. Despite a slight dimensional deviation, a fairly great coherence is observable between the numerical and experimental results. The reason of the resulting minor mismatch may be attributed to a few effective parameters on dilution depth, e.g., specific energy, local iron contamination, and local powder concentration, that are not considered in the FE model. Nonetheless, since none of the dimensional deviations does not exceed 10%, the accuracy of the thermal model is reliably insured.

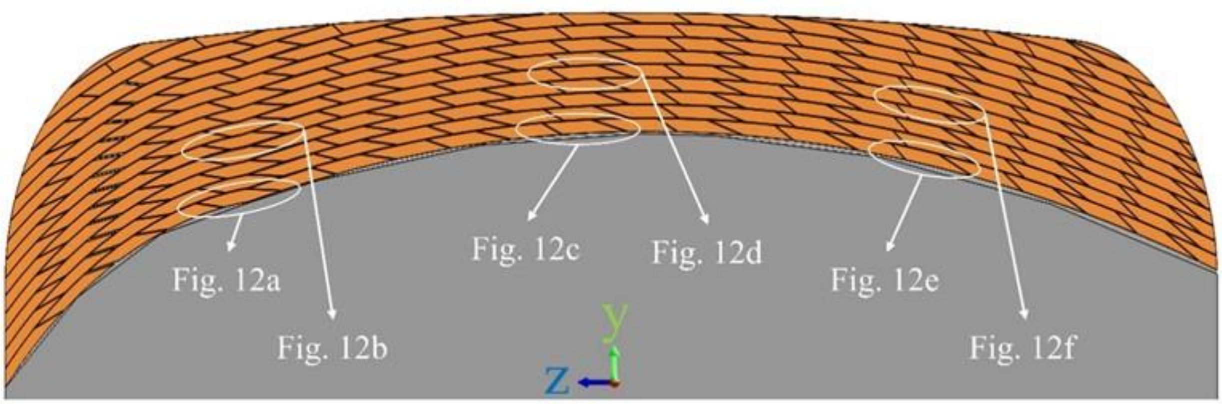

Fig. 6.5 General mapping of the areas where the dimensional comparison of the dilution depth between the predicted and measured results is performed. Referring to Sec. 5.1.1, Fig. 1, this figure shows the rail transversal cross section at x = 75 mm.

6.2.2. Hardness and microstructure distribution

Fig. 7 shows the measured hardness at different spots of the repaired rail. It is seen in the figure that the resulting hardness distribution offers that the repaired rail may be subdivided into three zones: (1) Deposition zone, where the upper layers are primarily consisted of untempered austenite and secondary δ-ferrite and lower layers contain primary δ-ferrite and tempered austenite due to the induced reheating cycles. (2) Heat-affected zone (HAZ) that encompasses the rail-deposition interface. Its deposition section contains austenite, δ-ferrite, and Cr-depleted δ-ferrite, and its rail section is majorly constructed of α-ferrite and austenite. And (3) rail zone that is made of austenite and α-ferrite.

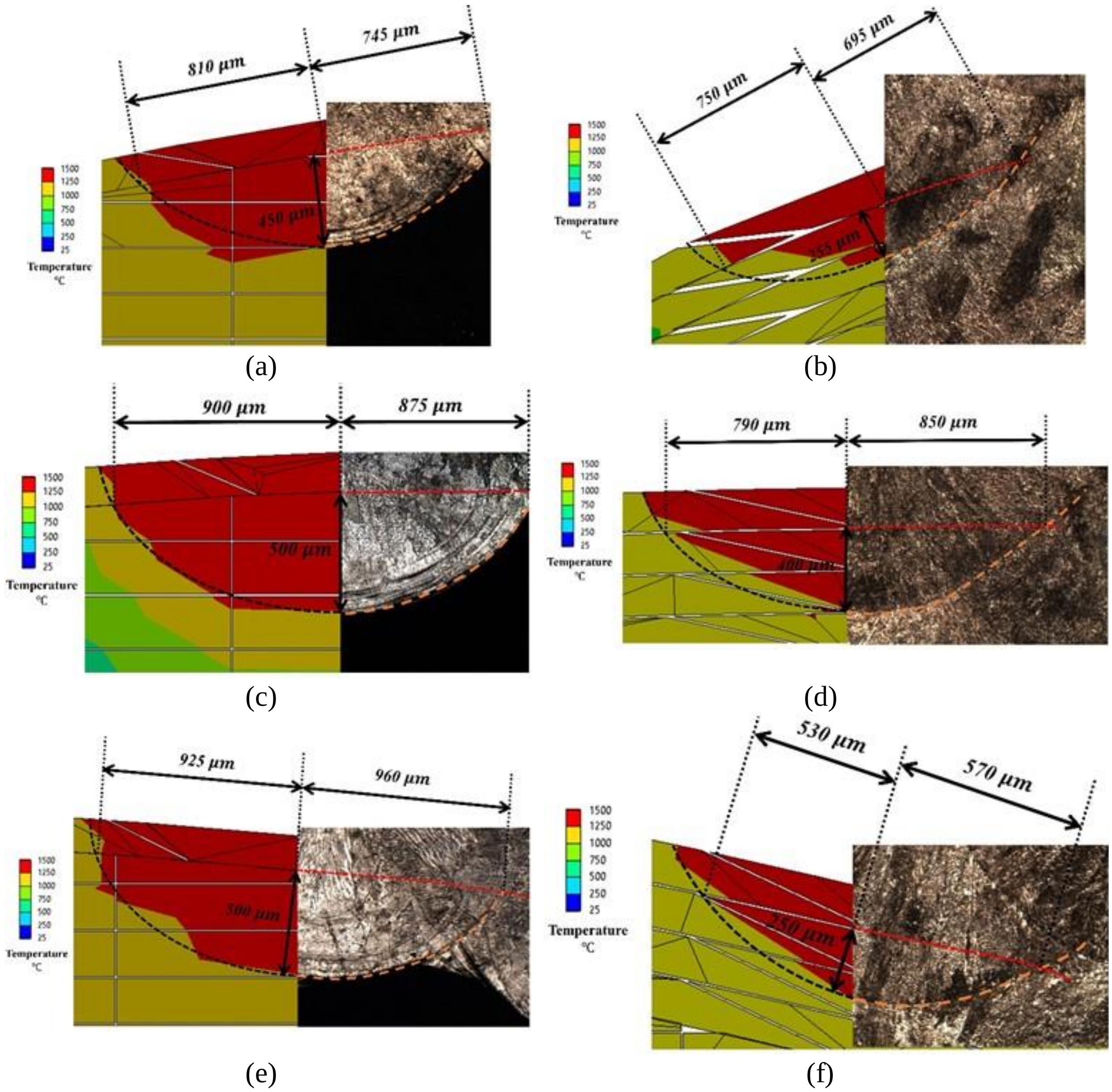

Fig. 6.6 Thermal contour distribution of the FE model versus the OM macrograph for dimensional comparison of dilution region between the numerical and experimental results at the (a) and (b) 5th, (c) and (d) 11th, and (e) and (f) 17th deposition row of the first and fifth deposition layers, respectively.

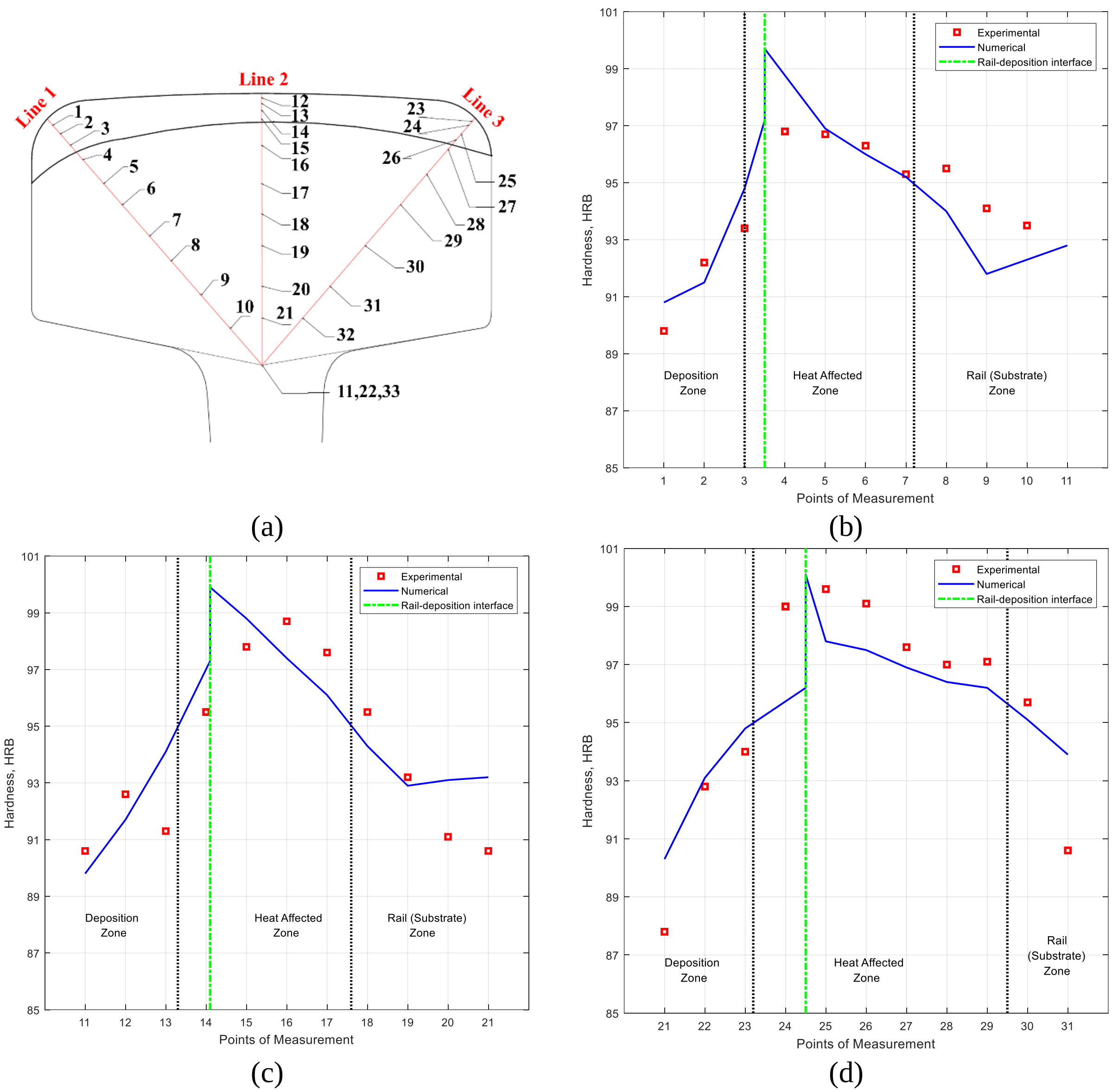

Fig. 6.7 Experimental vs. numerical hardness results; (a) schematic map of the points and lines on which the hardness is measured; (b) hardness distribution along line 1, (c) line 2, and (d) line 3.

The numerically calculated hardness values are put together with the experimental hardness results in Fig. 7. A stepped increase in numerical hardness values is discernible at the rail-deposition interface, of which the reason is attributed to different hardness expressions in those two zones in the FE model. The involved errors in both hardness measurement and calculation may be ascribed by the implicated errors in hardness test such as repeatability, correlation, and accuracy and also by the included approximations in the FE model. Anyhow, with 2.5% of maximum deviation, there is a quite well agreement between the measured and predicted hardness results.

The distribution of austenite volume fraction, f_δ, in the repaired rail is also calculated and put next to the predicted hardness distribution in Fig. 8. The presented results in this figure suggest an inverse correlation between hardness and austenite volume fraction.

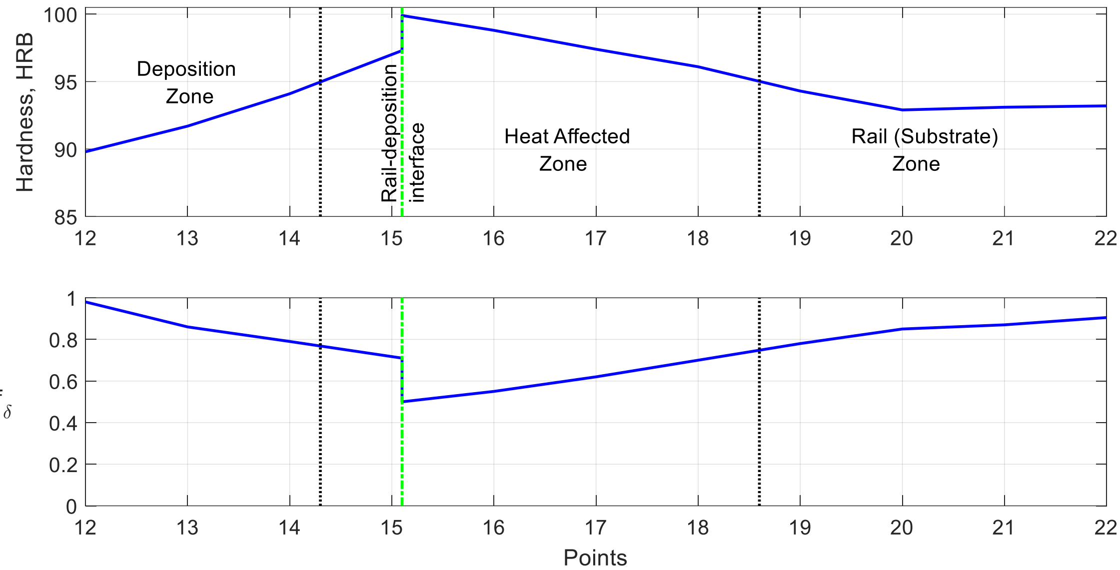

Fig. 6.8 Distribution of hardness and austenite volume fraction, f_{δ}, along line 2 (refer to Fig. 7a for configuration of line 2).

As it is evident in both Figs. 7 and 8, the hardest region locates inside the HAZ with an approximate value of 100 HRB near the rail-deposition interface. The top surface of the deposition zone, with the highest austenite concentration (Fig. 8b), has the lowest hardness (~90 HRB). The rail is not preheated in the current case study, and hence it acts as a huge heat extraction source during LPD. Therefore, fast cooling of the first deposition layer results in precipitation of δ-ferrite, which subsequently leads to high hardness amount for the initial deposition layer that is adjacent to rail-deposition interface. The bed temperature for subsequent deposition layers will be higher than that for the first layer, which brings a lower rate of cooling. Smoother cooling rate results in higher austenite volume fraction that causes lower hardness in the middle layers compared to the first layer. However, when a deposition layer is reheated by the upper deposition layers, δ-ferrite and Cr-depleted δ-ferrite are precipitated in the microstructure and intensify the hardness. Since the top layer does not undergo a reheating cycle, it experiences a complete austenite transformation and thus has the lowest hardness among all the deposition layers (Fig. 8).

The upper zone of the rail that falls into the HAZ is exposed to the laser beam and heats up to elevated temperatures near 1500°C. This area is then gradually cooled down to room temperature and almost completely transfers back to α-ferrite. Nevertheless, because the lower zone of the rail does not heat as high as the upper zone, a fraction of the microstructure remains austenite after complete cooling to 25°C. This fact describes the higher austenite and lower hardness in the lower zone of the rail rather than its upper region inside HAZ. Comparing this set of analysis on the microstructure distribution against those experimental findings presented in Sec. 3.1.2. shows a great agreement between the model predictions and real measurements.

6.2.3. Residual stress distribution

The longitudinal stress, σ_l, along x direction and transversal stress, σ_t, along z direction are the major driving forces to cause crack propagation along the corresponding directions (refer to Sec. 5.1.1, Fig. 1 for configuration of the reference coordination). Also, the normal stress, σ_n, along y direction is the leading motivation of delamination. Fig. 9 gives the derived numerical and experimental distribution of σ_l, σ_t, and σ_n along x, z, and y directions, respectively.

The experimental measurement of the residual stresses was presented in Sec. 5.1.1 and the resulting values were given in Sec. 5.1.1, Table 1. All of those measured values in Sec. 5.1.1, Table 1 are depicted as the red square-shaped dots in Fig. 9.

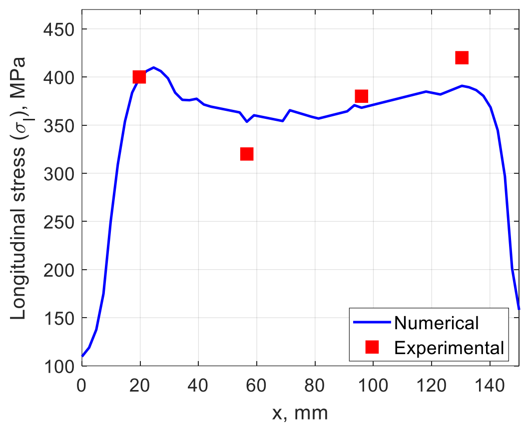

(a)

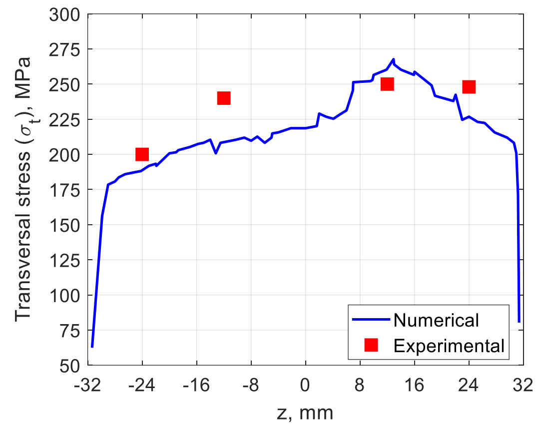

(b)

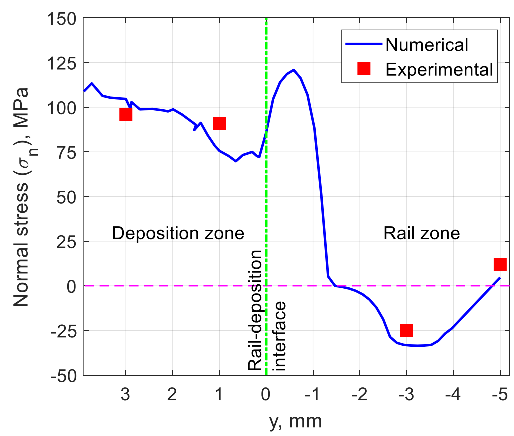

(c)

Fig. 6.9 Experimental vs. numerical residual stress distribution; (a) longitudinal stress, σ_l, along x direction at (y, z) = (0, 0), (b) transversal stress, σ_t, along z direction at rail-deposition interface for x = 0, and (c) normal stress, σ_n, along y direction at (x, z) = (0, 0). Refer to Sec. 5.1.1, Fig. 1 for configuration of the reference coordination system.

Now, speaking of the numerical values, it is evident in Fig. 9a and b that σ_l and σ_t remain all tensile due to the applied tensile stress from rail to the deposition materials at the interface. Both of the σ_l and σ_t go through a sharp ascend/drop at the two ends of their calculation interval and achieve their maximum value at the middle of the interval. The σ_l local peak values at x = 25 and 130 mm are equal to 410 and 390 MPa, respectively, and the single peak value of σ_t at z = 13 mm is 270 MPa. It is also observable that the numerical σ_l and σ_t graphs have an oscillating form rather than a smooth form. The reason of the presence of such oscillations is that the residual stress due to the deposition of every row is partially relieved once the adjacent row is deposited. According to Fig. 9a and b, there are more oscillations happening for σ_t rather than that for σ_l, of which the reason is that the deposition elements are not overlapped along the x direction, but there is a 50% overlap between the deposition rows along the z direction. More overlap leads to more stress relief and consequently more of those oscillations.

Regarding the numerically predicted distribution of σ_n in Fig. 9c, it remains tensile in the entire deposition zone ($0 \le y \le 4$ mm). In the rail zone (-5 mm $\le y \le 0$), it achieves a maximum 120 MPa near rail-deposition zone at y = −0.5 mm. It then sharply decays and alters to compressive and experiences a maximum compressive of 33 MPa at y = −3.2 mm and finally becomes neutral at around y = −5 mm. The reason that σ_n remains tensile to a specific depth of the rail zone is attributed to the dilution region that keeps the residual stress tensile down to the heat penetration depth of the substrate. The determinant factor that contributes to delamination is the gradient of σ_n at the rail-deposition interface. In the deposition zone, σ_n has an oscillating behavior which is due to the stress relief that happens during adding the upper layers upon the lower layers. As Fig. 9c depicts, the upper region of the deposition zone ($2 \le y \le 4$ mm) has higher σ_n values than the lower region ($0 \le y < 2$mm), because the upper layers are not reheated and consequently stress-relieved, as frequently as the lower layers do.

It can be deduced visually from Fig. 9 that the experimental results are comparable fairly well with the calculated data. The derived values show that the maximum difference between the measured and predicted stresses is as low as 10%. Both the experimental measurements and numerical calculations can be responsible for the errors. Increasing the number of counts in XRD analysis, eliminating the allocated approximations in choosing elastic constants, and refining the elements of the FE model can lead to a more accurate model and lower errors. The current FE model is viewed sufficient since the present errors are low enough to be neglected. Refining the FE model would considerably increase the calculation time. Hence, the present model for the ongoing aim is precise enough to provide reliable data for further parametric studies concerning the residual thermal stress during the LPD rail repair process.

In Chapter 7, the validated FE model is utilized to find the optimum LPD procedure in the matter of the deposition material and the preheating temperature to lead to the lowest residual stress in the LPD-repaired light rail.

References for Chapter 6

[1] G.E. Totten, M.A.H. Howes, T. Inoue, Handbook of residual stress and deformation of steel, ASM International (2002) ISBN: 978-0-87170-729-1.

[2] I. Tabernero, A. Lamikiz, S. Martínez, E. Ukar, L.N. López de Lacalle, Modelling of energy attenuation due to powder flow-laser beam interaction during laser cladding process, J. Mater. Process. Technol. 212(2) (2012) 516–522. https://doi.org/10.1016/J.JMATPROTEC.2011.10.019.

[3] C. Liu, J. Lin, Thermal processes of a powder particle in coaxial laser cladding, Opt. Laser Technol. 35(2) (2003) 81–86. https://doi.org/10.1016/S0030-3992(02)00145-7.

[4] J. Lin, Concentration mode of the powder stream in coaxial laser cladding, Opt. Laser Technol. 31(3) (1999) 251–257. https://doi.org/10.1016/S0030-3992(99)00049-3.

[5] J.M. Jouvard, D.F. Grevey, F. Lemoine, A.B. Vannes, Continuous wave Nd:YAG laser cladding modeling: a physical study of track creation during low power processing, J. Laser Appl. 9(1) (1997) 43–50. https://doi.org/10.2351/1.4745444.

[6] Y. Chew, J.H.L. Pang, G. Bi, B. Song, Thermo-mechanical model for simulating laser cladding induced residual stresses with single and multiple clad beads, J. Mater. Process. Technol. 224 (2015) 89–101. https://doi.org/10.1016/J.JMATPROTEC.2015.04.031.

[7] A. Frenk, M. Vandyoussefi, J.D. Wagnière, W. Kurz, A. Zryd, Analysis of the laser-cladding process for stellite on steel, Metall. Mater. Trans. B 28(3) (1997) 501–508. https://doi.org/10.1007/s11663-997-0117-0.

[8] Y. Zhu, Y. Yang, X. Mu, W.J. Wang, Z. Yao, H. Yang, Study on wear and rcf performance of repaired damage railway wheels: assessing laser cladding to repair local defects on wheels, Wear 430–431 (2019) 126–136. https://doi.org/10.1016/j.wear.2019.04.028.

[9] T. Roy, R. Abrahams, A. Paradowska, Q. Lai, P. Mutton, M. Soodi, P. Fasihi, W. Yan, Evaluation of the mechanical properties of laser cladded hypereutectoid steel rails, Wear 432–433 (2019) 202930. https://doi.org/10.1016/j.wear.2019.202930.

[10] Maintenance for railway engineering, American Railway Engineering and Maintenance-of-way Association (AREMA) Vol. 1: Track, Director of Administration (2014) ISSN: 1543-2254

[11] K. Rajasekhar, C.S. Harendranath, R. Raman, S.D. Kulkarni, Microstructural evolution during solidification of austenitic stainless steel weld metals: a color metallographic and electron microprobe analysis study, Mater. Charact. 38(2) (1997) 53–65. https://doi.org/10.1016/S1044-5803(97)80024-1.

[12] ASTM A800/A800M-01, Standard practice for steel casting, austenitic alloy, estimating ferrite content thereof, ASTM International, West Conshohocken, Pennsylvania (2001). https://doi.org/10.1520/A0800_A0800M-01.

[13] A. Deev, P. Kuznetsov, A. Zhukov, V. Bobyr, The structure and properties of the samples produced by selective laser melting of 410L steel-based metal powder, Phys. Procedia 89 (2017) 31-38. https://doi.org/10.1016/j.phpro.2017.08.013.

[14] M.S.F. Lima, A.M.E. Santo, Phase transformations in an AISI 410S stainless steel observed in directional and laser-induced cooling regimes, Mater. Res. 15(1) (2012) 32-40. https://doi.org/10.1590/S1516-14392012005000003.

[15] D.P. Koistinen, R.E. Marburger, A general equation prescribing the extent of the austenite-martensite transformation in pure iron-carbon alloys and plain carbon steels, Acta Metall. 7(1) (1959) 59-60. https://doi.org/10.1016/0001-6160(59)90170-1.

[16] D. Yang, C. Hua, S. Qu, J. Xu, J. Chen, C. Yu, H. Lu, Isothermal transformation of γ-Co to

ε-Co in Stellite 6 coatings, Metall. Mater. Trans. A 50 (2019) 1153–1161. https://doi.org/10.1007/s11661-018-5057-6.
[17] R. Turrubiates-Estrada, A. Salinas-Rodriguez, H.F. Lopez, FCC to HCP transformation kinetics in a Co–27Cr–5Mo–0.23C alloy, J. Mater. Sci. 46 (2011) 254–262. https://doi.org/10.1007/s10853-010-4969-3.
[18] K.P. Sołek, Ł. Rogal, P. Kapranos, Evolution of globular microstructure and rheological properties of Stellite™ 21 alloy after heating to semisolid state, J. Mater. Eng. Perform. 26 (2017) 115–123. https://doi.org/10.1007/s11665-016-2421-9.
[19] C. Allibert, C. Bernard, N. Valignat, M. Dombre, Co-Cr binary system: experimental re-determination of the phase diagram and comparison with the diagram calculated from the thermodynamic data, J. Less Common Met. 59(2) (1978) 211-228. https://doi.org/10.1016/0022-5088(78)90131-5.
[20] U.P. Singh, B. Roy, S. Jha, S.K. Bhattacharyya, Microstructure and mechanical properties of as rolled high strength bainitic rail steels, Mater. Sci. Technol. 17(1) (2001) 33–38. https://doi.org/10.1179/026708301101509098.
[21] A.K. Gupta, H.N. Krishnamurthy, Y. Singh, K.M. Prasad, S.K. Singh, Development of constitutive models for dynamic strain aging regime in austenitic stainless steel 304. Mater. Des. 45 (2013) 616–627. https://doi.org/10.1016/J.MATDES.2012.09.041.
[22] ASM Handbook, Properties and selection: irons, steels, and high-performance alloys, in: Elevated-temperature properties of stainless steels, ASM International 1 (1990) 930-949. https://doi.org/10.31399/asm.hb.v01.a0001048.
[23] T. Han, C.H. Kuo, N. Sridharan, L.M. Headings, S.S. Babu, M.J. Dapino, Effect of preheat temperature and post-process treatment on the microstructure and mechanical properties of stainless steel 410 made via ultrasonic additive manufacturing, Mater. Sci. Eng. A 769 (2020) 138457. https://doi.org/10.1016/j.msea.2019.138457.
[24] N. Hutasoit, W. Yan, R. Cottam, M. Brandt, A. Blicblau, Evaluation of microstructure and mechanical properties at the interface region of laser-clad Stellite 6 on steel using nanoindentation, Metallogr. Microstruct. Anal. 2 (2013) 328–336. https://doi.org/10.1007/s13632-013-0093-5.
[25] F.J. Clauss, J.W. Weeton, Relation of microstructure to high-temperature properties of a wrought cobalt-base alloy Stellite 21, AMS (1953) 5385. https://digital.library.unt.edu/ark:/67531/metadc56992/.

7. Chapter 7 STUDY ON THE EFFECT OF PREHEATING AND DEPOSITION MATERIALS ON THE RESIDUAL STRESSES IN THE REPAIRED RAIL USING THE VERIFIED FE MODEL

7.1. Effect of preheating and deposition alloy

After the development and verification of the finite element (FE) model in Chapter 6 based on the no-preheating case and 304L stainless steel as the deposition material, further potential deposition alloys, i.e., 410L stainless steel, Stellite 6, and Stellite 21, are tried for LPD-repairing the light rail only through the numerical study. In this way, chemical compositions of other studied deposition alloys are also brought in Table 1. Model development and numerical study of further potential deposition materials for LPD-repairing of heavy rails is currently under investigation.

Table 3 Chemical composition of the utilized LPD steel powders (wt.%).

Material	Co	Fe	C	Cr	Mn	Mo	Si	Ni	P	S	W
304L	-	Bal.	0.03	19.0	2.00	-	1.00	10.5	0.045	0.03	-
410L	-	Bal.	0.01	13.5	0.50	0.01	0.47	0.08	0.02	0.03	-
Stellite 6	Bal.	0.10	1.2	30.5	0.02	0.01	1.55	0.70	0.03	0.01	5.00
Stellite 21	Bal.	0.15	0.23	27.0	0.60	5.00	0.85	2.10	0.01	0.01	0.05

Based on the represented study plan in Table 2, the results are presented in four separate cases, i.e., Cases I, II, III, and IV, which explore 304L, 410L, Stellite 6, and Stellite 21 deposition tool steels, respectively. For each case, the residual stress distribution is given for five different rail-preheating cases, i.e., T_i = 25°C, 400°C, 600°C, 800°C, and 900°C.

Table 4 An overview of the employed study plan to investigate the residual stress out of the FE model results

Case no.	Deposition tool steel	Calculated residual stress*	Preheating Temperature, T_i (°C)				
Case I	304L stainless steel	σ_l along x	25	400	600	800	900
		σ_t along z	25	400	600	800	900
		σ_n along y	25	400	600	800	900
Case II	410L stainless steel	σ_l along x	25	400	600	800	900
		σ_t along z	25	400	600	800	900
		σ_n along y	25	400	600	800	900
Case III	Stellite 6	σ_l along x	25	400	600	800	900
		σ_t along z	25	400	600	800	900
		σ_n along y	25	400	600	800	900
Case IV	Stellite 21	σ_l along x	25	400	600	800	900
		σ_t along z	25	400	600	800	900
		σ_n along y	25	400	600	800	900

* The parameters σ_l, σ_t, and σ_n refer to the longitudinal, transversal, and normal stress, respectively. The coordination system along which the residual stresses are measured, are shown in Sec. 5.1.1, Fig. 1.

7.1.1. Case I

The residual stress distribution in the 304L repaired rail is given in Fig. 1. Because the 304L had higher value of thermal expansion coefficient than the rail (Sec. 6.1.3, Table 2), it tended to shrink faster than the rail. Consequently, the rail, as the stronger material, tries to harness the shrinkage of the deposition material by applying a tensile stress. Therefore, the σ_l and σ_t components remain tensile all over their measuring paths at the rail-deposition interface (Figs. 1a and b). For T_i = 25°C, both σ_l and σ_t experience a sharp increase/decrease towards both ends of their paths. σ_l undergoes two local maximums of 410 and 390 MPa at x = 24.6 and 130.4 mm, respectively, while σ_t encounters one peak of 268 MPa at z = 12.92mm. An inspection of the effect of preheating suggests that increasing the preheating temperature from 25°C to 900°C generally contributes to a changeover from the sharp stress distribution to a more uniform distribution. The deviation between the minimum and maximum values of σ_t (Fig. 1b) is decreased significantly by preheating, i.e., from 77% for T_i = 25°C to 46% for T_i = 900°C, which leads to a quite uniform stress distribution for the latter case. Regarding σ_l (Fig. 1a), by every increase in T_i, the two local maximum values shift towards the middle of the measuring path until they merge for T_i = 900°C case, where only one blunt local maximum occurs at x = 83.64 mm. On average, each step of increasing T_i results in about 25% reductions in both σ_l and σ_t. This notable reduction emerges from two objectivities, i.e., 1) the higher bed temperature leads to lower thermal gradients and 2) the temperature-dependent yield strength is decreased dramatically at high temperatures (Sec. 6.1.3, Table 2).

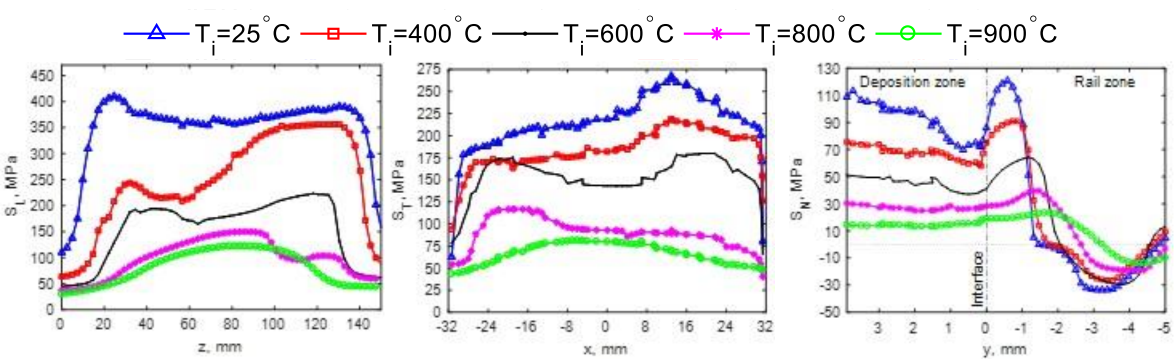

(a) (b) (c)

Fig. 7.1 (a) Longitudinal, (b) transversal, and (c) normal residual stress distributions for 304L repaired rail (Case I) along paths along x, z, and y directions, respectively. (Refer to Sec. 5.1.1, Fig. 1 for configuration of the coordinate system.)

Another important observation in the σ_l and σ_t distribution graphs is the presence of numerous local oscillations in every graph, especially for cases with lower values of T_i. These oscillations are ascribed to the fact that, due to the deposition of each clad, the induced residual stress is relieved partially when the adjacent clad is deposited. Considering the preheating trends in Figs. 1a and 1b, it is evident that the oscillations have eased off, and they gradually disappear as T_i is increased. When the substrate is preheated and the first layer is deposited on a bed with higher temperature, there would be lower thermal gradients at the time of the deposition of a new high-temperature adjacent clad; therefore, no notable relief in the stress would be visible in the stress distribution graphs. Moreover, it is discernible that the σ_t distribution, shown in Fig. 1b, contains more of these local oscillations compared to those for the σ_l distribution in Fig. 1a for the same T_i value. This is because there is no overlap between two consecutive clads in the longitudinal direction, but there is a 50% of adjacent clad overlap in the transverse direction, which intensifies the stress-relief effect in the transverse direction, and, consequently, shows more severe stress oscillations.

The σ_n distribution in Fig. 1c remains tensile over all of the deposition zone until it reaches a maximum near, but slightly underneath, the rail-deposition interface. Then, it goes through a sharp decay and switches to compressive stress. The compressive stress area also experiences a maximum in the rail zone, and, ultimately, becomes neutral as it approaches about 5 mm beneath the rail-deposition interface. In the σ_n distribution along *y*, Fig. 1c, the region between the maximum-tensile and maximum-compressive points is defined as the heat affected zone (HAZ). The high gradient of σ_n at the rail-deposition interface is the predominant contributor to the separation of the deposition part from the rail. The other visible fact in Fig. 1c is that, for T_i = 25°C, σ_n increases gradually from the rail-deposition interface upwards to the free surface on the top, i.e., at y = 3.9 mm. This behavior is attributed to two factors, i.e., 1) the upper deposition layers are subjected to faster cooling and shrinkage rates because they do not get reheated as frequently as the lower layers do and 2) the cooling-reheating cycles that the lower layers experience when the upper layers are being deposited, cause partial relief of the stress; this does not occur for the upper layers.

According to the graphs presented in Fig. 1c, the following major observations can be made concerning the effects of preheating: 1) increasing T_i shifts the tensile and compressive peaks deeper downwards to the rail zone, meaning that a higher preheating temperature deepens the HAZ; 2) the increment of preheating temperature squeezes the σ_n distribution curves to a smoother distribution, leading to a dramatic decrease in the HAZ stress gradient between maximum tensile and maximum compressive; 3) it mitigates the σ_n gradient at the rail-deposition interface, which will considerably decrease the chance of delamination; 4) the σ_n distribution in the deposition area (y > 0) becomes more uniform as the T_i increases; the deviation between the maximum and minimum stress in the deposition zone tends toward zero, and the stress fluctuations between two consecutive layers gradually fade away. The amount of heat that can be extracted from the deposited layers through the bulk substrate decreases as the preheating temperature increases. Thus, for T_i = 25°C, each deposited layer cools down enough to reside some reasonable stress, part of which will be released when the next layer is deposited. Increasing T_i helps to keep the bed temperature uniform and at a fairly high level throughout the entire deposition process. Subsequently, at the end of the deposition process, the deposition part is allowed to cool as a whole, integral component, concluding with a uniform stress distribution without any internal fluctuations between the layers.

7.1.2. Case II

Fig. 2 shows the residual stress distribution in the 410L repaired rail. For this case, for the same reason described for Case I, both σ_l and σ_t remain tensile all over their measuring paths, respectively (Figs. 2a and b). The distribution pattern of σ_l and σ_t generally are similar to that for Case I. Even so, the overall values of σ_l and σ_t for the T_i = 25°C condition for Case II (Figs. 2a and b) have been increased by about 45% and 40%, respectively, compared to the values for Case I (Figs. 1a and b); this is attributed to the higher average yield strength of 410L than that of 304L (Sec. 6.1.3, Table 2). Regarding the preheating cases, the σ_l values in Case II compared to Case I for T_i = 400°C, 600°C, 800°C, and 900°C are higher by around 31%, 27%, 21%, and 14%, respectively. In addition, the σ_t values in Case II are higher by 39%, 24%, 22%, and 21% for T_i = 400°C, 600°C, 800°C, and 900°C, respectively, than those in Case I. It is concluded that the overall difference of σ_l and σ_t between Cases I and II decreases as the T_i increases. This means that preheating at higher temperatures can, to some extent, diminish the dominance of the effects of the deposition material's properties on the resulting residual stresses. Also, it is perceptible in Sec. 6.1.3., Table 2 that the values of the thermal/mechanical properties of different materials become closer at elevated temperatures.

The normal stress distribution of 410L repaired rail along the y direction is illustrated in Fig. 2c. The general σ_n distribution follows the same motifs, similar to Case I, all along y direction, except for the deposition area. Moving from the rail-deposition interface (y = 0) upwards to the surface of the repaired rail (y = 3.9 mm), σ_n had an ascending trend for Case I (Fig. 1c), while it had a downward slope for Case II (Fig. 2c). According to Sec. 6.1.3., Table 2, the average values of specific heat, c_p, and thermal expansion coefficient, α, for 410L deposition steel are 22% and 25% lower than for 304L, respectively. Thus, although the top layers are less exposed to reheating cycles than the lower layers, they do not cool down and shrink as fast as 304L, and hence, they reside less normal stress. Also, a lower α coefficient causes lower thermal expansion and shrinkage, and, consequently, a lower deformation constraint exists along the depth direction, y, which ends up with a lower σ_n for the upper layers with the free surface on the top.

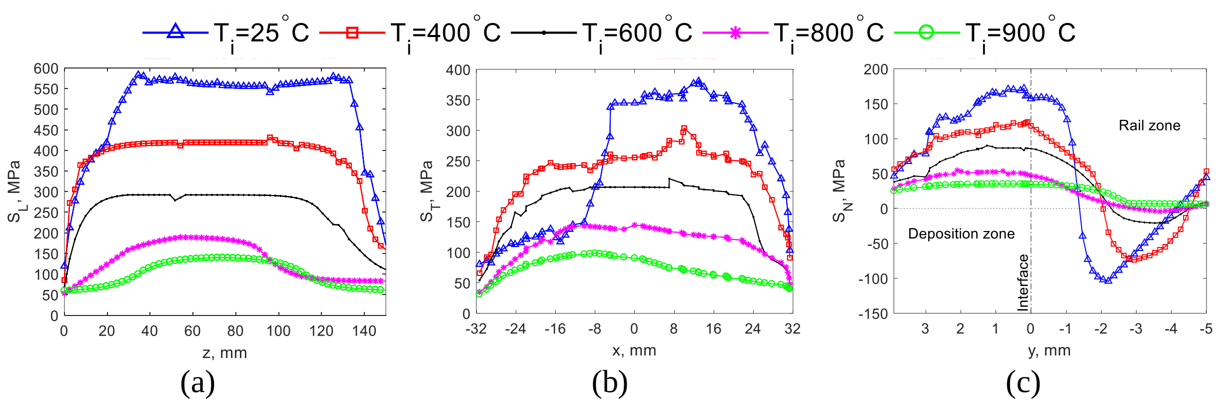

Fig. 7.2 (a) Longitudinal, (b) transversal, and (c) normal residual stress distributions for 410L repaired rail (Case II) along x, z, and y directions, respectively. (Refer to Sec. 5.1.1, Fig. 1 for configuration of the coordinate system.)

Concerning the values, the overall σ_n values in Case II for T_i = 25°C, 400°C, 600°C, 800°C, and 900°C preheating conditions are increased by approximately 51%, 42%, 40%, 38%, and 36%, respectively, compared to the amounts for Case I (Figs. 1c and 2c). Again, this confirms the idea of the attenuation of material properties' effects on residual thermal stress at high temperatures.

7.1.3. Case III

The residual stress distribution in the Stellite 6 repaired rail is presented in Fig. 3. Based on the information in Sec. 6.1.3, Table 2, Stellite 6 has a higher strength, but a lower thermal expansion coefficient, than the rail, 304L, and 410L. Thus, during the cooling procedure, the rail starts to shrink faster than Stellite 6, and, therefore, Stellite 6, as the stronger material, would apply a tensile stress at the rail-deposition interface in order to seize against the rail's shrinkage. This fact supports the reason for the thoroughly tensile distribution of σ_l and σ_t all along their measuring paths in Figs. 3a and b, respectively. Referring to Fig. 3a, σ_l goes through sharp gradients at both ends and remains almost uniform in the middle for all of the preheating cases, except that the sharpness of those gradients at the two ends decreases as T_i increases; the same description can be given to the σ_t distribution in Fig. 3b. The average σ_l amounts for Case III are increased by 63%, 61%, 58%, 49%, and 45% for T_i = 25°C, 400°C, 600°C, 800°C, and 900°C, respectively, against those for Case II, and the σ_t values are increased by 58%, 51%, 51%, 48%, and 45%, respectively. Hence, the overall residual stresses increase more steeply from Case II to Case III, rather than those from Case I to Case II, of which the dominant reason is due to the deposition materials' deviation in strength for different cases; although 410L (Case II) is moderately stronger than 304L (Case I), Stellite 6 (Case III) is much stronger than 410L (Sec. 6.1.3, Table 2).

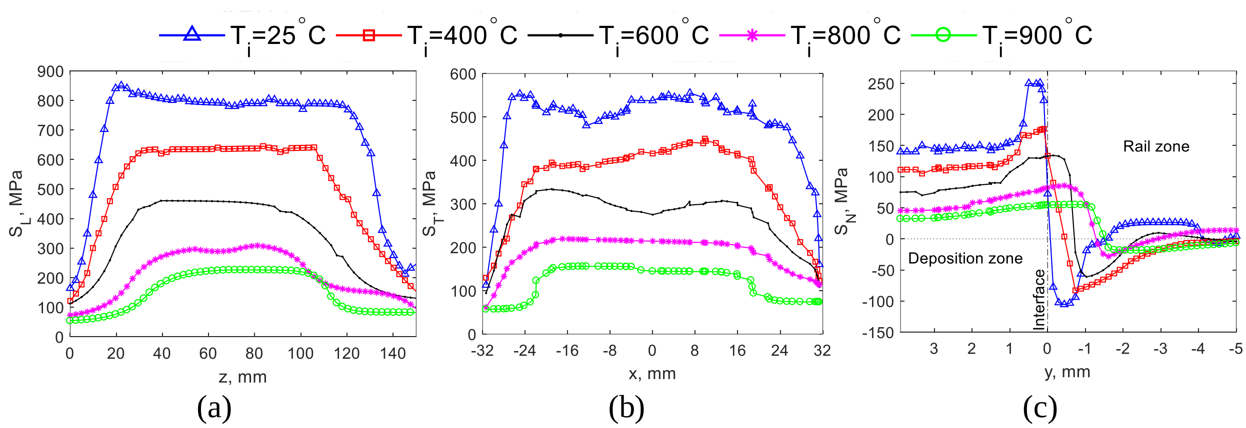

Fig. 7.3 (a) Longitudinal, (b) transversal, and (c) normal stress distributions for Stellite 6 repaired rail (Case III) along x, z, and y directions, respectively. (Refer to Sec. 5.1.1, Fig. 1 for configuration of the coordinate system.)

The σ_n diagram of the Stellite 6 repaired rail in Fig. 3c shows a quite uniform distribution in the deposition area for all T_i values. This consistency is due to the adequately low thermal expansion coefficient of Stellite 6, which minimizes thermal expansion and shrinkage during the deposition process, thereby minimizing the interlayer normal stresses. The lower specific heat is another effective parameter that causes all of the layers to cool down slowly enough not to cause any considerable increase in the stress on the upper layers. Sec. 6.1.3, Table 2 shows that the average thermal expansion coefficient of Stellite 6 is reduced by 12% and 33% compared to those for 410L and 304L, respectively, and the specific heat of Stellite 6 is, on average, lower than that for 410L and 304L by 13% and 29%, respectively. For T_i = 25°C, despite the desirable σ_n distribution in the deposition area, an increase in σ_n occurs near the rail-deposition interface at y = 0.20 mm, where the maximum tensile stress of 263 MPa is reached. Afterwards, σ_n experiences a sudden and significantly sharp diversion from tensile to compressive mode, until reaches the maximum compressive stress of -143.7 MPa in the rail zone at y = -0.44 mm. This extremely sharp σ_n gradient, which exists at the rail-deposition interface, would tremendously increase the risk of separating the deposition layer.

Based on the σ_n results in Fig. 3c, the advantageous effects of preheating are: 1) it essentially decreases the maximum tensile value, with a roughly 30% reduction by each increase in T_i; 2) the location of the maximum tensile stress is shifted gradually downwards to the rail zone, until it reaches y = -0.74 mm for T_i = 900°C; the HAZ also broadens along with this shifting, a phenomenon that eliminates any threat of failure in the deposition layers due to the high tensile amounts of σ_n; 3) the σ_n gradient at the rail-deposition interface is decreased substantially by raising T_i, thereby effectively decreasing the risk of delamination.

7.1.4. Case IV

The graphs in Fig. 4 illustrate the residual stress distribution in Stellite 21 repaired rail. A general comparison between the diagrams of Figs. 3 and 4 provides clear evidence that the distribution patterns of σ_l, σ_t, and σ_n between Cases III and IV are fairly similar. Moreover, the average σ_l, σ_t, and σ_n values of Case IV are 7%, 5%, and 4% higher than those for Case III. There are two justifications for such a close stress distribution: 1) it was described in Sec. 6.1.2 about how the microstructures of these two Co-based alloys are similar, which subsequently makes their defined kinetic models, and the corresponding developed equations, reasonably alike and 2) according to the data given in Sec. 6.1.3, Table 2, the predominant factors that affect the residual thermal stress, i.e., yield strength, Y_s, thermal expansion coefficient, α, and specific heat, c_p, of Stellite 21 are, on average, 4% higher, 6% lower, and 4% lower than those for Stellite 6, respectively. However, even though the Stellite 21 material properties deviate insignificantly from those of Stellite 6, the higher value of Y_s and the lower values of α and c_p still give the Stellite 21 repaired rail a higher, but smoother, stress distribution, although it does so to a limited extent.

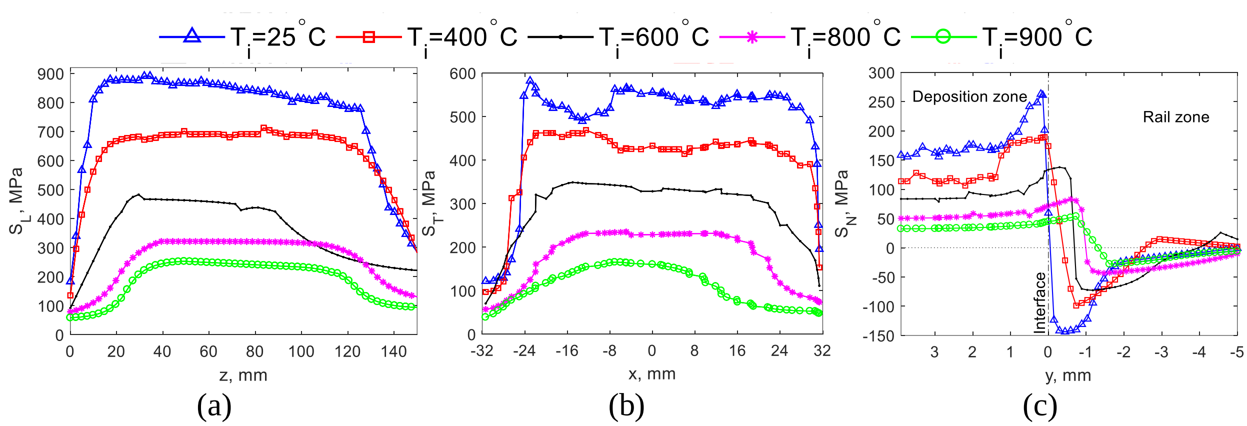

Fig. 7.4 (a) Longitudinal, (b) transversal, and (c) normal stress distributions for Stellite 21 repaired rail (Case IV) along x, z, and y directions, respectively. (Refer to Sec. 5.1.1, Fig. 1 for configuration of the coordinate system.)

7.2. Optimum preheating temperature and deposition alloy

All four studied cases in Sec. 7.1 for LPD-repair of light rail confirmed the positive effect of preheating on reducing and smoothing residual thermal stresses. Even so, on one hand, the experimental study of Fang et al. [1] showed that preheating to temperatures beyond 600°C would be either impractical or unjustifiably expensive, and on the other hand, Roy et al. [2] determined that preheating to temperatures below 400°C is insufficient to achieve the desired properties. Thus, preheating to 600°C would be the most optimum and realistic preheating approach. Therefore, hereafter, the residual stress results of the studied cases will be compared only based on the preheating condition of T_i = 600°C.

Fig. 5 shows the residual stress distributions for different deposition materials at T_i = 600°C. A close look at Sec. 6.1.3, Table 2 shows that the deposition materials in order of their yield strength, from the strongest to the weakest, are Stellite 21, Stellite 6, 410L, and 304L. As was discussed in Sec. 6.1.2, Stellite 6 and Stellite 21 have quite similar strengths. Therefore, Fig. 5 shows that Stellite alloys carry sensibly higher residual stresses than the stainless steels. Although Stellite 6 carries higher residual stresses at some local intervals of the measuring paths, the Stellite 21 generally contains the highest residual thermal stress in all three directions.

However, the magnitude of the residual stress is not the only decisive factor to determine the repaired rail's susceptibility to cracking and delaminating; the yield strength of the deposition alloy at room temperature is a second factor, and it is as critical as the first factor. Thus, to analyze the risk of the crack propagation and the layer separation for different cases with different deposition alloys, a new parameter, referred to as "normalized residual stress", is defined as the ratio of the residual stress to the room-temperature yield strength of the corresponding deposition material [3-5].

Fig. 6 gives the normalized residual stress distribution for different deposition alloys at T_i = 600°C. Fig. 6a shows that Stellite 21 and 304L generally carry lower normalized σ_l than the other two alloys. Meticulously, although the overall normalized σ_l of both the 304L and Stellite 21 are almost equal (~ 0.61), Stellite 21 still gives a more uniform distribution. Hence, based only on normalized σ_l results, Stellite 21 would be picked as the final candidate material because it has the least and most uniform normalized longitudinal stress.

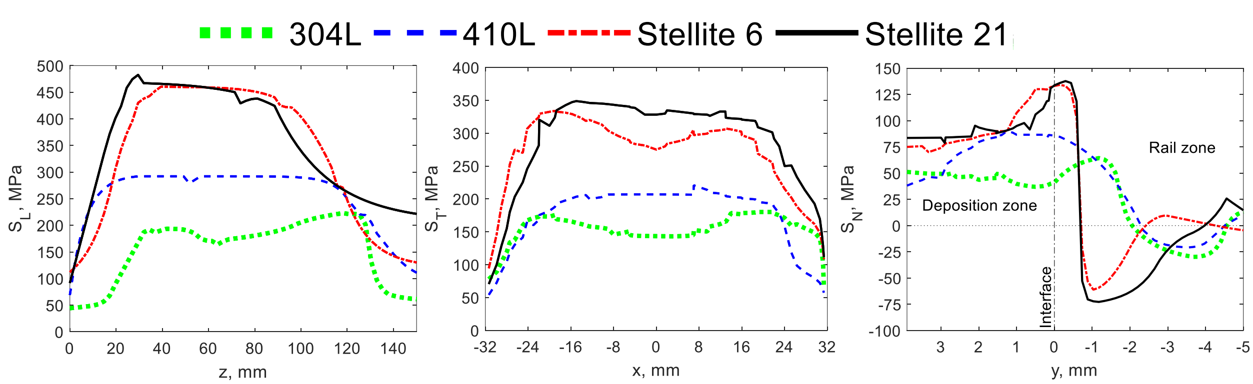

(a) (b) (c)

Fig. 7.5 (a) Longitudinal, (b) transversal, and (c) normal stress distributions along x, z, and y directions, respectively, for the repaired rails with different deposition alloys at the preheating temperature of 600°C. (Refer to Sec. 5.1.1, Fig. 1 for configuration of the coordinate system.)

Regarding normalized σ_t (Fig. 6b), 410L and Stellite 21 contain the minimum average magnitudes of ~0.49. Even concerning uniformity, both 410L and Stellite 21 maintain the same normalized σ_t distribution pattern all along its measuring path. Therefore, if the final decision were made based only on the normalized σ_t results, one could say that 410L and Stellite 21 have the minimum normalized stress and, therefore, are the most compatible materials for repairing rails.

Normalization of σ_n is done by dividing the σ_n values in the deposition area and in the rail area by the average room-temperature yield strength of the deposition material and rail material, respectively. Therefore, Fig. 6c shows that there is a sudden increase towards the rail zone in the normalized σ_n graphs at the rail-deposition interface. The sharpness of this increased gradient and the risk of the deposition layer separation are directly correlated. Thus, in Fig. 6c, if one compares the increased gradient of different graphs at the rail-deposition interface, the likelihood of delamination, from the highest to the lowest, would be 410L, 304L, Stellite 21, and Stellite 6. Concerning the normalized σ_n values, Stellite 6 and Stellite 21 carry more tensile stress in the deposition zone than 304L and 410L. However, at the same time, Stellite alloys experience a higher maximum compressive stress in the rail zone than the stainless steel alloys. In addition, Stellite 21 remains compressive down to the depth of y = -3.8 mm, whereas Stellite 6 switches to tensile sooner at y = -2.3 mm. Hence, in a discussion solely depending on normalized σ_n diagrams, while Stellite 6 gives the lowest risk of delamination, Stellite 21 leads to the longest fatigue life due to the highest and broadest compressive stress distribution.

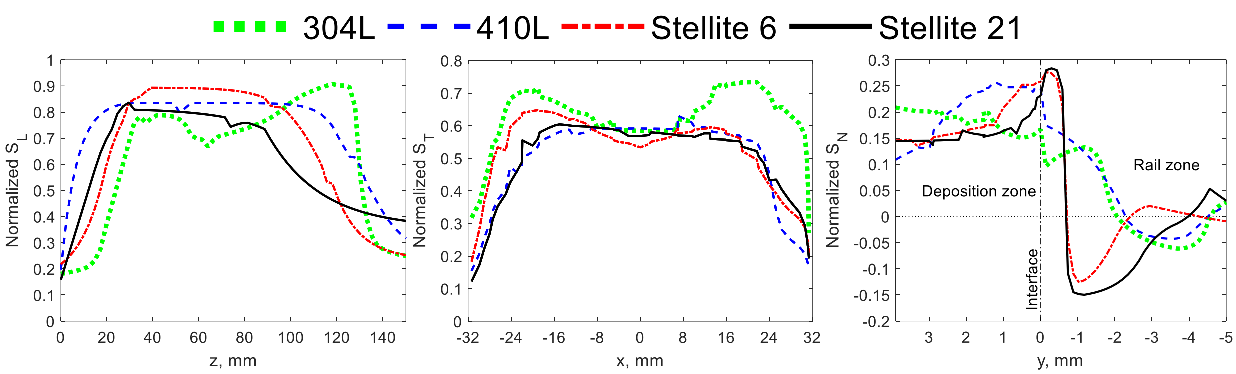

(a) (b) (c)

Fig. 7.6 Normalized (a) longitudinal, (b) transversal, and (c) normal stress distributions along x, z, and y directions, respectively, for the repaired rails with different deposition alloys at the preheating temperature of 600°C. (Refer to Sec. 5.1.1, Fig. 1 for configuration of the coordinate system.)

Even though some deposition materials exhibited acceptable performance in a single normalized stress direction, the material that was recommended in all three stress analyses due to its favorable performance was Stellite 21. The lowest normalized σ_l and σ_t magnitudes in Stellite 21 promise the lowest chance of the crack propagation along the longitudinal and transversal directions at the rail-deposition interface. Also, it was shown that Stellite 21 offers a reduced likelihood of delamination, as well as the longest fatigue life to the repaired rail. Thus, the calculations in the current study indicate that Stellite 21 is the most promising deposition material for repairing a 75-lb standard U.S. light rail with a preheating temperature of 600°C. A lab-scale experimental investigation on a Stellite 21 repaired rail also is recommended as the next phase of a feasibility study in order to examine the microstructure regarding the phase and micro-cracks distribution.

References for Chapter 7

[1] J.X. Fang, S.B. Li, S.Y. Dong, Y.J. Wang, H.S. Huang, Y.L. Jiang, B. Liu, Effects of phase transition temperature and preheating on residual stress in multi-pass & multi-layer laser metal deposition, J. Alloys Compd. 792 (2019) 928-937. https://doi.org/10.1016/j.jallcom.2019.04.104.

[2] T. Roy, Q. Lai, R. Abrahams, P. Mutton, A. Paradowska, M. Soodi, W. Yan, Effect of deposition material and heat treatment on wear and rolling contact fatigue of laser cladded rails, Wear 412–413 (2018) 69–81. https://doi.org/10.1016/J.WEAR.2018.07.001.

[3] T. Mukherjee, W. Zhang, T. DebRoy, An improved prediction of residual stresses and distortion in additive manufacturing, Comput. Mater. Sci. 126 (2017) 360-372. https://doi.org/10.1016/j.commatsci.2016.10.003.

[4] S.C. Cao, A.X.Y. Guo, A novel multiple impact model for predicting the residual stress state, SSRN (2022). https://dx.doi.org/10.2139/ssrn.4102984.

[5] G. Peng, Z. Lu, Y. Ma, Y. Feng, Y. Huan, T. Zhang, Spherical indentation method for estimating equibiaxial residual stress and elastic–plastic properties of metals simultaneously, J. Mater. Res. 33(8) (2018) 884-897. https://dx.doi.org/10.1557/jmr.2018.57.

8. Chapter 8 FLEXURAL AND SHEAR STRENGTH EVALUATION

8.1. Flexural evaluation of the weld materials in SAW-repaired heavy rail

8.1.1. Calculation of flexural and shear stress

Extraction of the bending specimen from the weld materials was described in detail in Sec. 2.3. Putting the sample under bending using the bending test machine, the force-displacement diagram is instantly extracted from the connected computer and shown in Fig. 1.

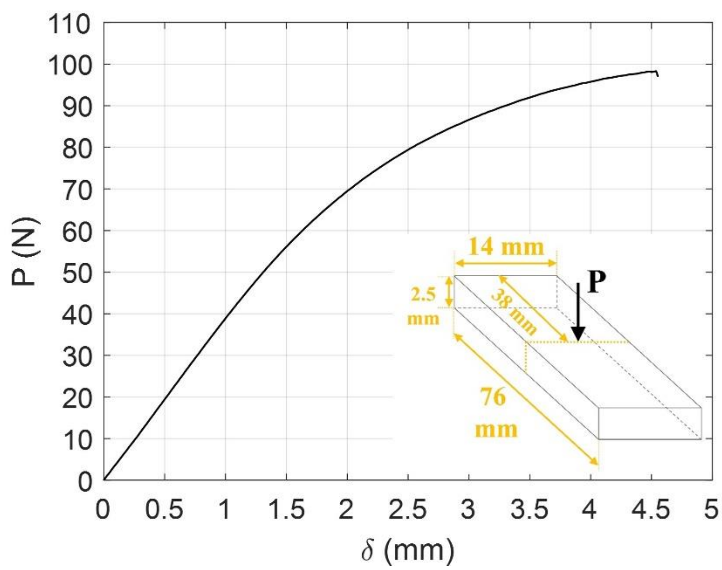

Fig. 8.1 Force (P) – displacement (δ) diagram extracted instantly from 3-point bending test of the thin specimen extracted from the weld materials of the SAW-repaired heavy rail.

To figure out the stress-strain diagram, the force and displacement data need to be transformed to the stress and strain data, respectively. The general scheme of the 3-point bending test setup is shown in Fig. 2. For the current case study of the thin sample, L = 76 mm, b = 14 mm, and h = 2.5 mm (see Sec. 2.3, Fig. 6b for configuration of the dimensions).

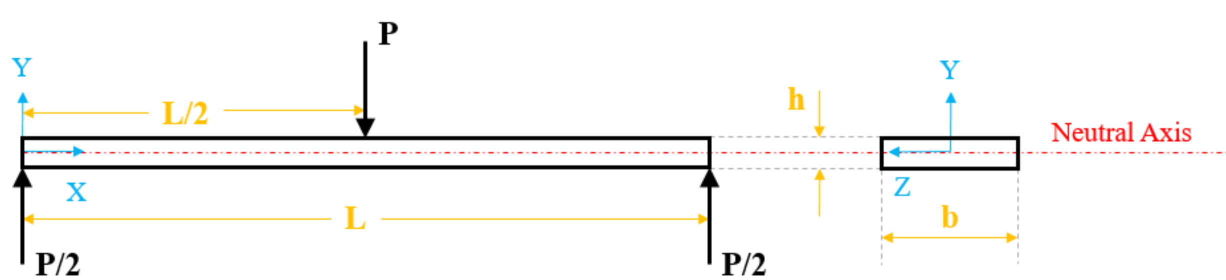

Fig. 8.2 Schematic depiction of the 3-point bending test on the thin specimen extracted from weld materials.

When the P load is applied, the bending stress at the neutral axis is zero. It is seen in Fig. 2 that the neutral axis is located at the middle of the sample cross section, i.e., at a distance of h/2 from the top surface and h/2 from the bottom surface of the sample. Maximum compressive stress occurs at the top surface of the sample (y = h/2 in Fig. 2) and maximum tensile takes place at the bottom surface (y = -h/2 in Fig. 2). A stress distribution contour is shown in Fig. 3 for better clarification.

To calculate the applied maximum stress for any amount of the applied load, the moment and shear distribution in the specimen for any given load of P needs to be expressed. Based on the study by Sideridis and Papadopoulos [1], the maximum shear and bending in a 3-point bending test take place at the center, where the load is applied, with the following values:

$$V_{max} = \frac{P}{2} \tag{1}$$

$$M_{max} = \frac{PL}{4} \tag{2}$$

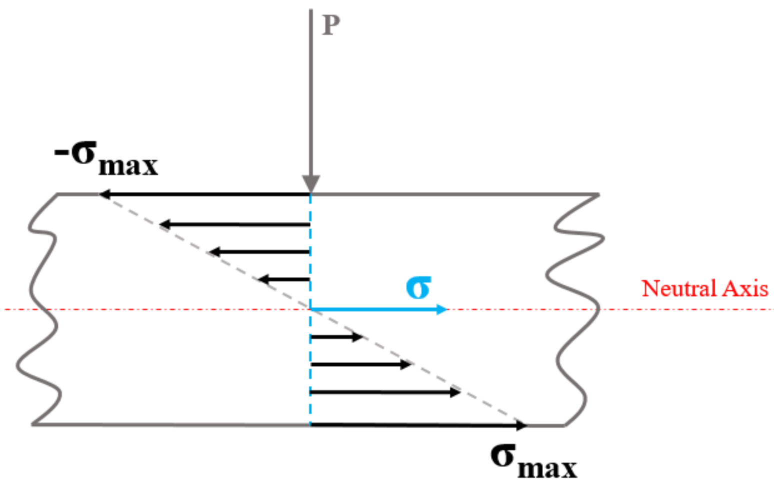

Fig. 8.3 Bending stress distribution at the location of the applied 3-point bending test.

where V_{max} is the maximum shear force, M_{max} is the maximum moment, P is the applied force, and L is the distance between the two supports, which, here, is equal to 76 mm (refer to Sec. 2.3, Fig. 6b). Fig. 4 shows the shear and moment diagrams.

According to [1], the maximum bending stress, σ_{max}, is calculated using the following equation:

$$\sigma_{max} = \frac{M_{max}C}{I} \tag{3}$$

where M_{max} is expressed in Eq. 2, C is the distance from the neutral axis to the top/bottom surface, and I is the sample's moment of inertia. C and I are formulated as:

$$C = \frac{h}{2} \tag{4}$$

$$I = \frac{bh^3}{12} \quad (5).$$

Putting Eqs. 2, 4, and 5 into Eq. 3 results in:

$$\sigma_{max} = \frac{3PL}{2bh^2} \tag{6}$$

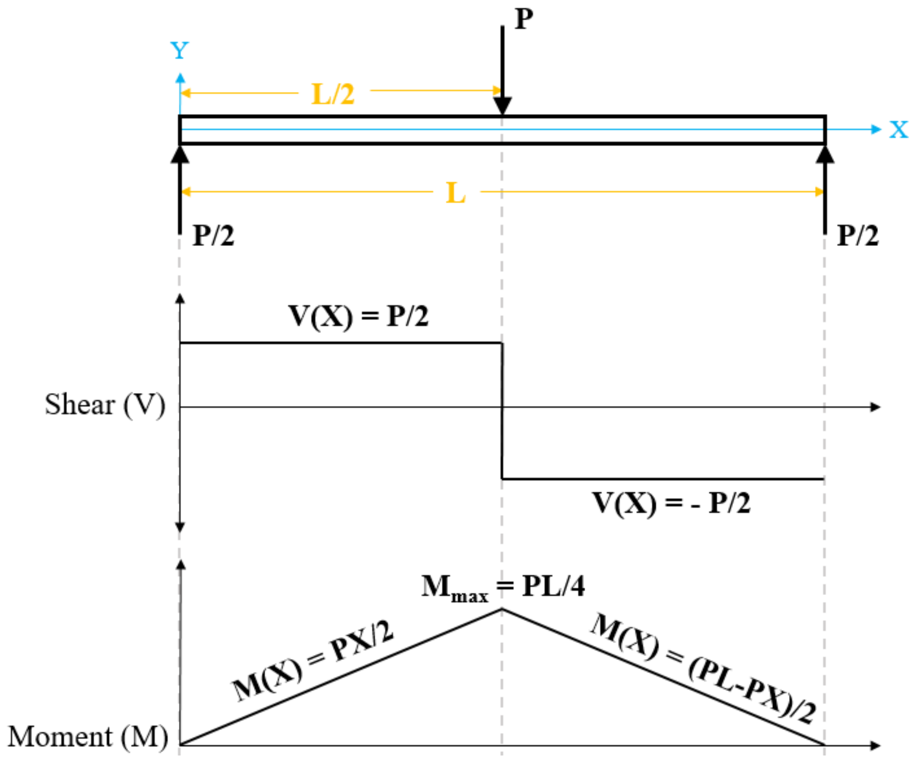

Fig. 8.4 Shear and moment diagrams for the sample under bending load in 3-point bending test.

The shear force (V), results in shear stress, i.e., τ_{xy}, which acts vertically, parallel to the cross section along the y direction. The average shear stress acting on the cross section could be calculated as the shear force (V) divided by the cross-sectional area (A). However, the shear stresses, as the shear flow pattern is shown in Fig. 5, are not distributed uniformly across the cross section of the specimen. As it can be seen in Fig. 5, the shear stress starts at zero at the free top/bottom surfaces, and reaches to its maximum value at the neutral axis. Therefore, as the average shear stress does not reflect the maximum or minimum shear stress, it is not very useful. Instead, the following equation can be used to calculated the shear stress at the cross section:

$$\tau_{xy} = \frac{VQ}{Ib} \tag{7}$$

where V is the applied shear force, Q is the first moment of area, I is the moment of inertia, and b is the width of the cross section. Derivation of this equation is given in [1] and will not be covered here. It should only be noted that it is based on considering equilibrium of stresses acting on small elements within the specimen. The Eq. 7 assumes that the shear stress is constant across the width, i.e., b, of the cross section, and hence the shear stress is a function of the distance along the specimen, i.e., x, and the distance from the neutral axis, i.e., y (refer to Fig. 2 for configuration of the coordinate system and the parameters).

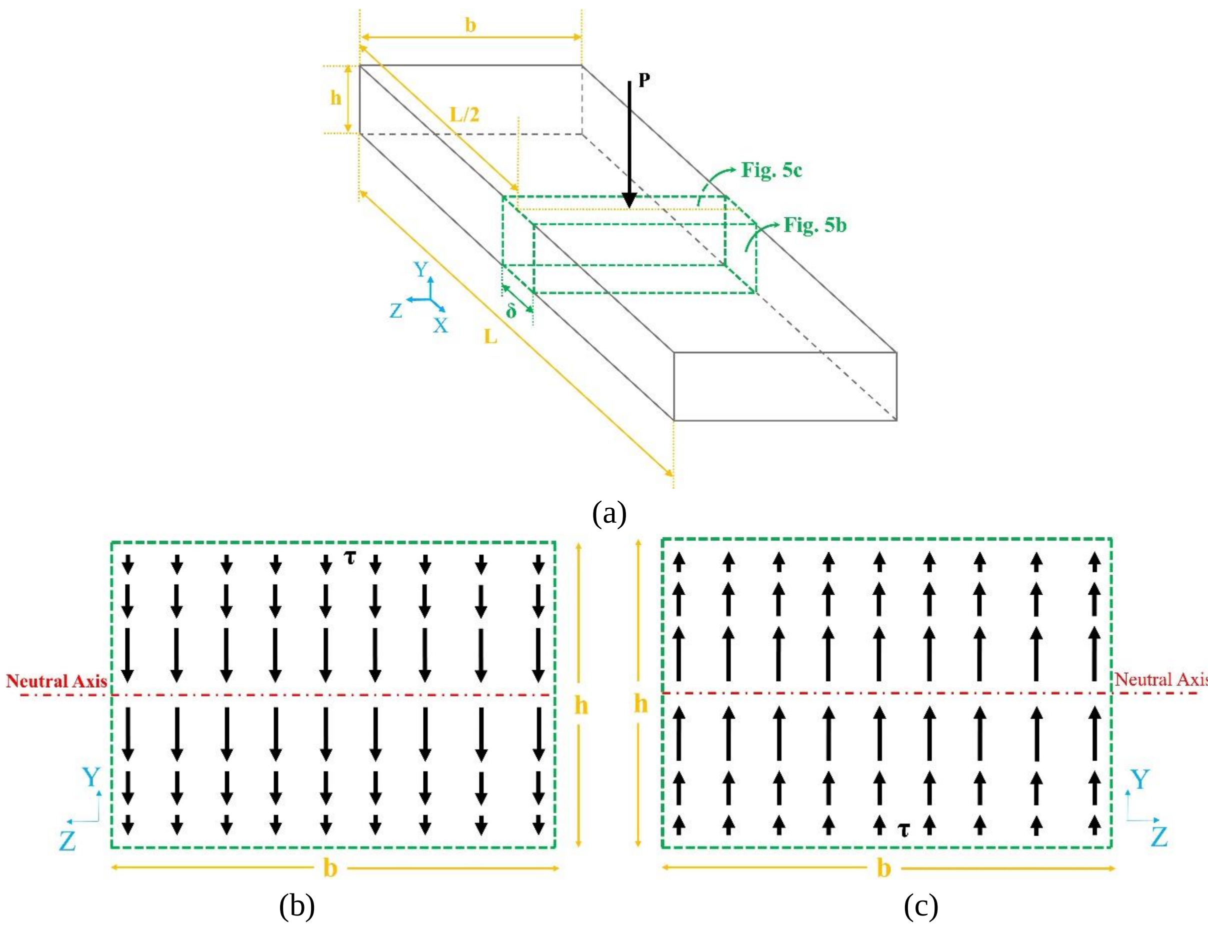

Fig. 8.5 Shear flow diagram at the cross section of the thin bending specimen shown in Fig. 2.

The Q parameter in Eq. 7 is the first moment of area and is equal to:

$$Q = \frac{b}{2}\left(\frac{h^2}{4} - y^2\right) \tag{8}$$

Therefore, at the neutral axis (y = 0), where the maximum shear occurs, the Q is calculated as:

$$Q = \frac{bh^2}{8} \tag{9}$$

Putting Eqs. 1, 5, and 9 into Eq. 7, the maximum shear stress for any given load of P is:

$$\tau_{max} = \frac{3P}{4bh} \tag{10}$$

Further, calculation of strain based on the collected displacement data (δ) is carried out using the following equation:

$$\varepsilon = \frac{6\delta h}{L^2} \tag{11}$$

of which the derivation can be found in [1].

The extracted force-displacement data in Fig. 1 can now be transformed to stress-strain data. The force data (P) are transformed to stress data (σ) using Eq. 6 and considering that L = 76 mm, b = 14 mm, and h = 2.5 mm (refer to Sec. 2.3, Fig. 6b for configuration of the dimensions). The displacement data (δ) are transformed to strain data (ε) using Eq. 11 and considering that h = 2.5 mm and L = 76 mm. The stress-strain diagram is plotted in Fig. 6. It has to be noted that the acquired force-displacement data in Fig. 1 and the stress-strain data in Fig. 6 are taken from the bottom surface of the bending sample, i.e., the surface that is in tension during the 3-point bending test.

Referring to Fig. 6, the slope of the elastic region gives the Young's modulus of the weld material. Therefore, the modulus of elasticity of the weld materials is E = 196 MPa. Using the 0.2%-offset method, where a line parallel with the elastic region is drawn starting from ε = 0.002 mm/mm to intersect with the stress-strain diagram, the yield strength can be figured out. In this way, the stress-strain diagram in Fig. 6 gives the yield strength of the weld material as S_y = 53 MPa. According to the developed standards by AREMA [2], a standard 136RE heavy rail should have a minimum yield strength of 300 MPa. Hence, for the SAW-repaired heavy rail, the yield strength (S_y) is below the minimum requirement by AREMA, and it is concluded that the repaired rail will fail under the dynamic load of the train. The minimum yield strength of a light 75-lb/yd is 210 MPa [2], which is also above the material yield strength of the current weld tested.

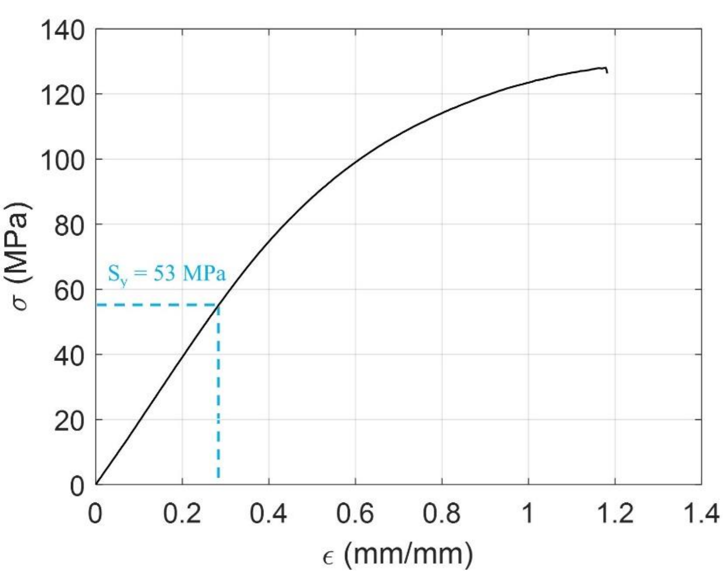

Fig. 8.6 The resultant stress-strain diagram from the 3-point bending test of the thin specimen extracted from the weld materials of the SAW-repaired heavy rail. The related force-displacement diagram is given in Fig. 1.

This kind of interpretation of the results is only valid if the sample is failed only due to bending and not shear. Calculating the shear stress at the breakage point using Eq. 10 gives τ_f = 2 MPa which is very low value compared to the flexural failure stress, i.e., 126 MPa. However, it does not guarantee that the sample did not undergo any shear failure. To carry out the better analysis the broken cross sections of the bending sample are examined using SEM.

Another important factor that is to be analyzed, is the maximum elongation percentage of the specimen at the time of failure. During the 3-point bending test, the bending sample is deflected by an amount of δ, as shown in Fig. 7. The initial length of the sample is L, where the distance between one of the supports to the point of load is L/2, as seen in Fig. 7. Therefore, the final length of the deflected sample, L_2, can be estimated following the Pythagorean theorem:

$$L_2/2 = \sqrt{(L/2)^2 + \delta^2} \tag{12}$$

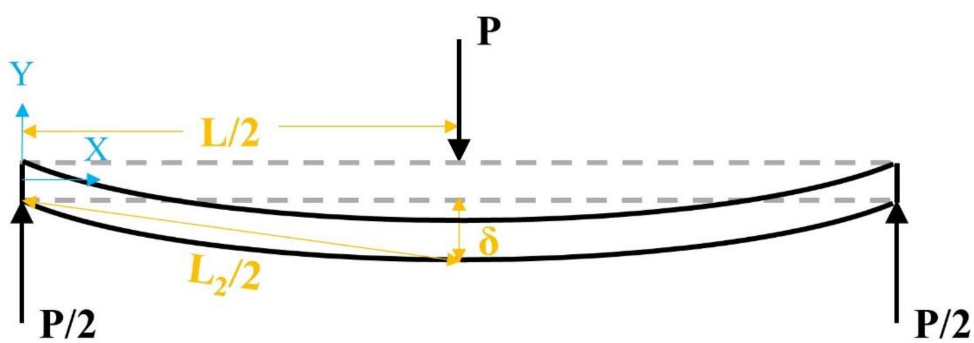

Fig. 8.7 A schematic view of the deflected thin bending specimen.

Therefore, the percentage of the sample elongation can be calculated as follows:

$$Elongation\,\% = \frac{L_2/2 - L/2}{L/2} \times 100 = \frac{L_2 - L}{L} \times 100 \tag{13}$$

Therefore, for the bending sample with the initial length of L = 76 mm and maximum deflection of δ = 4.55 mm, the specimen is elongated 0.71% with the final length of L_2 = 76.54 mm at the time of failure. The elongation is much lower than 5%, which means that the specimen has gone through a brittle failure and the cracks started to propagated at the early stages of deflection.

8.1.2. Failure mode analysis

The fracture surface of the bending specimen is examined by SEM to help clarify and discuss the possible failure mode occurred during the 3-point bending test. Fig. 8 illustrates a clear observation of the fracture surface.

In Fig. 8a, the fracture surface can generally be divided into two regions; the lower region that was under tensile during the 3-point bending test, and the upper region that was under compression during bending. A closer look at the fracture surface in Fig. 8b shows that the light vertical cleavage signs initiate from the lower region, continue to somehow upper than the middle, but do not reach all way to the top. As observable in Fig. 8b, the upper region lacks those cleavage signs; this is probably due to the fact that no fracture has been initiated from the upper region. Besides, looking at the border around the fracture surface in Fig. 8a, the lower horizontal borderline along with the lower section of the right vertical borderline are appeared lighter than the other sections of the borderlines. This, again, confirms the idea of initiation of failure from the lower region, i.e., tensile region. As the compression region mostly lacks any sign of cleavage, there is a rare chance that shear had any part in the fracture of the specimen during 3-point bending test.

It can also be inferred from Fig. 8 that the neutral axis has not been perfectly located in the middle; it has shifted a little bit towards the top surface. This interpretation is because the cleavages are started from the bottom surface and extended to upper than the middle of the fracture surface.

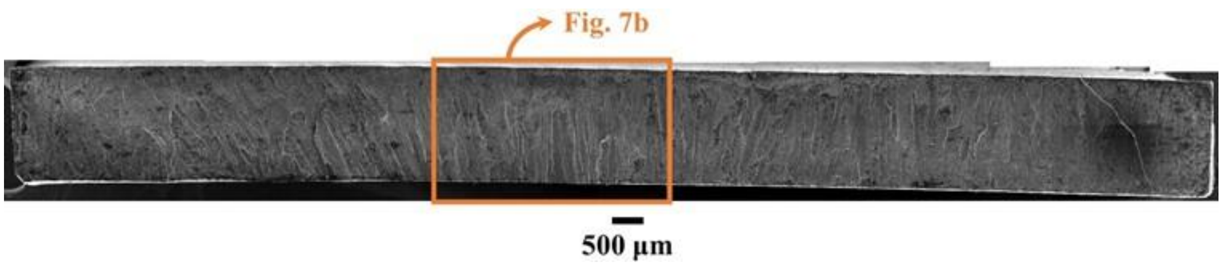

(a)

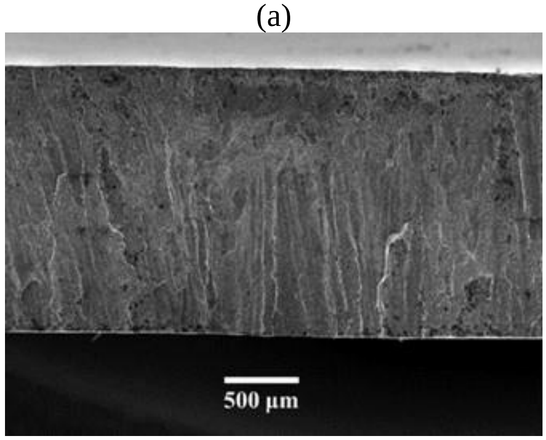

(b)

Fig. 8.8 SEM macrograph from the fracture surface of the 3-point bending specimen; (a) an overall view from the whole fracture surface and (b) a closer view to the surface.

Another visible phenomenon in the fracture surface shown in Fig. 8 are the numerous small and large black-colored sites that might be micro-pores as a result of defective welding, dimples as a result of flexural failure in 3-point bending test, or carbon-concentrated lands due to the inconsistent chemical distribution. To discuss this issue, some of those black islands are scanned using EDS. These typical captured sites along with their corresponding chemical composition are presented in Fig. 9.

The scanned region in Fig. 9e is a typical region with no special signs of black spots or cleavage. This region represents a regular region that most probably presents the regular chemical composition of the weld materials.

On one hand, comparing Figs. 9c and 9g to Fig. 9e shows a quite close chemical composition; although carbon content in Fig. 9g is slightly higher than that for Fig. 9e, they still fairly fall in identical category of carbon content interval. This means that those black islands shown in Figs. 9c and 9g do not represent any carbon-intruded area, and they may represent a dimple or a pore as microstructural deficiency in the weld. Comparing the oxygen content of Fig. 9e against Figs. 9c and 9g, it is seen that the scanned areas of Figs. 9c and 9g contain considerably higher fraction of oxygen than the regular, i.e., than that of Fig. 9e. This strengthens the idea that the black lands in Figs. 9c and 9g are actually representing a pore with some amount of entrapped air.

On the other hand, it is evident that those studied black islands in Figs. 9b, 9d, and 9f have a quite higher carbon concentration than the regular expectation, i.e., the 5.3 wt.% in Fig. 9e. Besides, their oxygen content is fairly close to the regular fraction, i.e., the 2.6 wt.% in Fig. 9e, which almost rejects the hypothesis that these spots might be an air-entrapped pore. Hence, it is inferred that the visible black spots in Figs. 9b, 9d, and 9f show a carbon-concentrated area, and there is a rare chance that they are the signs of some kind of dimple or pore.

All such discovered inconsistencies, i.e., the inconsistent chemical distribution and the micro-pore in the microstructure of the sample, can contribute in shifting the neutral axis from the middle axis towards the top or bottom surface; the fact that was described earlier and is visible in Fig. 8b. Also, the such a low measured yield strength (53 MPa) of the sample as an output of the 3-point bending test is most probably due to all those deficiencies, i.e., the chemical inconsistency and the pores. These deficiencies could lead to the premature failure of the bending specimen. It was found in Sec. 4.2.1 that the weld materials of the SAW-repaired heavy rail have a high hardness in the range of 50 to 60 HRC. Based on the developed relationships by Juvinall and Marshek [6] for estimating the strength properties of a steel from its hardness, the yield strength of a steel can be estimated through the measured hardness using the following equation:

$$S_y = 3.62H_B - 206.84\ MPa \tag{14}$$

where S_y is the yield strength and H_B is the Brinell hardness number. Using the measured hardness data in Se. 4.2.1 and estimating the yield strength using Eq. 14, Table 1 is developed.

Table 5 Estimation of the yield strength of the weld materials of the SAW-repaired rail based on the measured hardness data using the developed relationship by Juvinall and Marshek [6], .i.e., Eq. 14.

Brinell hardness number (H_B)	Yield strength, S_y (MPa)
187	469

175	427
198	511
205	535
218	582
223	602
218	582
223	602
211	558
218	582
218	582
223	602
218	582
223	602

Based on the acquired data in Table 1, it is seen that such a hard weld material should have a yield strength in the order to 500-600 MPa. Therefore, such a low yield strength of the bending specimen (53 MPa) is definitely due to the existing deficiencies in the weld.

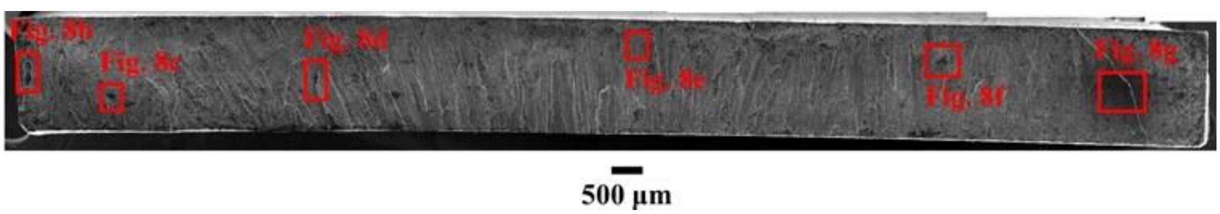

(a)

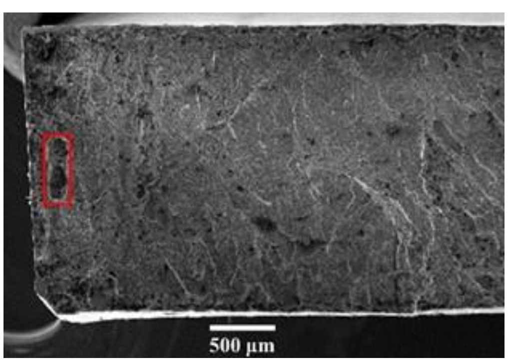

Fe	C	Cr	Mn	Si	O
Bal.	27.4	2.0	1.6	1.4	1.2

(b)

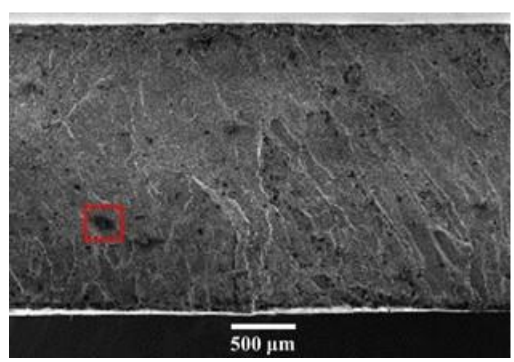

Fe	C	Cr	Mn	Si	O
Bal.	6.4	2.3	2.1	4.61	14.3

(c)

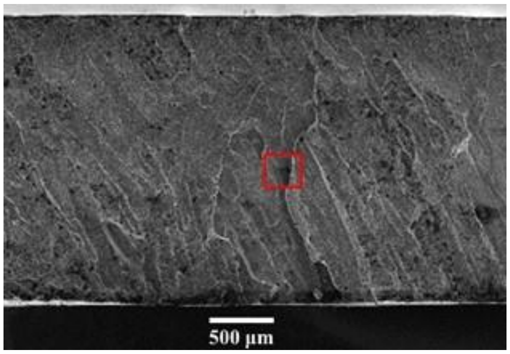

Fe	C	Cr	Mn	Si	O
Bal.	50.9	-	-	-	3.1

(d)

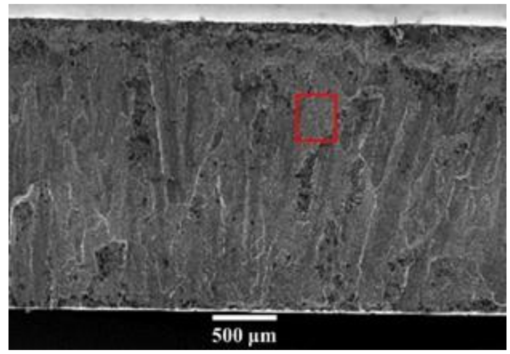

Fe	C	Cr	Mn	Si	O
Bal.	5.3	3.1	2.2	1.21	2.6

(e)

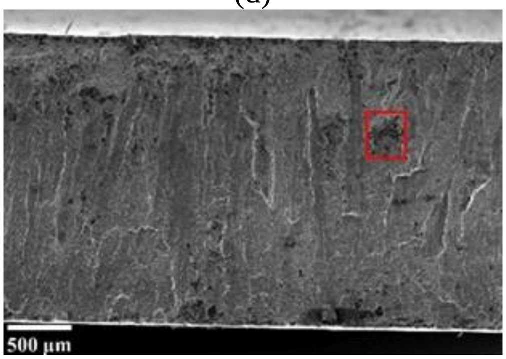

Fe	C	Cr	Mn	Si	O
Bal.	52.95	1.43	1.74	1.13	2.3

(f)

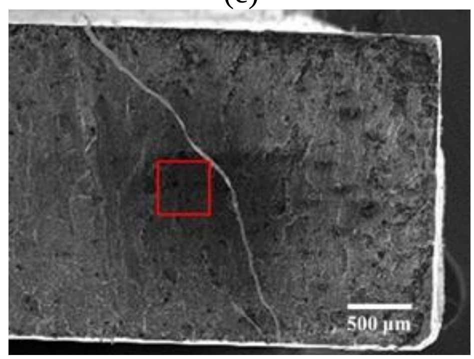

Fe	C	Cr	Mn	Si	O
Bal.	14.7	2.1	1.9	1.5	10.7

(g)

Fig. 8.9 EDS scan analysis of different locations of the fracture surface of the bending specimen to figure out the nature of the observable black islands based on their chemical composition (each chemical element is represented by its wt.%).

8.2. Flexural evaluation at the rail-weld interface in SAW-repaired heavy rail

8.2.1. Calculation of flexural and shear stress

Extraction of the bending specimen from the rail-weld interface was described in detail in Sec. 2.3. The sample is put under bending using the bending test machine in a way that the bending load is applied to the rail side, i.e., the rail side is at the top and mostly under compression, and the weld side is at the bottom and under tensile. The force-displacement diagram is instantly extracted from the connected computer and shown in Fig. 10.

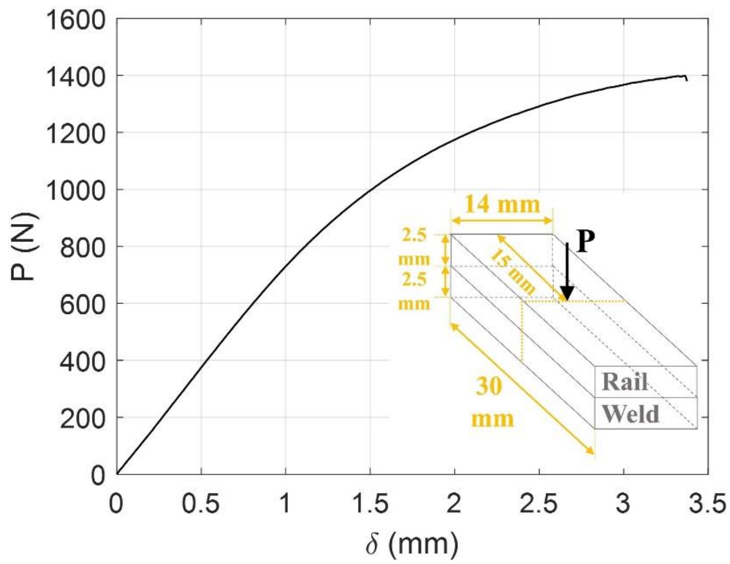

Fig. 8.10 Force (P) – displacement (δ) diagram extracted instantly from 3-point bending test of the thick specimen extracted from the rail-weld interface of the SAW-repaired heavy rail.

The general load setup is like the previous case discussed in Sec. 8.1.1 for the weld sample and shown in Fig. 2, except that the current case is a composite sample, containing rail and weld materials, and hence it should not be assumed in the calculation that the neutral axis will be located exactly at the middle of the cross section. Therefore, Eq. 6, that was presented for a bending specimen with homogeneous material, will not work for the current case. In the rail-weld-interface sample, the mechanical properties between the rail and the weld materials differ, which means that Eq. 6 should be modified.

According to the study by Deng et al. [3], to take into account the plastic deformation in a 3-point bending strength, the typical Eq. 6 needs to be multiplied by a modification factor. According to Deng's recommendation in [3], the following modification factor is good to be considered for the hardfacing steels:

$$\sigma_f = 0.8 \times \left(1 - \frac{4h}{3\pi L}\right) \times \left(\frac{3PL}{2bh^2}\right) \tag{15}$$

For the current specimen that is made of two materials, the tensile/compressive stress determination method needs modification [4]. The offset of the neutral axis from the middle plane, i.e., from the rail-weld interface, needs to be determined. This shifting of the neutral axis (d_{NA}) is illustrated graphically in Fig. 11 for a better clarification.

At the cross section of the specimen during bending, the resultant force should be zero. This fact can be expressed as:

$$\int \sigma_t ds = \int \sigma_c ds \tag{16}$$

where σ_t is the tensile normal stress, and σ_c is the compressive normal stress. The normal stress is generally defined as follows:

$$\sigma = \frac{Ey}{r} \tag{17}$$

with E as the modulus of elasticity, y the distance from the neutral axis, and r the neutral axis curvature. Combining Eqs. 16 and 17 results in:

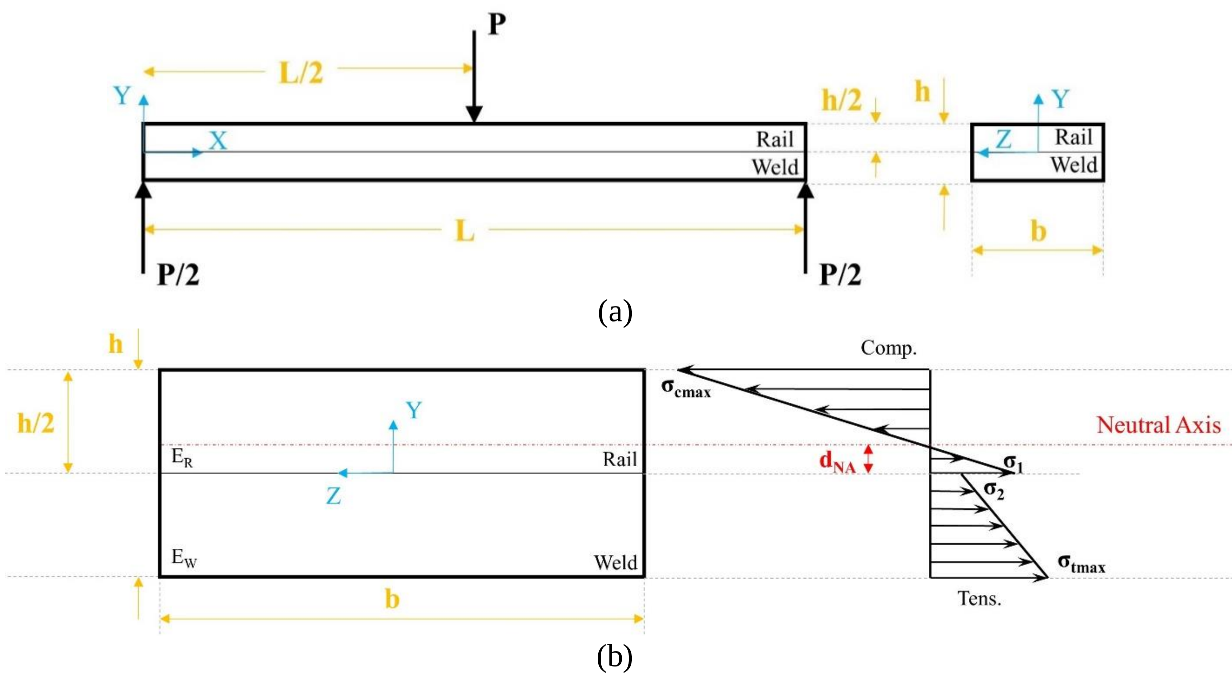

Fig. 8.11 (a) Schematic depiction of the 3-point bending test on the thick specimen extracted from rail-weld interface, and (b) a closer look at the cross section of the specimen in Y-Z plane.

$$\frac{E_R}{2r} \times \left(\frac{h}{2} - d_{NA}\right)^2 = \frac{E_R \times d_{NA}{}^2}{2r} + \frac{h}{4} \times \left(\frac{E_W \times d_{NA}}{r} + \frac{E_W \times (d_{NA} + h/2)}{r}\right) \tag{18}$$

where E_R and E_W represent the modulus of elasticity of the rail and the wheel, respectively, h is the thickness of the thick bending specimen, and d_{NA} is the distance of the shifted neutral axis from the middle plane (see Fig. 11 for a graphical sense of the parameters). The neutral axis offset (d_{NA}) can be derived from Eq. 18 as follows:

$$d_{NA} = \frac{h(E_R - E_W)}{4(E_R + E_W)} \tag{19}.$$

For a unit magnitude of the bending force, i.e., P = 1, the applied stress at the rail-weld interface in the rail area can be expressed as (see Fig. 11):

$$\sigma_1 = \frac{d_{NA}}{h/2 - d_{NA}} \tag{20}$$

the applied stress at the rail-weld interface in the weld area is (see Fig. 11):

$$\sigma_2 = \frac{E_W d_{NA}}{E_R(h/2 - d_{NA})} \tag{21}$$

and the maximum flexural tensile stress at the bottom surface of the weld is (see Fig. 11):

$$\sigma_{tmax} = \frac{E_W(h/2 + d_{NA})}{E_R(h/2 - d_{NA})} \tag{22}.$$

Hence, the resulting moment at the cross-sectional plane of the bending specimen can be formulated as follows (see Fig. 11):

$$\begin{aligned} M_0 &= \int_{d_{NA}}^{h/2} \frac{y}{(h/2 - d_{NA})} bydy + \int_{-h/2}^{d_{NA}} \frac{E_W}{E_R} \frac{y}{(h/2 - d_{NA})} bydy \\ &= \frac{b}{3(h/2 - d_{NA})} \left(\left(h^3/8 - d_{NA}{}^3 \right) + E_W/E_R \left(h^3/8 + d_{NA}{}^3 \right) \right) \end{aligned} \tag{23}.$$

Based on what was discussed in Sec. 8.1.1 and shown in Fig. 4, the maximum applied bending in a 3-point bending test is PL/4. Therefore, the failure flexural tensile stress (σ_f) is:

$$\sigma_f = \sigma_{tmax} \times \frac{PL/4}{M_0} = \frac{PL}{4} \times \frac{1}{M_0} \times \frac{E_W(h/2 + d_{NA})}{E_R(h/2 - d_{NA})} \tag{24}.$$

Combining the modification factor for plastic deformation, that was presented in Eq. 15, with Eq. 24, the failure bending strength is:

$$\sigma = 0.8 \times \left(1 - \frac{4h}{3\pi L}\right) \times \frac{PL}{4} \times \frac{1}{M_0} \times \frac{E_W(h/2 + d_{NA})}{E_R(h/2 - d_{NA})} \tag{25}.$$

As it was shown in Secs. 6.1.3 and 8.1.2, the elastic moduli of the weld and rail materials are E_W = 196 MPa and E_R = 210 MPa, respectively. To provide a strict reference, the elastic moduli of the heavy and light rails, deposited weld materials on the current bending specimen, and the Lincore-40S weld wire are listed in Table 2. As it was described in Sec. 2.3, the thick bending sample extracted from the rail-weld interface has a thickness of h = 5 mm. Putting these parameters into Eq. 19 gives the neutral axis offset equal to d_{NA} = 0.04 mm. Considering that the thick bending specimen has a width of b = 14 mm, from Eq. 23 it can be calculated that M_0 = 57.31 mm^3. It was illustrated in Sec. 2.3, Fig. 6d that a span length of L = 30 mm is put between the supports. Having all these parameters along with the recorded failure load of P = 1398.91 N in the 3-point bending test of the thick specimen (Fig. 10), the failure bending stress can be calculated using Eq. 25, which is equal to:

$$\sigma_f = 131\ MPa \qquad (26).$$

Now, using Eq. 25, the extracted force-displacement data in Fig. 10 can be transformed to stress-strain data. The displacement data (δ) are transformed to strain data (ε) using Eq. 11 and considering that h = 2.5 mm and L = 30 mm. The stress-strain diagram is plotted in Fig. 12. It has to be noted that the acquired force-displacement data in Fig. 10 and the stress-strain data in Fig. 12 are taken from the bottom surface of the bending sample, i.e., the weld surface that is in tension during the 3-point bending test.

Referring to Fig. 12, the slope of the elastic region gives the Young's modulus of the weld material. Therefore, the modulus of elasticity of the weld materials is E = 182 MPa, which is fairly close to the gained Young's modulus from the thin specimen. Using the 0.2%-offset method, where a line parallel with the elastic region is drawn starting from ε = 0.002 mm/mm to intersect with the stress-strain diagram, the yield strength can be figured out. In this way, the stress-strain diagram in Fig. 12 gives the yield strength of the weld material as S_y = 57 MPa, which is almost a perfect match to the measured yield strength from the thin specimen. According to the developed standards by AREMA [2], a standard 136RE heavy rail should have a minimum yield strength of 300 MPa. Hence, for the SAW-repaired heavy rail, the yield strength (S_y) is below the minimum requirement by AREMA, and, again, it is concluded that the repaired rail will fail under the dynamic load of the train.

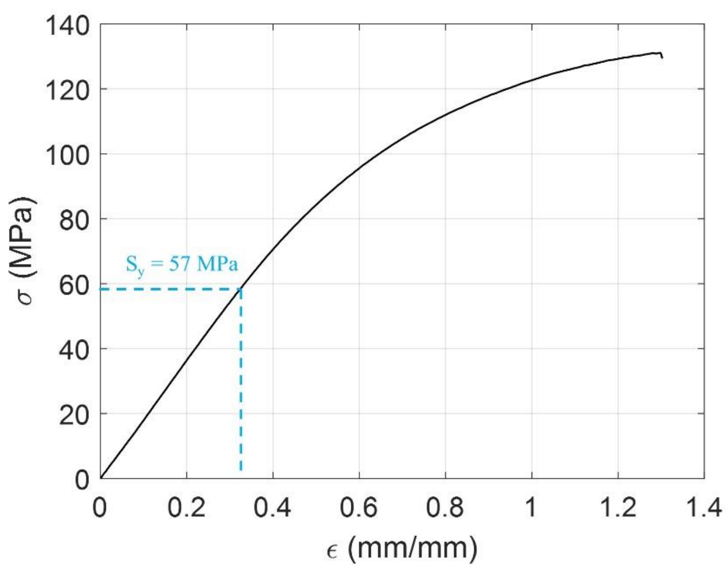

Fig. 8.12 The resultant stress-strain diagram from the 3-point bending test of the thick specimen extracted from the rail-weld interface of the SAW-repaired heavy rail. The related force-displacement diagram is given in Fig. 10.

Regarding the shear stress, as was given in Eq. 7, it is calculated as τ = VQ/Ib. It was presented in Fig. 4 that the maximum shear force during a 3-point bending test is:

$$V = \frac{P}{2} \tag{27}$$

Table 6 Young's modulus of the rail and weld materials.

Material	Heavy rail	Light rail	Deposited weld	Lincore 40-S weld wire
Yield strength (MPa)	210	203	196	185

By dividing the cross section of the thick bending sample shown in Fig. 11b into 3 areas, an area division can be provided as illustrated in Fig. 13, which is ideal for calculating the first moment of area (Q). Referring to Fig. 13, the first moment of area of the thick bending specimen can be calculated as [4]:

$$\begin{aligned} Q &= A_1y_1 + A_2y_2 + A_3y_3 \\ &= \left(b\left(\frac{h}{2} - d_{NA}\right)\right)\left(\frac{1}{2}\left(\frac{h}{2} - d_{NA}\right)\right) + (bd_{NA})\left(\frac{d_{NA}}{2}\right) \\ &+ \left(\left(b\frac{E_R}{E_W}\right)\left(\frac{h}{2}\right)\right)\left(\frac{1}{2}\left(\frac{h}{2} + d_{NA}\right)\right) \\ &= \frac{b}{2}\left(2d_{NA}{}^2 + \frac{h^2}{4}\left(\frac{E_R}{E_W} + 1\right) + hd_{NA}\left(\frac{E_R}{2E_W} - 1\right)\right) \end{aligned} \tag{28}$$

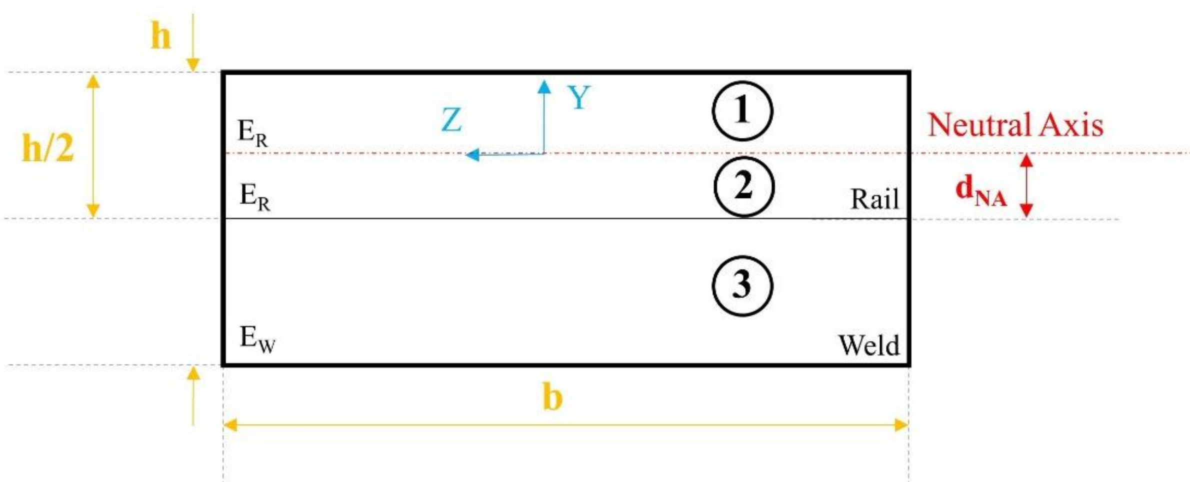

Fig. 8.13 Cross section of the bending specimen divided into 3 zones as a reference for calculation of the first moment of area and moment of inertia.

Referring to Fig. 13, the equivalent moment of inertia (I) for the composite thick bending specimen can be calculated as follows [4]:

$$
\begin{aligned}
I &= \left(I_1 + A_1 {d_1}^2\right) + \left(I_2 + A_2 {d_2}^2\right) + \left(I_3 + A_3 {d_3}^2\right) \\
&= \left[\frac{b\left(\frac{h}{2} - d_{NA}\right)^3}{12} + \left(b\left(\frac{h}{2} - d_{NA}\right)\right)\left(\frac{1}{2}\left(\frac{h}{2} - d_{NA}\right)\right)^2\right] \\
&+ \left[\frac{b{d_{NA}}^3}{12} + (bd_{NA})\left(\frac{d_{NA}}{2}\right)^2\right] \\
&+ \left[\frac{\left(b\frac{E_R}{E_W}\right)\left(\frac{h}{2}\right)^3}{12} + \left(b\frac{E_R}{E_W}\left(\frac{h}{2}\right)\right)\left(\frac{1}{2}\left(\frac{h}{2} + d_{NA}\right)\right)^2\right]
\end{aligned}
\quad (29).
$$

Putting Eqs. 27, 28, and 29 into Eq. 7, and replacing all the parameters with their corresponding values defined for the thick bending specimen extracted from the rail-weld interface, the failure shear stress can be calculated as:

$$\tau_f = 84\ MPa \quad (30).$$

For the thick sample with a length of L = 30 mm and maximum deflection of δ = 3.37 mm, using Eqs. 12 and 13 it is calculated that the sample is elongated 2.5% with the final length of L_2 = 30.75 mm at the time of failure. Although the elongation percentage if much higher for this sample compared to the thin sample, it is still less than 5% and therefore gives the fact that the sample has most probably experienced a brittle failure.

8.2.2. Failure mode analysis

It was found in the last section that at the failure point of the thick bending specimen, a 131 MPa of flexural tensile stress (Eq. 26) and an 84 MPa of shear stress (Eq. 30) are applied simultaneously. What is to be discussed here is about the percentage of contribution of each type of stress in the resulting fracture, i.e., to find out if the thick specimen is ultimately failed as a result of pure bending, as a result of pure shear, or as a combined result of both of them.

Generally, the shear strength of a high-carbon hard steel alloy is about 0.7 of its tensile strength [5]. For the current under-investigation thick specimen, it is found that is has a 131 MPa of flexural tensile stress. Therefore, following Лошак's findings [5], it should have a shear strength around 0.7×131 = 92 MPa. The 3-point bending test showed that the specimen was carrying a shear stress of 84 MPa at the moment of failure, which gives a great chance of shear stress contribution in its ultimate failure/fracture. Figuring out the principal stresses, as shown in Fig. 14, it is seen that the maximum shear stress is 106.5 MPa, which goes beyond the expected shear strength of 92 MPa. This supports the idea of shear involvement in the fracture of the thick bending specimen.

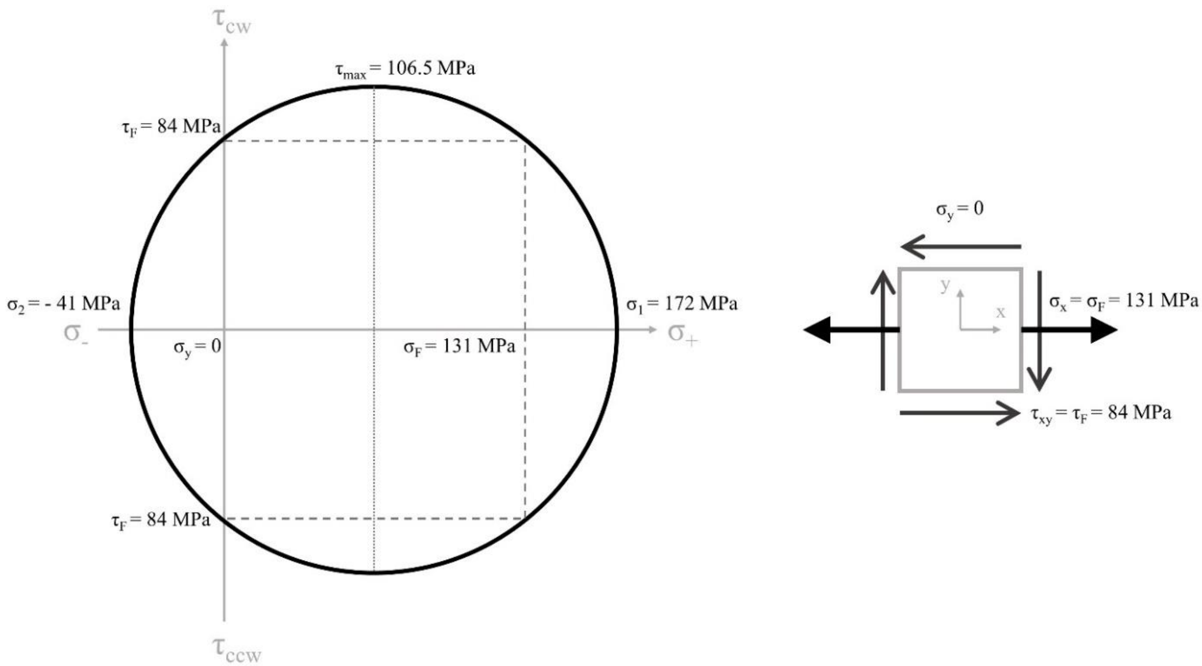

Fig. 8.14 Mohr's circle drawn based on the applied plane and shear failure stresses to the thick bending specimen extracted from the rail-weld interface.

The fracture surface of the thick bending specimen extracted from rail-weld interface is captured using SEM and shown in Fig. 15. It is observable in Fig. 15a that the lower half of the fracture surface, i.e., the weld side, is populated by massive amount of cleavage signs with light appearance. These mostly vertical light-colored lines of cleavage have a very sparse distribution in the upper half, i.e., the rail side, compared to the lower weld side. These cleavage signs show that the normal flexural tensile stress in the weld region was a pivotal contributor of the specimen failure during the 3-point bending.

The other visible fact in Fig. 15a is an elongated sign of combined cleavage and crack at the right side of the fracture surface that is developed in the middle plane of the sample, i.e., at the rail-weld interface. A closer look into it in Fig. 15b shows minor signs of cracks around the elongated cleavage line. These symptoms give a strong evidence that shear stress was also partially involved in the fracture of the specimen at the failure point.

It is concluded that the repaired rail can tolerate shear stresses up to 84 MPa at the rail-weld interface before facing any failure, and the weld material on the top have a tensile bending strength of 131 MPa, which is below the minimum 450 MPa ultimate tensile strength required for the heavy 136RE rails [2].

In Fig. 9, the chemical distribution at different points of the weld materials were scanned to show if the existing black spots are representing a pore, air trap, or a carbon intruded site. It was found that these pores and air bubbles are the main reasons of such a low yield strength and the premature failure of the bending sample. To make sure that this is a valid conclusion, the rail section is also chemically scanned using EDS to check the chemical consistency through the rail material. Fig.

16 shows a random EDS scan of the thick bending specimen at different points of the rail side, i.e., the compression side. It is observable that the despite a slight deviation of the weight percentage of each element between different sites (less than 5%), there is a consistent chemical distribution throughout the entire rail section. This confirms the fact that the weld material suffers from an inconsistent structure which was the reason of neutral axis shifting in the thin bending specimen, and premature failure of both the thin and the thick bending specimens.

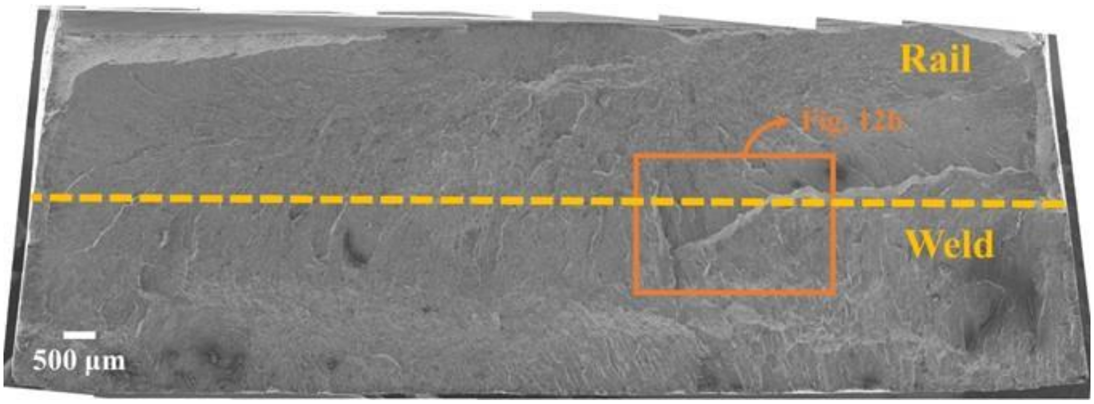

(a)

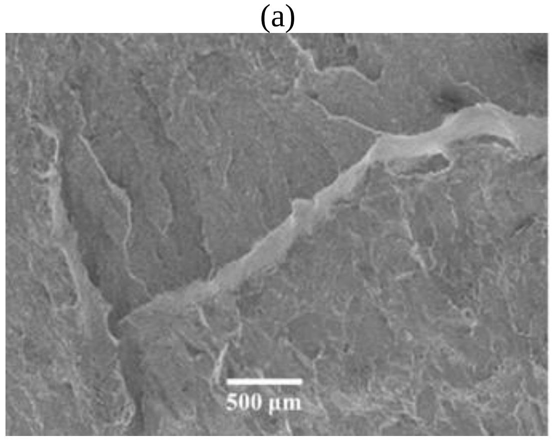

(b)

Fig. 8.15 SEM macrograph from the fracture surface of the thick 3-point bending specimen extracted from the rail-weld interface; (a) an overall view from the whole fracture surface and (b) a closer view to the surface.

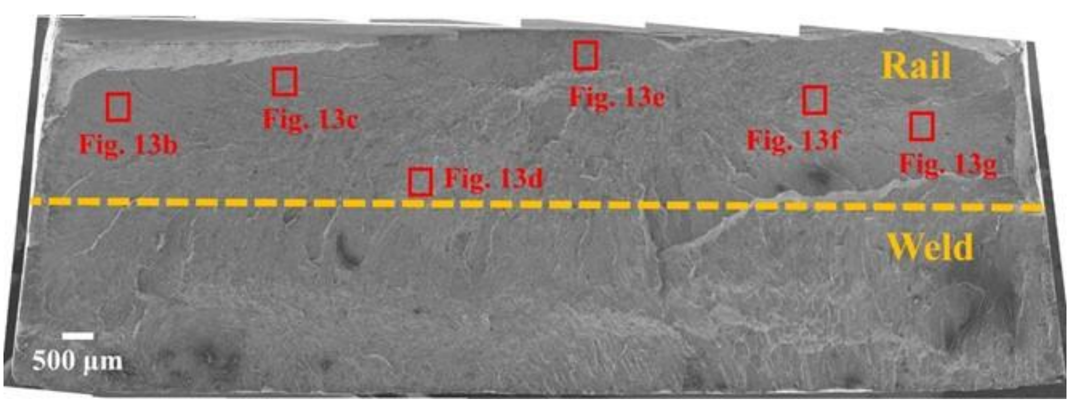

(a)

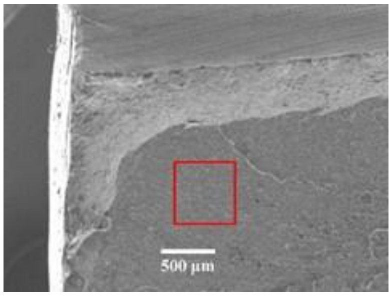

Fe	C	Cr	Mn	Si	O
Bal.	13.7	2.0	3.8	1.0	2.0

(b)

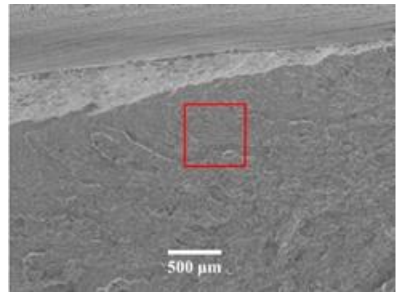

Fe	C	Cr	Mn	Si	O
Bal.	1.8	2.3	2.5	0.5	2.6

(c)

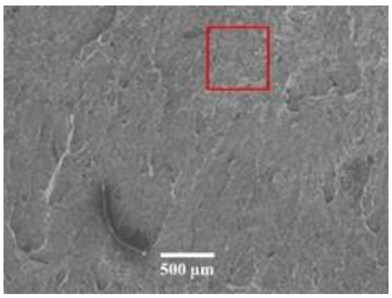

Fe	C	Cr	Mn	Si	O
Bal.	8.97	2.5	3.3	0.8	1.4

(d)

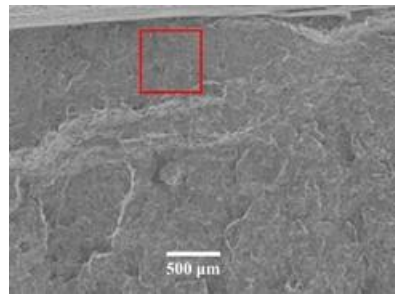

Fe	C	Cr	Mn	Si	O
Bal.	13.42	0.8	3.1	0.5	4.4

(e)

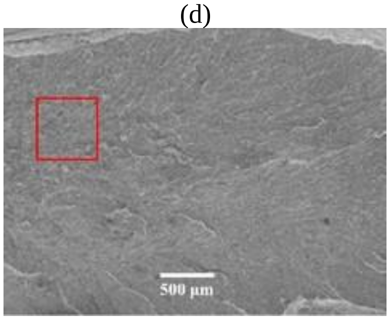

Fe	C	Cr	Mn	Si	O
Bal.	12.9	2.0	3.4	0.3	2.4

(f)

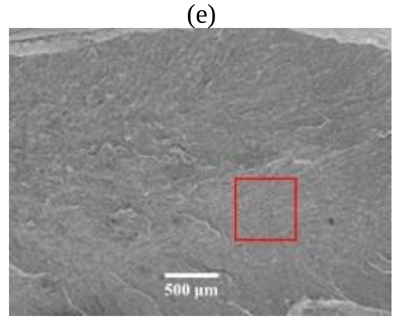

Fe	C	Cr	Mn	Si	O
Bal.	9.62	1.7	2.9	0.4	1.8

(g)

Fig. 8.16 EDS scan analysis of random locations of the upper side of the fracture surface of the thick bending specimen to figure out the chemical consistency of the rail material compared to that of the weld material shown in Fig. 9 (each chemical element is represented by its wt.%).

To get a clearer visualization regarding the chemical consistency throughout the rail and weld areas, the given data in Figs. 9 and 16 are re-presented in the form of graphs in Fig. 17. Each chemical element is presented in a separate graph. The y-axis of each graph shows the weight percentage of the chemical element, and the x-axis shows the location of measuring the weight percentage of the chemical element in Figs. 9 and 16; for example, the measurement location b for C graph in Fig. 17 means the weight percentage of C that was measured for weld in Fig. 9b and for rail in Fig. 16b. An overall look at Fig. 17 shows how sensibly the weight percentage of each individual chemical element goes through sharp fluctuations for the weld material, while the rail material experiences a smooth distribution for every individual element at different locations of measurement; this fact is especially more observant for carbon, silicon and oxygen elements in Fig. 17. The presented graphs in Fig. 17 are put together in a single graph in Fig. 18 for a clearer demonstration regarding the elements with the most fluctuations. One can conclude from Fig. 18 that the carbon and oxygen are those elements that their weight percentage fluctuates greater than the other elements. The reason for oxygen oscillations can be attributed to the presence of air bubbles and air-entrapped holes in the deficient weld structure. The significant oscillation of carbon may be due to the high carbon content of the weld wire, flux particles, and the rail. When these three high-carbon components fuse together during submerged arc welding, then the carbon content near the rail area might be higher as a result of rail's carbon diffusion into the weld microstructure. This again confirms the chemical inconsistency in the weld material, while the rail has a plain chemical distribution. This metallurgical inconsistency in the weld zone could be the major contributor of the premature failure during the 3-point bending test.

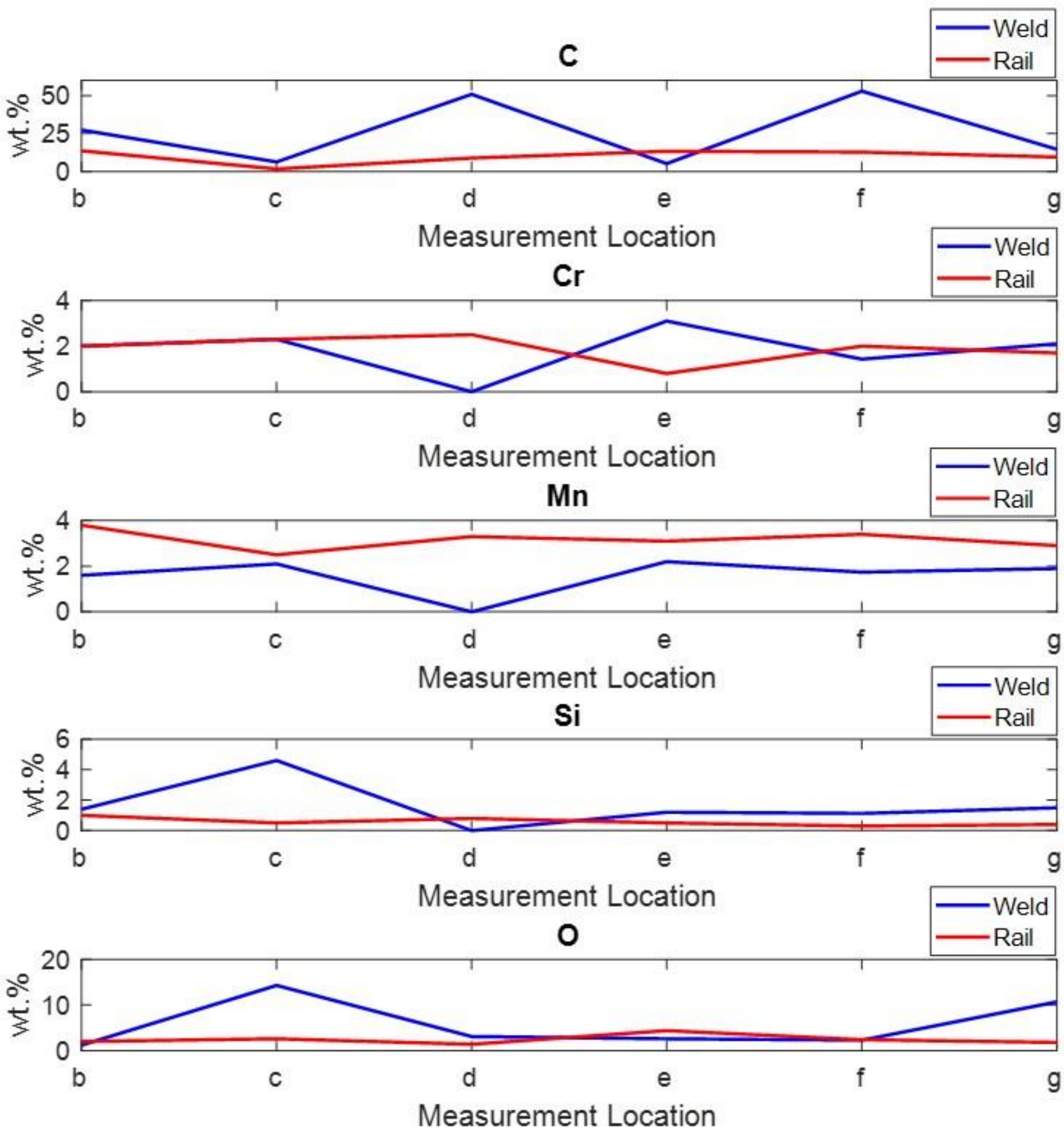

Fig. 8.17 Distribution of the weight percentage of different chemical elements in separate graphs throughout the weld and rail areas. The b-g measurement locations on the x-axis correspond to the locations where EDS chemical measurement is conducted, as shown in Figs. 9b-g and Figs. 16b-g for the weld and rail materials, respectively.

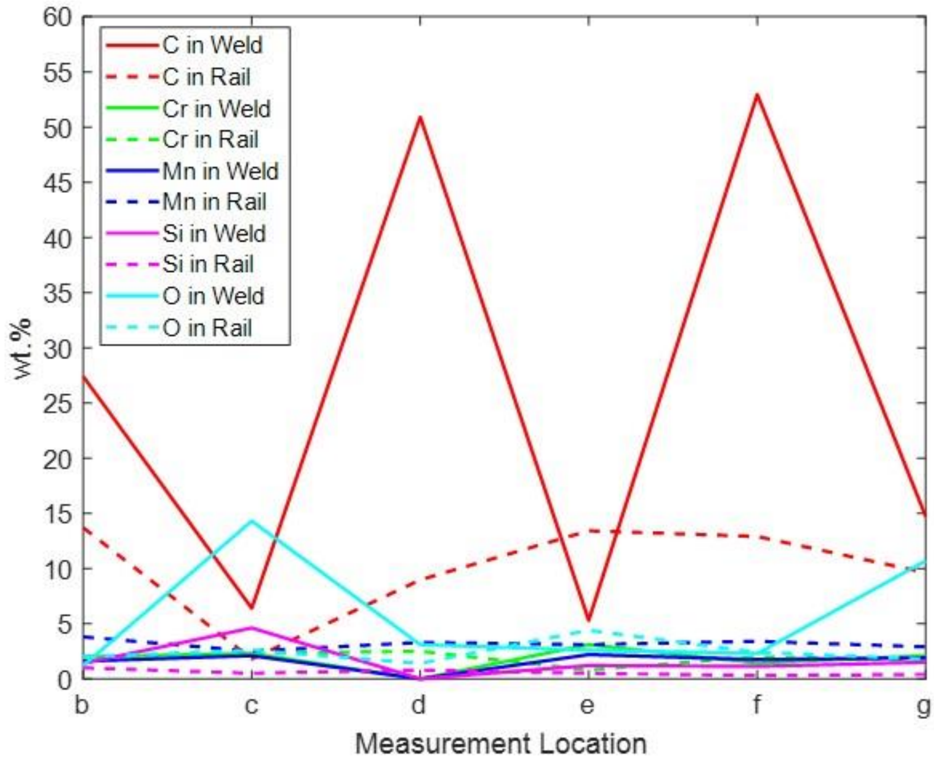

Fig. 8.18 Distribution of the weight percentage of different chemical elements in a single graph throughout the weld and rail areas. The b-g measurement locations on the x-axis correspond to the locations where EDS chemical measurement is conducted, as shown in Figs. 9b-g and Figs. 16b-g for the weld and rail materials, respectively.

The presented experiments in Chapter 8 could give valuable results and could act as a great bedrock to find the best next step for modifying and improving the rail properties. However, all the results and discussions in Secs. 8.1 and 8.2 are only based on a single thin bending specimen and a single thick bending specimen, respectively. This makes the results unreliable. In order to validate the results, all the testing procedures need to be repeated for at least another 2 times, for each of the thin and thick specimens separately. In this way, after comparing the results and making sure of the test repeatability, the validated outcomes can be utilized for the next step of the experiments.

References for Chapter 8

[1] E. Sideridis, G.A. Papadopoulos, Short-Beam and Three-Point-Bending Tests for the Study of Shear and Flexural Properties in Unidirectional-Fiber-Reinforced Epoxy Composites, Wiley InterScience (2003). https://doi.org/10.1002/app.20382

[2] AREMA Manual for Railway Engineering, Chapter 4: Rail, American Railway Engineering and Maintenance-of-way Association (2020)

[3] H. Deng, H. Shi, S. Tsuruoka, Influence of coating thickness and temperature on mechanical properties of steel deposited with Co-based alloy hardfacing coating, Surf. Coat. Technol. 204(23) (2010) 3927-3934. https://doi.org/10.1016/j.surfcoat.2010.05.013

[4] F.P. Beer, J.E. Russel Johnson, Mechanics of materials, McGraw-Hill (2014) 7th edition.

[5] М.Г. Лошак, Strength and fatigue life of hard alloys, Metallurgical Industry Press (1990) 1th edition.

[6] R.C. Juvinall, K.M. Marshek, Fundamentals of machine component design, John Wiley & Sons (2012) 5th edition.

9. Chapter 9 MODIFIED FINITE ELEMENT MODELING AND VALIDATION OF SUBMERGED ARC WELDING FOR REPAIRING 136RE HEAVY RAILS

The constant wear and tear experienced by rail surfaces due to continuous loading necessitates repairs for maintaining optimal performance within railway networks. Traditional repair methods are not only time-consuming but also costly, motivating the exploration of innovative alternatives. This study focuses on the development of a finite element (FE) model to simulate the submerged arc welding (SAW) process, which serves as an additive manufacturing technique for restoring 136-lb/yd (136RE) rails, commonly utilized in heavy freight and passenger rail systems across the United States.

To validate the developed FE model, a series of experimental laboratory investigations were conducted. A worn section of the 136RE rail was carefully chosen for this study. After the rail's surface underwent milling and flattening, the submerged arc welding process was employed to rebuild the rail, utilizing a 1/8-inch Lincore 40-S depositing wire. The reconstructed rail sample was then subjected to experimental tests, including tensile testing, which provided the essential mechanical properties required to validate the simulation process.

The FE model encompasses all conceivable interactions, including thermal, mechanical, and phase transformations. This simulation employs an element-birth-and-kill method, examining the thermal distribution within the sample across different sections. By considering the thermal history and phase change relations, the model predicts the mechanical properties of the repaired rail. The validated model showcases substantial potential in exploring and predicting mechanical properties and thermal distribution during the SAW process for heavy rail repair.

Introduction

Rail tracks' durability is influenced by wear and rolling contact fatigue [1]. Various types of damages commonly arise on railway tracks, predominantly attributable to side wear, fatigue cracks, head checks, and spalling [2]. Switches, crossings, and curves are particularly prone to side wear, making their maintenance expenses significantly higher compared to straight sections of rail tracks. The primary cause of defects in rail tracks, mainly side wear, is the combination of normal and tangential stresses. Consequently, numerous studies have been undertaken to analyze and model the forces, moments, and contact area at the wheel/rail interface [3]–[7]. Rail defects have the potential to initiate and propagate cracks, ultimately causing spalling and, in severe cases, complete rail fracture. Consequently, another line of research has embraced rail grinding as a method to eliminate surface defects and prevent the progression of such cracks [8]–[10]. The grinding process can adversely affect rail longevity and increase operational costs [11], [12].

In response to the limitations of cost and weight in manufacturing rail profiles with high resistance to wear and rolling contact fatigue, the utilization of surface coatings as a form of surface treatment has gained prominence. Various surface coating technologies, such as shielded metal arc welding (SMAW), have been developed as alternative approaches based on specific applications and coating types. For instance, Saiful Akmal and Wahab researched the application of SMAW for repairing damaged surfaces of UIC-54 rails in the Malaysian railway network [13]. De Becker et al. [14] are also developing a mobile system for automated on-site repair of the railway network in the United Kingdom. Kabo et al. [15] developed a numerical model to examine the rolling contact fatigue performance and material defects in weld-repaired rails in Sweden. Furthermore, Xin et al. [16] conducted a valuable numerical study in the Netherlands, investigating repair welding and grinding of standard European rails using finite element modeling.

Regarding studying standard rails utilized in the United States railway system, the current research group is the sole entity concentrating on repairing them through overlay weld techniques. Previous investigations in the United States have explored laser cladding to repair damaged surfaces in both light transit rails [17], [18] and heavy freight/passenger rails [19]. Another research endeavor examined submerged arc welding (SAW) applications for repairing light rails [20]. This present study represents the first examination of the mechanical and metallurgical properties of a standard U.S. heavy rail undergoing SAW repair.

Repairing a damaged railhead surface offers significant advantages over conventional replacement methods, primarily due to its ease of implementation and avoiding extensive manipulation and reconstruction of the rail infrastructure. Although some minor surface grinding and cutting are necessary for overlay welding on the railhead, this approach ensures that the original strength of the rail base is maintained. However, previous studies [21]–[25], including the author's research [17]–[20] have demonstrated that a surface-welded rail is more susceptible to cracking and premature failure than an integral parent rail. Consequently, conducting a comprehensive investigation into the strength properties, hardness, residual stress, and distribution of inclusions, pores, and cracks in a weld-repaired rail becomes essential. Notably, no study has been published that investigates explicitly the repair of heavy-duty rails used in the standard railway network of the United States using the submerged arc welding (SAW) method as mentioned in previous research [20], various arc-based methods, such as shielded metal arc welding (SMAW), gas tungsten arc welding (GTAW), submerged arc welding (SAW), and plasma arc welding (PAW), can be employed for surface welding. Among these methods, SAW is considered the most suitable for multi-layer, high-thickness welding due to its superior quality and productivity[26], [27].

In this research, a three-dimensional coupled temperature-displacement numerical model is developed using the commercial ANSYS software. This model aims to analyze the thermo-mechanical behavior of residual thermal stresses generated during the manufacturing of the worn part of the rail using the submerged arc welding (SAW) process. This specific configuration is referred to as Case I in the study. To examine the impact of preheating on thermal stresses, two additional cases involving different preheating methods and subsequent cooling rates are investigated to determine the optimal preheating approach. In Case II, preheating is applied by placing hot plates beneath the railhead during the cooling process of the additive part to reduce residual thermal stress. In Case III, hot plates are positioned at the railhead's bottom and sides. The results obtained from all three cases are compared to evaluate the state of thermal stress at the weld/rail interface. The safety margin of thermal stresses is determined by comparing the results to the yield strength of the material.

METHODOLOGY

The rail to be repaired in this study is a worn 136RE rail commonly employed in freight and passenger railway networks across the United States. The specimen analyzed in this research was a 30-cm section of the worn rail, as depicted in Figure 1. The chemical composition of the high-carbon steel utilized in manufacturing the 136RE rail is provided in Table 1.

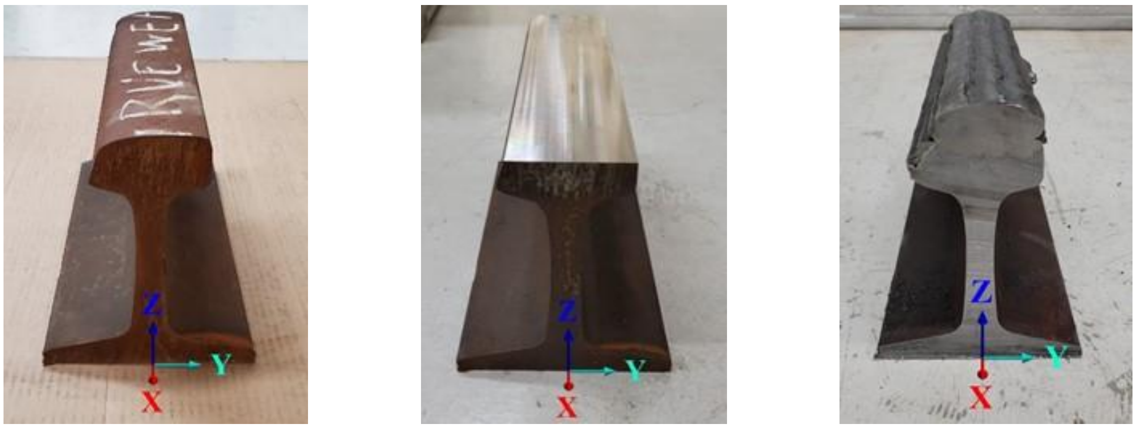

(a) (b) (c)

Figure 9.1 (a) The to-be-repaired 136RE worn rail; (b) milled rail; (c) repaired rail

Table 1 Chemical composition of the rail and the SAW wire (wt. %)

Material	Fe	C	Cr	Mn	Mo	Si	Ni	P	S
Rail	Bal.	0.80 ± 0.06	0.03 ± 0.01	0.23 ± 0.03	-	0.04 ± 0.01	0.14 ± 0.04	0.01 ± 0.005	0.01 ± 0.005
Wire	Bal.	0.12 ± 0.05	0.50 ± 0.03	2.75 ± 0.30	0.85 ± 0.05	3.30 ± 0.20	-	-	-

Table 2 Chemical composition of the neutral Lincolnweld 801 submerged arc flux (wt. %)

SiO2	CO2	CrO	MoO3	MnO	Fe2O3
10.0 ± 0.9	21.2 ± 0.8	8.9 ± 0.2	18.4 ± 0.9	14.2 ± 0.8	22.7 ± 1.0

For the SAW process, the selected depositing wire was the 1/8-inch Lincore 40-S hard-facing submerged arc wire. This specific wire was chosen due to its excellent characteristics in terms of rolling and sliding wear properties. Moreover, it is compatible with carbon steel and suitable for depositing up to 5 layers. The chemical composition of the SAW wire used is provided in Table 1. To complement the process, the neutral Lincolnweld 801 submerged arc flux was employed as the recommended and compatible flux, and its chemical composition is detailed in Table 2.

To facilitate the SAW process on a flat substrate, the surface of the worn railhead undergoes milling and flattening. Before commencing the SAW process, the milled surface is further prepared by grinding, polishing, and cleaning with acetone to eliminate loose mill scales, rust, and micro contaminants. The milled rail can be observed in Figure 1b, while Figure 1c depicts the rail after the SAW process, referred to as the surfaced rail. This emerged rail serves as the final product on which all mechanical and metallurgical assessments will be carried out.

The key distinction between conventional arc welding and SAW lies in covering flux. In SAW, the wire and the arc are effectively shielded beneath a layer of flux grains, protecting against oxidation. Another advantage of submerging the welding area within the flux stream is that it remains insulated from excessive radiation heat loss, resulting in a cleaner weld. By preventing potential heat loss mechanisms like radiation, convection, or energy scattering from wire to rail, the energy efficiency can be increased by 90% or even more. This heightened efficiency yields significant benefits, including enhanced weld reliability and a high deposition rate.

The SAW process involves the development of an arc between the filler wire and the railhead, which serves as the substrate. Simultaneously, flux grains are dispensed onto and around the arc area through a hopper. This forms a covering envelope at the arc zone, solidifying the melt pool on the railhead's surface where the arc is burned. The flux grains close to the envelope melt and solidify, forming a thin layer known as slag, which will be removed once the SAW process is completed. The current SAW process for overlay repairing the damaged railhead surface utilizes an open-circuit voltage ranging from approximately 25 to 36 V, a weld current of 150 A, a travel speed of 23 mm/s, and a wire feed rate of 21 mm/s.

Process Physical description

In the following, Nomenclature and related Subscripts describe the process given. Also, the governing equations for this process are defined as follows:

- T temperature (K)
- x, y, z coordinate
- $\vec{V}$ velocity vector (m/s)
- u, v, w velocity component (m/s)
- $\vec{g}$ gravity vector (m^2/s)
- p pressure (Pa)
- ν kinematic viscosity (m^2/s)
- β thermal expansion coefficient (K^{-1})
- α_f thermal diffusivity of air (m^2/s)
- α_s thermal diffusivity of solid body (m^2/s)
- q_{in} incident radiative heat flux (W/m^2)
- q_{out} net radiative heat flux from the surface (W/m^2)
- Ω hemispherical solid angle (sr)
- I_{in} intensity of the incoming ray (W/sr)
- $\vec{s}$ ray direction vector
- $\vec{n}$ normal vector pointing out of the domain
- ε emissivity
- ϵ strain

- σ stress (Pa)
- C fourth-order material stiffness tensor (N/m)
- H' strain-hardening rate (Pa)
- ϑ Poisson's ratio
- E elastic modulus (Pa)
- e deviatoric strain
- γ engineering strain
- t time (s)

Subscripts

- h hot body
- c cold body
- w wall
- e elastic
- p plastic
- T thermal
- eq equivalent (von-Mises)
- zz longitudinal direction of principal stress
- xx transversal direction of principal stress
- yy normal direction of principal stress

Continuity equation:

$$\vec{\nabla}.\vec{V} = 0 \tag{1}$$

Momentum equation:

$$\frac{D\vec{V}}{Dt} = -\frac{1}{\rho}\vec{\nabla}p + \nu\vec{\nabla}^2\vec{V} + \vec{g}\beta(T - T_c) \tag{2}$$

Energy equation for fluid medium:

$$\frac{DT}{Dt} = \alpha_f(\vec{\nabla}^2.T) \tag{3}$$

Energy equation for a still solid region without internal heat generation is:

$$\frac{\partial T}{\partial t} = \alpha_s(\vec{\nabla}^2.T) \tag{4}$$

The radiation intensity approaching a point on a wall surface can be integrated to yield the incident radiative heat flux:

$$q_{in} = \int_{\vec{s}.\vec{n}>0}^{q_{in}} I_{in}\vec{s}.\vec{n}d\Omega \tag{5}$$

The net radiative heat flux from the surface is then computed as:

$$q_{out} = (1 - \varepsilon_w)q_{in} + \varepsilon_w \sigma T_w^4 \tag{6}$$

Numerical Modeling

To simulate the effects of thermal stresses, a three-dimensional model of the worn rail and weld layers is created using SolidWorks 2022. The new rail profile adheres precisely to the AREMA standard profiles (136 lb/yd [136RE]), while the worn profile is obtained from the provided rail specimen. The combined new and worn rail profiles are depicted in Figure 2.

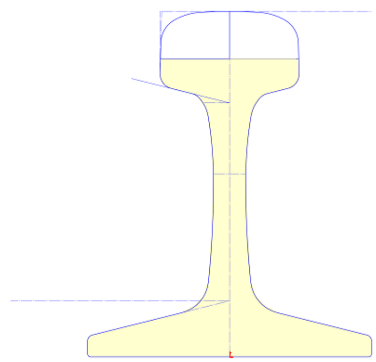

Figure 9.2 Original and worn rail profiles

A grid independence test is performed during the thermal study (finite volume) step to reduce computational time and ensure confidence in the results. As a result, a grid system consisting of 90,792 elements is employed for calculations. Among these elements, 9,792 belong to the rail part, and 81,000 are associated with the weld part. Different mesh zones generated in the solid bodies are illustrated in Figure 3.

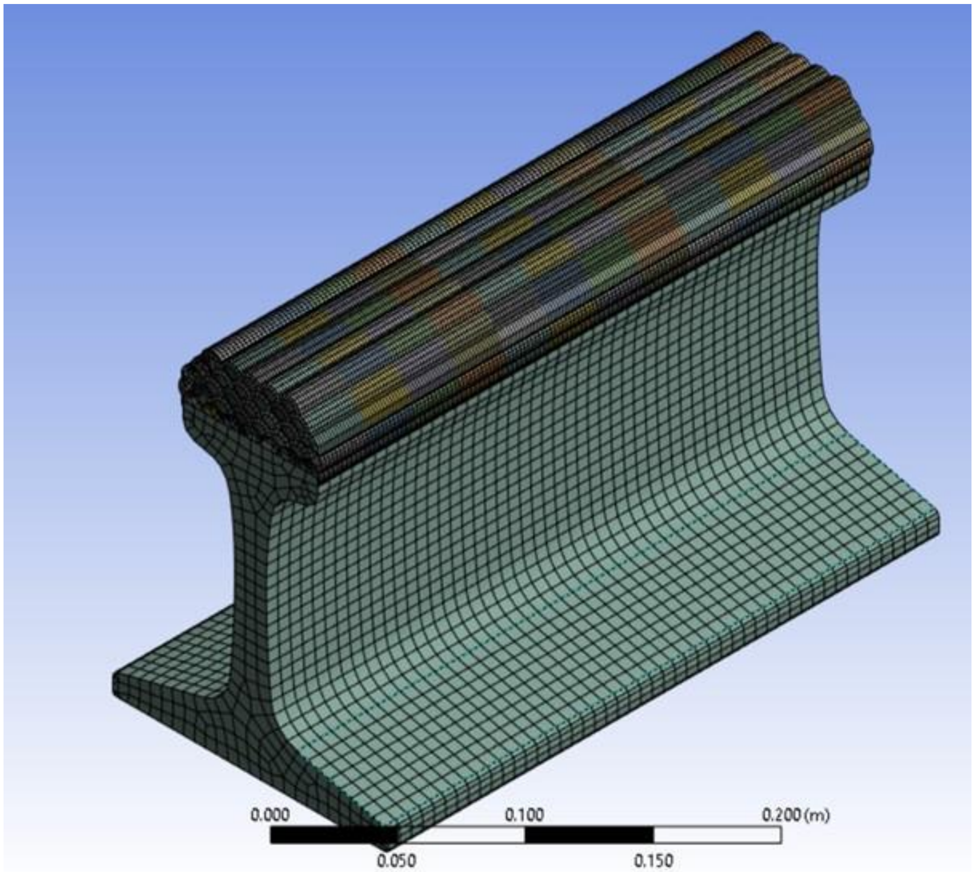

Figure 9.3 mesh zones generated in the solid bodies

The model is divided into two sections: simulation of the process in a welding pass and simulation of the process in the entire cross-section area. This division is due to the nature of the welding process. After a complete row of welding, it can be assumed the entire row has the same temperature, and it should save a huge amount of calculation without losing much accuracy, considering that the first line of welding will also be simulated. Assuming that the additive layer in the 3D printing process reaches the temperature of 1700°C and the ambient temperature (typical for SAW temperature) is 22 °C. The model is divided into two sets of elements with different material properties: the rail material and the weld material. The material properties are imported based on the data provided in Table 2.

The element birth-and-kill technique is incorporated to build up the worn part of the railhead in the FE. Each element was considered with a length of 25mm, so there are 12 elements in each pass. According to welding speed, the time steps of this method are applied to the model. Considering this method, the welding process can be simulated as an internal heat generation with 3.8e009 W/m3. The generated heat can be extracted from the current and voltage of the process by an adjustment to ensure that the melting pool's temperature will be provided (T=1700°C). The shape of the elements was estimated according to the actual weld profile in the real sample.

The thermal history field and subsequent residual stresses are analyzed through sequential thermo-mechanical analyses utilizing the commercial finite element code ANSYS 2023 R1. The thermal heat transfer analysis replicates the cooling process using the transient thermal method, and the results of this analysis are used as initial conditions for the subsequent finite element analysis.
Model Results

Using numerical modeling, comprehensive information can be obtained regarding temperature distribution. As before mentioned, to reduce the computational calculation this model is divided into two main sections. In the first section, the model properties are validated by examining one welding row. In this regard, the result is shown in the figure 5. Figure 4 also shows the procedure modeling. This model is a result of finite element try and error to find the optimum element size and heat generation properties as the controllable inputs.

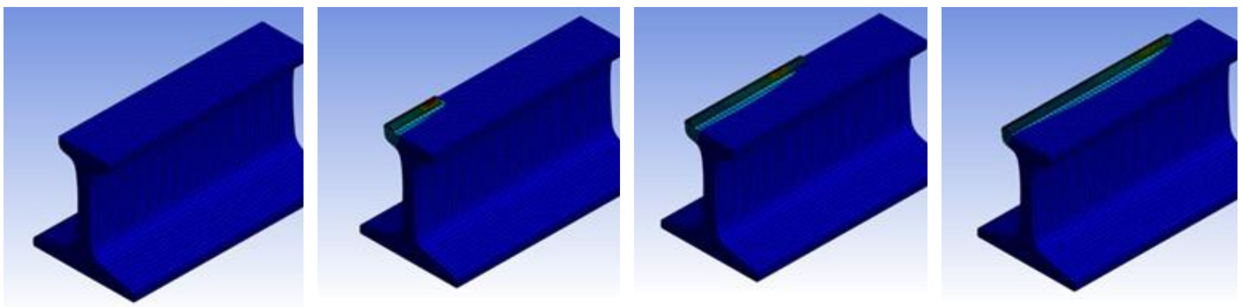

Figure 9.4 Graphical show of the model's procedure (step1)

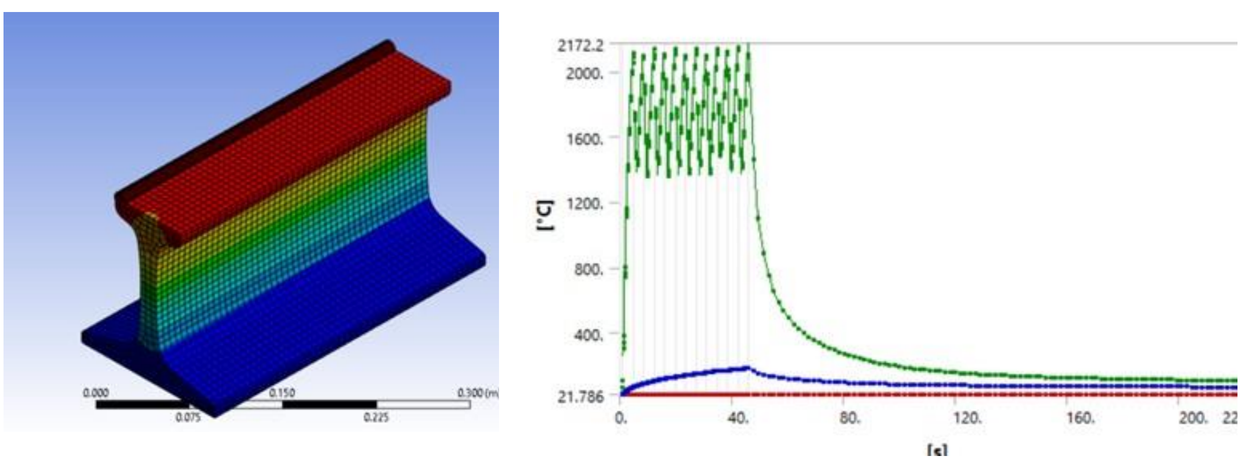

Figure 9.5 Graphical and numerical temperature distribution resulted from the model

The welding process is modeled on a 2D scale in the second step. In this section, only the first element got involved in the model. The first step's result shows that this assumption does not affect the entire process. Figure 5 illustrates the profile temperature result and historical temperature profile in the sample. This thermal history shows that in the Fe-Cr phase (Figure 6) what is the mechanical properties of the simulated maple. The dotted line in this diagram according to the table 3.

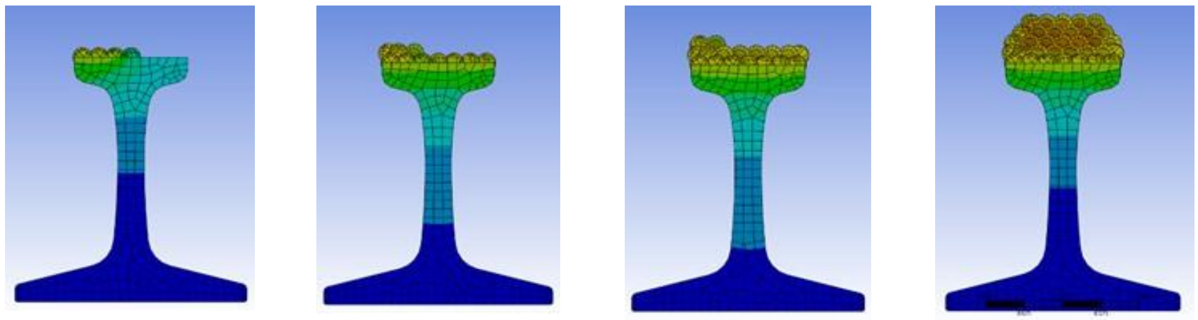

Figure 9.6 Graphical show of the model's procedure (step 2)

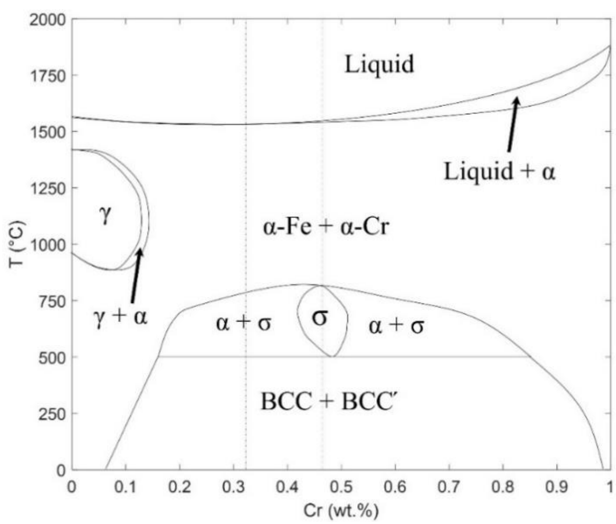

Figure 9.7 Fe-Cr phase diagram for the Lincore 40-S hard-facing wire used in the SAW process

Table 3 Chemical composition (wt. %) of different areas of the repaired rail (Areas are addressed graphically in Fig. 4.)

Area	Fe	C	Cr	Mn	Mo	Si
Layer 4	Bal.	0.067 ± 0.007	0.32 ± 0.05	1.25 ± 0.20	0.82 ± 0.03	3.42 ± 0.40
Layer 3	Bal.	0.028 ± 0.007	0.39 ± 0.05	1.93 ± 0.20	0.80 ± 0.03	3.26 ± 0.40
Layer 2	Bal.	0.016 ± 0.007	0.41 ± 0.05	2.55 ± 0.20	0.73 ± 0.03	3.12 ± 0.40

Layer 1	Bal.	0.017 ± 0.007	0.47 ± 0.05	2.19 ± 0.20	0.73 ± 0.03	2.94 ± 0.40
HAZ	Bal.	0.23 ± 0.06	0.12 ± 0.01	1.01 ± 0.20	0.03 ± 0.01	0.53 ± 0.40
Rail	Bal.	0.80 ± 0.06	0.03 ± 0.01	0.23 ± 0.03	-	0.04 ± 0.01

The Fe-Cr phase diagram shows that the Lincore 40-S weld wire, containing approximately 0.5 wt.% chromium (as stated in Table 1), consists of a mixture of BCC phases with Fe-rich (BCC) and Cr-rich (BCC') alloy compounds at room temperature.. At 0 ≤ Cr-wt.% < 0.12, the austenite with the lightest appearance in HCl-etched carbon steel nucleates. Then, at Cr-wt.% ≥ 0.12, a combined α-Fe + α-Cr phase forms, which starts with the dominancy of the light-etched α-Fe at Cr-wt.% = 12 and smoothly transforms to a dark-etched, α-Cr-dominant compound as the Cr-wt.% leans towards 1.

Table 2 shows a declined flow of Cr-wt.% from Layer 1 to Layer 4. The liquidus weld drops at 1600 – 1700 °C, and the preheated railhead surface has a temperature of 200 – 300 °C, so the weld materials start to experience an initially fast cooling procedure down to 500 – 700 °C during the first layer. At the beginning of the second layer, Layer 1 is reheated and has a long exposure at a higher temperature range, 700 – 1000 °C. Layer 2, with a higher initial substrate temperature (500 – 700 °C), remains at elevated temperatures around 700-1000 °C until the third layer starts. This trend proves that the top layers are exposed to higher temperature ranges, i.e., higher than 500 – 800 °C. Prolonged exposures to temperatures in the range of 500 – 800 °C give enough time for the α→σ transition—besides, a higher wt.% of Cr results in higher precipitated σ but lower Cr-wt.% gives a lower fraction of the brittle σ phase in the final microstructure. This explains why the semi-dark σ fraction decreases from Layer 1 to 4. By moving to the upper layers, the number of reheating opportunities (and the length of the 500 – 800 °C exposure time) decreases, hence the chance of α→σ decreases. Another observable fact is that, as the Cr-wt.% decreases from Layer 1 to Layer 4 (Table 2), the volume fraction of the Cr-rich α, i.e., α-Cr, falls, and that of the Fe-rich α, i.e., α-Fe, increases. Therefore, layer 1 contains the highest, and layer 4 (Fig. 5c) has the lowest amount of this dark α-Cr volume fraction among layers. In addition, the wt.% of the ferrite stabilizers (Mo and Si) has an increasing trend from Layer 1 to Layer 4 (Table 2), leading to the increment of the ferrite phase and increasing the light-etched α-Fe area in the upper layers.

This diagram is modeled in the computational model based on the following diagrams. These diagrams are the linear forms of the phase diagram.

Table 4 Temperature- and Microstructure-Dependent Material Properties of Substrate (Rail) and Deposition Materials; Used in Fe Modeling of Additive Manufacturing (Lpd) Process

Material		T (°C)	E (GPa)	**ν**	**α** (10-5/°C)	c (J/kg°C)	K (W/m°C)
304L Stainless Steel (Deposition Material)	δ	25	-	-	-	-	-
		600	134	0.34	1.73	745	18.9
		1000	19	0.41	1.82	984	15.5
		1500	19	0.41	1.82	971	13.2

	γ	25	200	0.29	1.73	510	15.5
		600	141	0.37	1.87	687	22.4
		1000	19	0.45	1.97	953	28.7
		1500	-	-	-	-	-
C-Mn (880 grade) steel (Substrate Material)	$\alpha + Fe_3C$	25	203	0.26	1.2	434	60.5
		600	110	0.33	1.4	638	41.6
		1000	-	-	-	-	-
		1500	-	-	-	-	-
	γ	25	-	-	-	-	-
		600	-	-	-	-	-
		1000	19	0.4	1.47	886	12.6
		1500	19	0.4	1.47	886	12.6

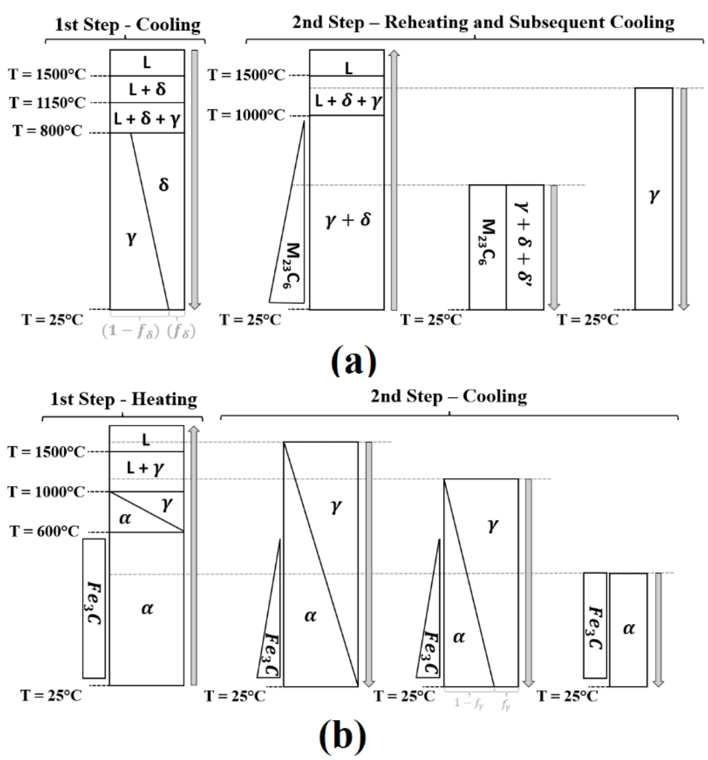

Figure 9.8 A Schematic Diagram of the Microstructure Evolution Pattern Defined in Fe Modeling During the Additive Manufacturing (Lpd) Process, and its Cyclic Heating and Cooling for (A) Deposition Materials (304l Stainless Steel), and (B) Substrate (Rail). Δ: Δ Ferrite; Α: Α Ferrite; and Γ: Austenite

Experimental validificatiuon

Hardness test

The Rockwell C hardness test is the best scale for high/mild carbon steels, conforming to ASTM E18 [28]. The Rockwell C scale's applied major and minor loads are 150 kgf and 10 kgf, respectively. A LECO hardness tester is used for this purpose. Fig. 2e shows the assigned test plan on the transverse section, using the slices cut from the repaired rail shown in Fig. 2b based on the test protocol provided by the American Railway Engineering and Maintenance-of-way Association (AREMA) [29].

Tensile test

The prepared tensile samples are illustrated in Fig. 2f and Fig. 2g. Four specimens are extracted from different regions of the base railhead and weld. The test method follows ASTM E8M[30], and the load requirement is assigned as per AREMA [29]. The test specimens are machined and dimensioned based on ASTM E8M. The standard test jig, recommended by ASTM E8M, is bundled with a hydraulic compression system as the major component of the test setup. A constant crosshead velocity of 2.5 mm/min is used for the tensile test.

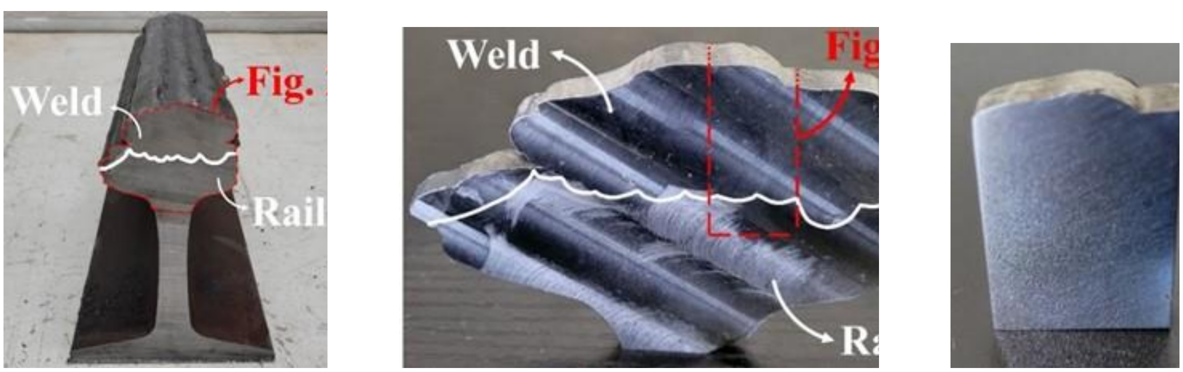

(a) (b) (c)

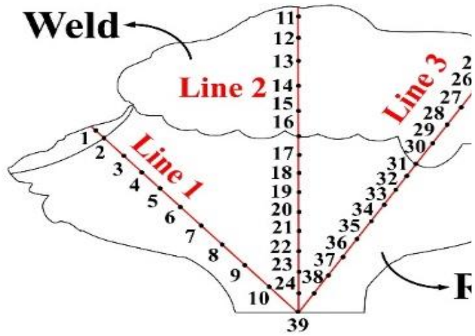

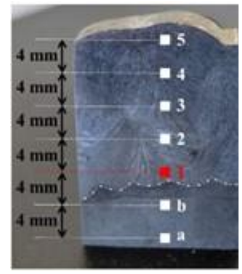

(g) (e) (d)

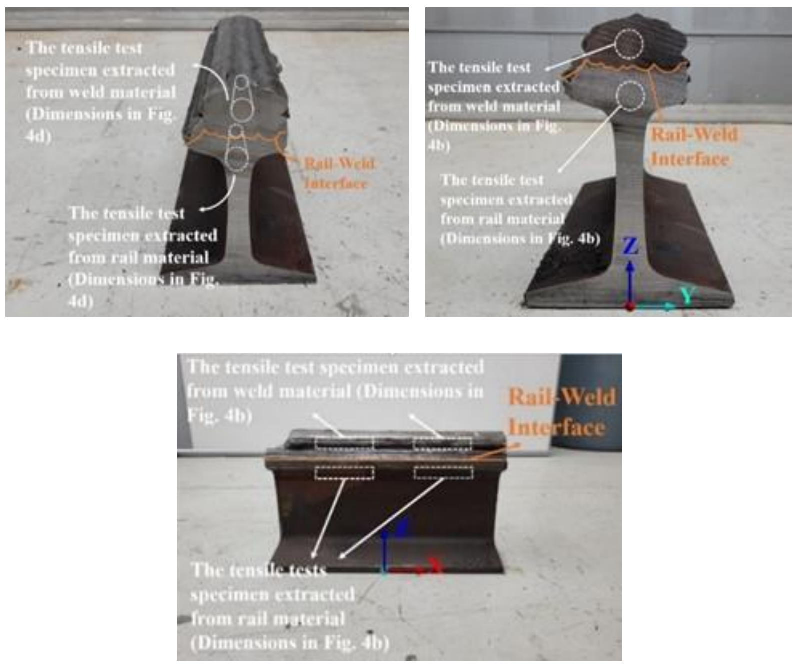

(f)

Figure 8 (a) the Repaired Rail; (b) the extracted slice from the repaired rail; (c) the extracted, polished XRD specimen from the slice; (d) the etched XRD specimen; (e) the hardness test plan; (f) Locations where the tensile specimens are extracted from the weld and the rail materials; (b) dimensions of a typical tensile test specimen (all dimensions are in millimeters)

Conclusion

In this chapter, a 3D model was modified and a coupled finite volume-finite element method was utilized to investigate the thermo-mechanical effects of high-temperature additive materials on the rail during the SAW process for repair purposes on worn rails. Three cases were examined to analyze the impact of preheating on the residual thermal stress induced at the rail/additive interface. The key findings can be summarized as follows:

1- In phase one, the stress distribution revealed that in each pass of welding, the temperature result leans to a temperature, which in the second phase is used in the rest of the conclusion.

2- To mitigate the rapid cooling rate, Case II was introduced, where two hot plates were placed at the bottom of the railhead to maintain elevated temperatures at the rail and rail/additive interface for a longer duration. This approach led to a reduction of approximately 40% in the final induced thermal stress. However, both Case I and Case II exhibited a sudden increase in stress at the edges of the transversal line of the rail/weld interface. This phenomenon occurred because the edge points experienced the fastest cooling rate due to direct exposure to airflow and the ambient wall. Consequently, these points rapidly lost heat through various heat transfer mechanisms, including conduction, convection, and radiation.
3- To address this issue, Case III was introduced, where two additional hot plates were positioned at the sides of the railhead. By doing so, these hot plates shielded the edges of the interface from direct exposure to the ambient environment. It was observed that this approach effectively mitigated the residual stresses at the edges, eliminating the sudden stress increases observed in the previous cases.

Overall, the study demonstrated the influence of numerical methods in simulation of welding process on the distribution of residual thermal stress at the rail/weld interface. The findings highlighted the importance of controlling the cooling rate and providing thermal insulation to minimize thermal stresses and ensure the integrity of the printed components.

References for chapter 10

[1] S. R. Lewis, R. Lewis, and D. I. Fletcher, "Assessment of laser cladding as an option for repairing/enhancing rails," Wear, vol. 330–331, pp. 581–591, May 2015, doi: 10.1016/j.wear.2015.02.027.
[2] W. J. Wang, J. Hu, J. Guo, Q. Y. Liu, and M. H. Zhu, "Effect of laser cladding on wear and damage behaviors of heavy-haul wheel/rail materials," Wear, vol. 311, no. 1–2, pp. 130–136, Mar. 2014, doi: 10.1016/j.wear.2014.01.011.
[3] B. Paul, "A Review of Rail-Wheel Contact Stress Problems."
[4] P. A. Montenegro and R. Calçada, "Wheel–rail contact model for railway vehicle–structure interaction applications: development and validation," Railway Engineering Science, 2023, doi: 10.1007/s40534-023-00306-4.
[5] B. Liu and S. Bruni, "Analysis of Wheel-Roller Contact and Comparison with the Wheel-Rail Case," Urban Rail Transit, vol. 1, no. 4, pp. 215–226, Dec. 2015, doi: 10.1007/s40864-015-0028-3.
[6] T. Telliskivi and U. Olofsson, "Contact mechanics analysis of measured wheel-rail profiles using the finite element method," in Proceedings of the Institution of Mechanical Engineers, Part F: Journal of Rail and Rapid Transit, 2001, pp. 65–72. doi: 10.1243/0954409011531404.
[7] W. Yan and F. D. Fischer, "Applicability of the Hertz contact theory to rail-wheel contact problems."
[8] W. Zhai, J. Gao, P. Liu, and K. Wang, "Reducing rail side wear on heavy-haul railway curves based on wheel-rail dynamic interaction," in Vehicle System Dynamics, Taylor and Francis

Ltd., May 2014, pp. 440–454. doi: 10.1080/00423114.2014.906633.
[9] "The_Art_and_Science_of_Rail_Grinding".
[10] A. Kapoor, J. H. Beynon, D. I. Fletcher, and M. Loo-Morrey, "Computer simulation of strain accumulation and hardening for pearlitic rail steel undergoing repeated contact," in Journal of Strain Analysis for Engineering Design, Jul. 2004, pp. 383–396. doi: 10.1243/0309324041223935.
[11] "d940f7aa37ad31fbbe878e79fd401199".
[12] A. Mazzù, C. Petrogalli, and M. Faccoli, "An integrated model for competitive damage mechanisms assessment in railway wheel steels," Wear, vol. 322–323, pp. 181–191, Jan. 2015, doi: 10.1016/j.wear.2014.11.013.
[13] M. N. SaifulAkmal and M. N. Wahab, "Characterization of UIC-54 Rail Head Surface Welded by Hardfacing Using Flux-Cored Steel Wire," in Lecture Notes in Mechanical Engineering, Springer Science and Business Media Deutschland GmbH, 2021, pp. 763–775. doi: 10.1007/978-981-15-9505-9_68.
[14] D. De Becker, J. Dobrzanski, M. Goh, and L. Justham, "Towards the development of a deposition technology for an automated rail repair system," May 2020, pp. 100–102. doi: 10.31256/Vz2Jt4I.
[15] E. Kabo, A. Ekberg, and M. Maglio, "Rolling contact fatigue assessment of repair rail welds," Wear, vol. 436–437, Oct. 2019, doi: 10.1016/j.wear.2019.203030.
[16] L. Xin, V. Markine, and I. Shevtsov, "Analysis of the effect of repair welding/grinding on the performance of railway crossings using field measurements and finite element modeling," Proc Inst Mech Eng F J Rail Rapid Transit, vol. 232, no. 3, pp. 798–815, Mar. 2018, doi: 10.1177/0954409717693960.
[17] E. Mortazavian, Z. Wang, and H. Teng, "Effect of heat treatment on microstructure and hardness of a worn rail repaired using laser powder deposition," International Journal of Transportation Science and Technology, vol. 11, no. 2, pp. 406–422, Jun. 2022, doi: 10.1016/j.ijtst.2021.05.004.
[18] E. Mortazavian, Z. Wang, and H. Teng, "Finite Element Investigation of Thermal-kinetic-mechanical Evolutions during Laser Powder Deposition as an Innovative Technique for Rail Repair," International Journal of Advanced Manufacturing Technology, vol. 118, no. 1–2, pp. 319–342, Jan. 2022, doi: 10.1007/s00170-021-07873-y.
[19] E. Mortazavian, Z. Wang, and H. Teng, "Measurement of Residual Stresses in Laser 3d Printed Train Rail Using X-Ray Diffraction Technique," 2021.
[20] E. Mortazavian, Z. Wang, and H. Teng, "Repair of light rail track through restoration of the worn part of the railhead using submerged arc welding process," International Journal of Advanced Manufacturing Technology, vol. 107, no. 7–8, pp. 3315–3332, Apr. 2020, doi: 10.1007/s00170-020-05208-x.
[21] B. L. Josefson and J. W. Ringsberg, "Assessment of uncertainties in life prediction of fatigue crack initiation and propagation in welded rails," Int J Fatigue, vol. 31, no. 8–9, pp. 1413–1421, Aug. 2009, doi: 10.1016/j.ijfatigue.2009.03.024.
[22] A. Masoudi, M. Davarpanah Jazi, M. Mohrekesh, and R. Masoudi Nejad, "An investigation of rail failure due to wear using statistical pattern recognition techniques," Eng Fail Anal, vol. 134, Apr. 2022, doi: 10.1016/j.engfailanal.2022.106084.
[23] H. Desimone and S. Beretta, "Mechanisms of mixed mode fatigue crack propagation at rail butt-welds," Int J Fatigue, vol. 28, no. 5–6, pp. 635–642, May 2006, doi: 10.1016/j.ijfatigue.2005.07.044.

[24] A. Skyttebol, B. L. Josefson, and J. W. Ringsberg, “Fatigue crack growth in a welded rail under the influence of residual stresses,” Eng Fract Mech, vol. 72, no. 2, pp. 271–285, Jan. 2005, doi: 10.1016/j.engfracmech.2004.04.009.
[25] R. Masoudi Nejad, Z. Liu, W. Ma, and F. Berto, “Fatigue reliability assessment of a pearlitic Grade 900A rail steel subjected to multiple cracks,” Eng Fail Anal, vol. 128, Oct. 2021, doi: 10.1016/j.engfailanal.2021.105625.
[26] “Submerged_Arc_Welding”.
[27] S. Bharathi, A. Arul, M. Moshi, S. R. Sundara Bharathi, R. Rajeshkumar, and R. Kumar, “Factors Influencing Submerged Arc Welding On Stainless Steel-A Review,” vol. 11, no. 2, 2016, [Online]. Available: www.arpnjournals.com

10. Chapter 10 ADDITIONAL MECHANICAL AND METALLURGICAL ASSESSMENT OF SUBMERGED ARC SURFACED RAIL

The railhead surface is constantly subject to several destructive interactions, such as wheel-rail rolling contact fatigue [1], frictional burns due to wheel slippage [2], and ballast flying damage [3]. Therefore, a practical repair method may be applied to restore the damaged surface of the railhead to ensure the comfort and security of riding the trains. Minor surface damages on a railhead can be rehabilitated using surface grinding, an easy railway maintenance technique appropriate for immediate and extensive application [4]. Although this method can effectively eliminate the point defects, the grinding length should be long enough to compensate for the vertical winding impact. Hence, grinding is not a sensible repair in case of moderate railhead surface damage. Instead, removing the damaged area and rebuilding the lost material using an additive manufacturing technique is practical. This overlay rail repair idea originated from a patent by Kral et al. in 2004 [5]; ever since, several have been devoted to investigating various build-up methods for repairing conventional rails in different countries.

Overlay arc welding of UIC60 rails is assessed by a couple of research groups in Korea [6-8]. Feng et al. [9] analyzed the pros and cons of online welding and post-heat treatment of standard rails in China. Another research study in China focused on surface repairing U75V rails using laser-directed energy deposition [10]. In Thailand, Suwanpinij et al. [11] demonstrated improved surface properties of surface-welded R260 and R350HT rails compared to the base rail material. Srikarun [12] also investigated the abrasive wear performance of R260 rails that are repaired by shield metal arc welding (SMAW). Repairing of damaged surface of UIC-54 rails used in the Malaysia railway network using SMAW is investigated by Saiful Akmal and Wahab [13]. A research group thoroughly explores laser cladding of hypereutectoid Australian rails and its upgrading and downgrading effects at Monash University [14]. De Becker et al. [15] are developing a mobile system for automated on-site repair of the damaged railway network in the United Kingdom. A numerical model investigating the rolling contact fatigue performance and material defects of a weld-repaired rail is developed by Kabo et al. [16] in Sweden. Another valuable numerical study was conducted by Xin et al. [17] in the Netherlands, in which repair welding and grinding of standard European rails are surveyed using finite element modeling.

Regarding the investigation of the standard rails used in the United States railway system, the current team is the only research group thus far that has focused on repairing them using overlay weld techniques. One line of investigation was solely devoted to laser cladding of damaged rail surfaces, both the light transit rails [18,19] and heavy freight/passenger rails [20] in the United States. A separate line of research assessed the submerged arc welding (SAW) technique for repairing light rails [21]. The current paper is the first study focused on evaluating the mechanical and metallurgical properties of a standard U.S. heavy rail repaired using SAW.

Each type of rail repair method, i.e., a laser-based method like laser cladding or an arc-based method like SAW, has its benefits and drawbacks. Therefore, without in-depth investigation, a specific method cannot be immediately determined as the best option in all mechanical and metallurgical aspects. Instead, the most proper technique should be determined based on factors such as rail type, repair quality, cost, and railway network occupation time.
Surface repairing a damaged railhead has significant advantages over the conventional

replacement approach, especially since it is much easier to implement and does not require manipulating and rebuilding the rail infrastructure. Although some minor surface grinding and cutting are required for overlay welding on the railhead surface, it allows the rail base to maintain its original strength. Nevertheless, it is shown in quite a lot of former studies [22-26], including authors' studies [18-21], that a surface welded rail is much more vulnerable to cracking and premature failure than an integral parent rail. Therefore, it is necessary to thoroughly investigate the strength properties, Hardness, residual stress, and distribution of inclusions, pores, and cracks in a weld-repaired rail. However, no study has been published investigating the SAW-repairing of heavy-duty rails used in the standard railway network of the U.S. As was mentioned in the former research as well [21], there are several potential arc-based methods for surface welding, such as SMAW, gas tungsten arc welding (GTAW), submerged arc welding (SAW), and plasma arc welding (PAW). However, SAW is the most proper method for multi-layer, high-thickness welding while delivering the highest quality and productivity [27,28].

Through some experiments, this study investigates the mechanical and metallurgical properties of a SAW-repaired standard U.S. heavy rail. These tests include micro-hardness Measurement, X-ray diffraction (XRD) for residual stress measurement, microstructural evaluation using an optical microscope (O.M.) and scanning electron microscope (SEM), and tensile test. First, the material properties of the rail base, weld wire, and flux particles are presented. Second, a summarized description of the SAW process and incorporated processing parameters are given. Sample preparation strategies for each experiment are then thoroughly described. Finally, the results are presented and discussed, and some solutions to modify the existing properties and mitigate the residual stresses are suggested for future studies.

2. Experimental

2.1. Materials

The to-be-repaired rail is a worn 136RE rail utilized in most freight/passenger railway networks across the United States. The studied specimen is a 30-cm cut of the worn rail, as shown in Fig. 1a. Chemical composition of the high-carbon 136RE rail steel is listed in Table 1.

The depositing wire for the SAW process is chosen to be a 1/8-in Lincore 40-S hard-facing submerged arc wire because of its distinguished rolling and sliding wear properties. In addition, this wire is specifically compatible with carbon steel and appropriate for depositing up to 5 layers. Table 1 gives the chemical composition of the utilized SAW wire. The neutral Lincolnweld 801 submerged arc flux is used as the recommended and compatible flux, of which the chemical composition is demonstrated in Table 2.

The surface of the worn railhead is milled and flattened for a better SAW process on a flat substrate. The milled surface is also ground, polished, and cleaned with acetone to remove all loose mill scales, rust, and micro contaminants before starting the SAW process. The milled rail is shown in Fig. 1b. The SAW-surfaced rail, i.e., surfaced rail, is shown in Fig. 1c. This is the final product on which all the mechanical and metallurgical assessments will be conducted.

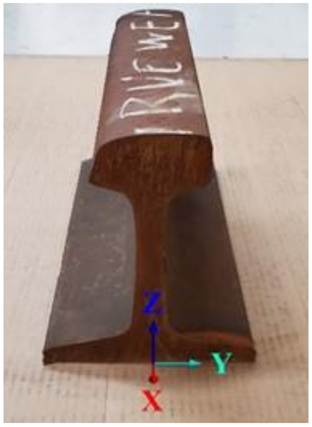

(a)

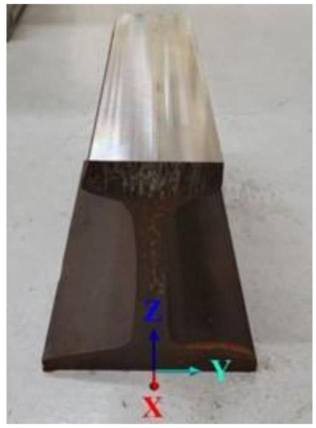

(b)

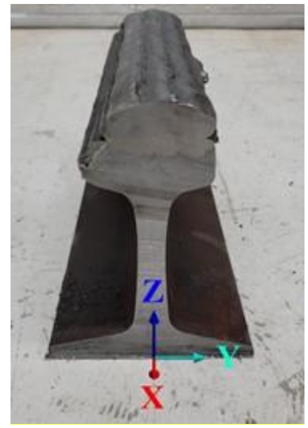

(c)

Figure 10.1 (a) The to-be-repaired 136RE worn rail, (b) milled rail, and (c) repaired rail

Table 1 Chemical composition of the rail and the SAW wire (wt.%)

Material	Fe	C	Cr	Mn	Mo	Si	Ni	P	S
Rail	Bal.	0.80 ± 0.06	0.03 ± 0.01	0.23 ± 0.03	-	0.04 ± 0.01	0.14 ± 0.04	0.01 ± 0.005	0.01 ± 0.005
Wire	Bal.	0.12 ± 0.05	0.50 ± 0.03	2.75 ± 0.30	0.85 ± 0.05	3.30 ± 0.20	-	-	-

Table 2 Chemical composition of the neutral Lincolnweld 801 submerged arc flux (wt.%)

SiO_2	CO_2	CrO	MoO_3	MnO	Fe_2O_3
10.0 ± 0.9	21.2 ± 0.8	8.9 ± 0.2	18.4 ± 0.9	14.2 ± 0.8	22.7 ± 1.0

2.2. Submerged Arc Welding (SAW)

The featured difference between regular arc welding and SAW is the covering flux. The wire and the arc are technically buried under flux grains to stay immune from oxidation. Another advantage of submerging the welding spot into the flux stream is that it stays free of any extreme radiation heat loss, which keeps it a very clean weld. Blocking potential heat loss mechanisms, such as radiation, convection, or scattering the transferring energy from wire to the rail, helps increase energy efficiency by close to 90% or even higher. The valuable outcomes of such a high efficiency are great weld reliability and a high deposition rate.

An arc is developed between the wire as the filler material in the SAW process. This arc applies from the wire to the railhead as the substrate. At the same time, flux grains are flown on and around the arc area through a hopper. Therefore, a covering envelope is developed at the arc zone to solidify the melt pool where the arc is burnt on the railhead surface. The flux grains near the envelope melt, firm, and establish a thin coat on the weld, which is called slag and will be removed after finishing the SAW process. An open-circuit voltage of 25~36 V, 150 A of weld current, 23 mm/s of travel speed, and 21 mm/s of wire feed rate are utilized for the current SAW process, i.e., overlay repairing of damaged railhead surface. Further details and explanations about the SAW process in tandem with a schematic figure can be found in the former study [21].

2.3. Sample preparation and test method

2.3.1. XRD residual stress measurement

The experiments' first step starts with preparing samples for XRD stress measurement, the stress distribution all over the weld material, and part of the rail material. Slices used to extract samples are cut, as shown in Fig. 2b. A rectangular specimen is extracted from the piece to contain all the weld layers, the rail-weld interface, and the rail. Fig. 2c shows the extracted XRD specimen.
The XRD stress measurement on the specimen surface is performed using a Bruker D8 Discovery X-ray diffractometer that contains a CuKα radiation source and a constant 1.5406 Å wavelength. The voltage and current of the X-ray tube are 40 kV and 40 mA, respectively. The measurement area is controlled through a 1-mm pinhole collimator. Based on the study by Ghasri-Khouzani et al. [31], an X-ray beam originated from a CuKα source and aimed at a non-austenitic steel surface has an average penetration depth of 5 μm. Accordingly, to mitigate the surface roughness and to ensure that there are no surface spikes taller than 5 μm to interrupt the X-ray beams, pasted diamond suspensions on SiC papers are used to polish the specimen down to 1 μm. The extracted, polished specimen is visible in Fig. 2c. A thickness of 750 μm is removed from the sample surface due to polishing.

The sample is etched to remove the relaxed residual stresses on the polished sample surface due to cutting and polishing. The incorporated etchant is an HCL-based solution made from HCL (30 ml), H_2O_2 (1.5 ml), and H_2O (10 ml). The etched sample is presented in Fig. 2d. Each course of 30-second etching removes around 50 μm of the sample thickness. Then, the etching course is repeated until the XRD-measured stress on the surface is stabilized and externally-induced residual stresses are entirely removed. The related graphs of this step of testing validation will be presented and discussed in the Results section. The locations where residual stress is measured using XRD are shown in Fig. 2d as numbered white spots on the etched sample, except for spot 1, shown in red. The stress at spot 1 is frequently measured at each sample preparation step, i.e., before and after polishing and after each etching course. This Measurement ensures that the existing error factors are eliminated, i.e., surface roughness and externally-induced residual stresses. Once the sample is etched enough that the measured stress at spot 1 is stabilized, stress at the other spots is measured.

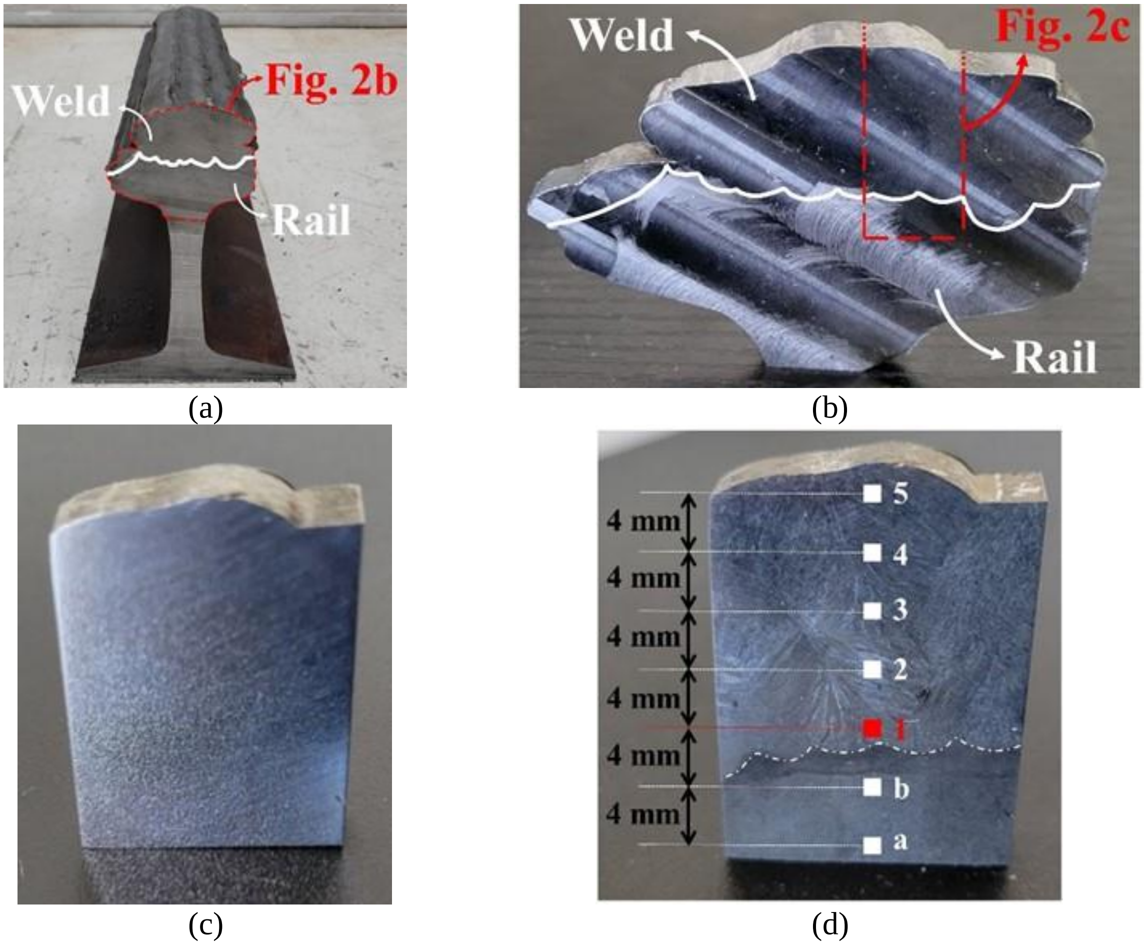

Figure 10.2(a) Repaired Rail, (b) The extracted slice from the repaired rail, (c) the extracted, polished XRD specimen from the slice, and (d) the etched XRD specimen

As another contribution to validating the XRD test results, surface roughness is measured at each step of sample preparation to ensure that it does not exceed 1 μm after polishing and etching. a Dektak 6M stylus profiler is used to do so. The profiler has a diamond-tip stylus with a diameter of 25 μm. At each run, the stylus applies a 10 mg contact load on the surface and scans a 2-mm length for 13 seconds, which gives 3,900 data points. The roughness of the gained profile data has a horizontal resolution of 1×10^{-5} μm and a vertical resolution of 1×10^{-5} μm. The existing noises are removed from the raw data using a cubic spline filter to reach the roughness profile accuracy. The study in [32] gives more details about this noise-removal method.

2.3.2. SEM/OM analysis

The etched sample shown in Fig. 2d and the destructed samples under tensile tests, which will be described in later sections, are used for O.M. and SEM metallographic examination.
O.M. morphology is carried out using a Leica DM750M optical microscope, and SEM

investigation is performed through a JEOL JSM-5610 scanning electron microscope. Chemical composition variations between different weld layers, rail, and heat-affected zone (HAZ) are tracked with an Oxford ISIS electron-dispersive X-ray spectroscopy (EDS) detector coupled with the SEM device.

2.3.3. Hardness test

The third step is to measure the Hardness all over the repaired railhead, including weld material and base material, using the slices cut from the repaired rail shown in Fig. 2b and Fig. 3a.

Rockwell C hardness test is the best scale for high/mild carbon steels, conforming to ASTM E18 [29]. The applied major and minor loads for the Rockwell C scale are 150 kgf and 10 kgf, respectively. A LECO hardness tester is used for this purpose in this regard. Fig. 3b shows the assigned test plan on the transverse section of the slice. The numbered black spots show the measurement locations. The red lines and black measuring spots in Fig. 3b follow the standard test protocol provided by American Railway Engineering and Maintenance-of-way Association (AREMA) [30].

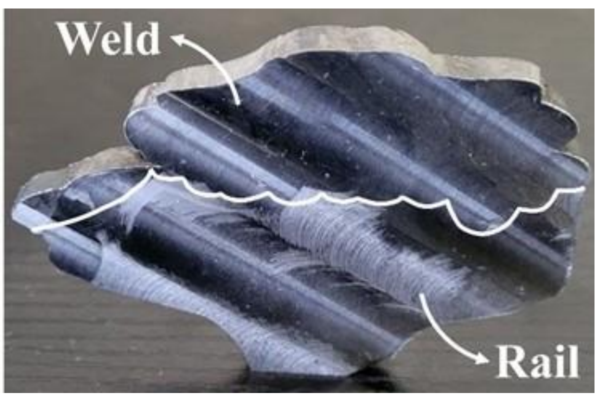

(a)

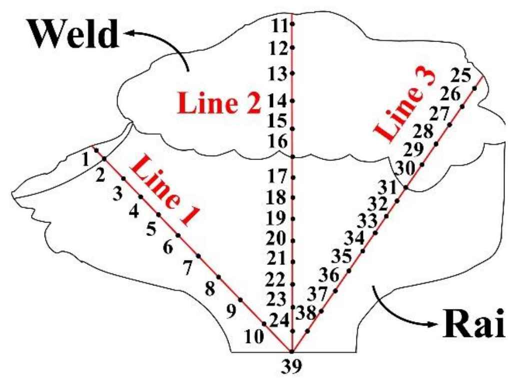

(b)

Figure 10.3 (a) Extracted slice as the hardness test specimen and (b) the hardness test plan

2.3.4. Tensile test

The prepared tensile samples are illustrated in Fig. 4. Four specimens are extracted from different regions of the base railhead and weld. The test method follows ASTM E8M [33], though the load requirement is assigned as per AREMA [30]. The test specimens are machined and dimensioned based on ASTM E8M. The standard test jig recommended by ASTM E190 [34] and bundled with a hydraulic compression system as the major components of the test setup. In addition, 2.5 mm/min of constant crosshead velocity is used for the tensile test.

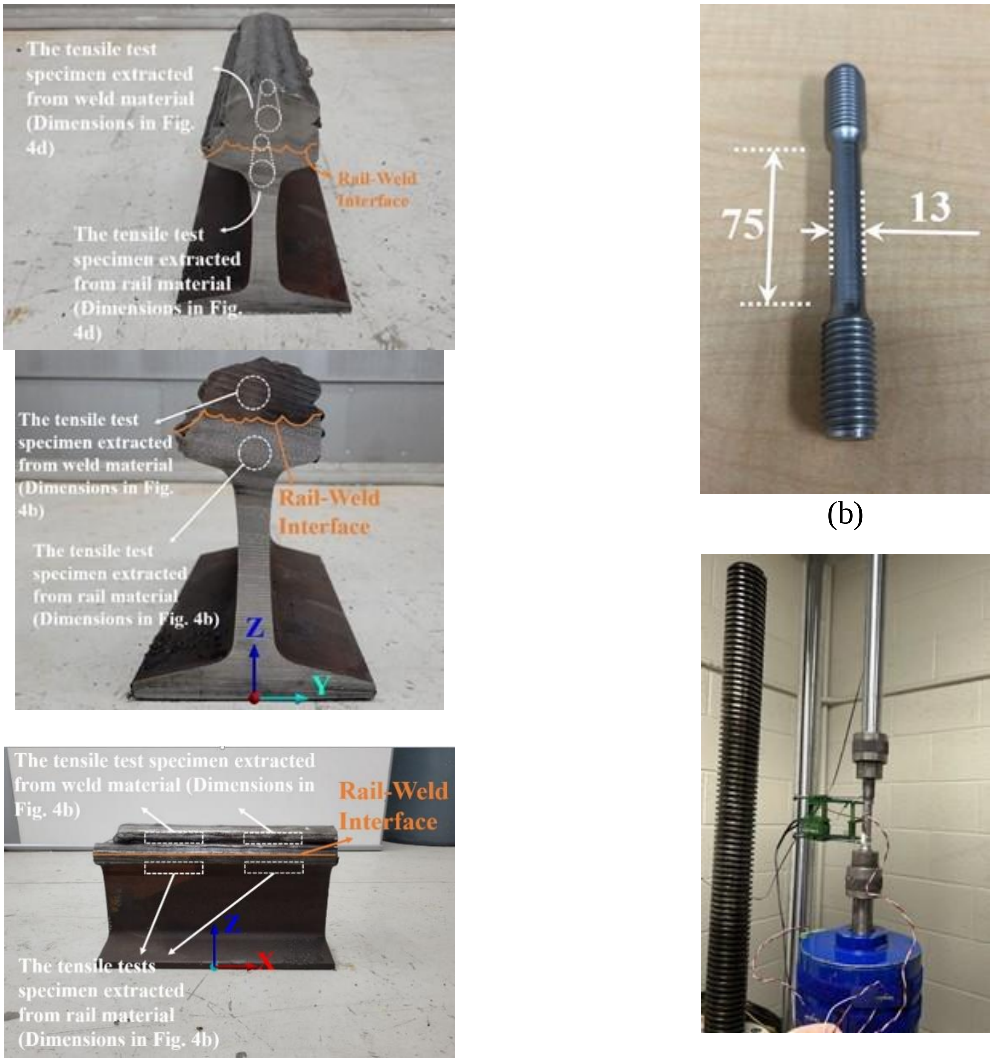

(a) (b) (c)

Figure 10.4(a) Locations of extracting the tensile specimens from weld and rail materials, (b) typical tensile test specimen dimensions (all dimensions are in millimeters), (c) the tensile test specimen fixed in the machine test jigs.

3. Results and Discussion

3.1. XRD residual stress measurement

3.1.1. Surface Roughness

A stylus profiler measures the XRD specimen's surface roughness before polishing in the as-built condition, after polishing, and after the first step of etching to ensure that the height of the surface spikes does not exceed 5 µm (see sec. 2.3.1).

The measured surface profiles are given in Fig. 5. A horizontal dashed line represents the graphs' median plane at the zero-µm level. A considerable roughness in the order of 25-50 µm is seen for the As-built specimen in Fig. 5. Spikes are located where a positive roughness (higher than the median plane) is captured, and pits exist where there is a negative roughness (lower than the median plane). This order of +/- 50 µm suggests that the X-ray beams with only a 5 µm penetration depth will be interrupted by the surface spikes and pits, so any stress measurement will not be reliable.

The surface roughness of the Polished specimen in Fig. 5 shows a 0.4-0.8 µm order of roughness, which is significantly lower than the 5-µm penetration depth of the X-ray beam. The Etched specimen also offers the same 0.4-0.8 µm order of roughness and proves that etching will not affect the surface finish quality that much to be a concern for the XRD test. This matter promises that the surface roughness will not affect the X-ray stress measurement accuracy on the etched specimen.

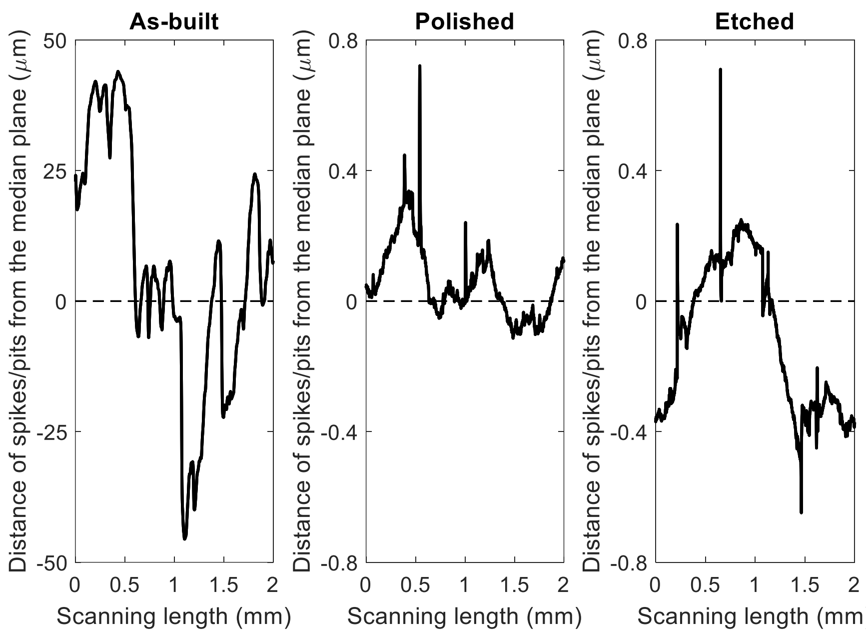

Figure 10.5 Surface roughness measurement of the XRD specimen at different conditions; before polishing (i.e., As-built), after polishing (i.e., Polished), and after etching (i.e., Etched)

3.1.2. Stress measurement strategy

A typical XRD phase scan analysis from the weld and rail materials is given in Figs. 6a and 6b, respectively. As it is intended to obtain a precise measurement of strain owing to lattice spacing variations, the residual stresses are recommended to be measured at the highest possible diffraction angles as long as it does not considerably affect the measurement accuracy [35].

According to Fig. 6a, the stress in the weld section (points 1 to 5 in Fig. 2d) is measured at the BCC(310) diffraction peak (diffraction angle (2θ) of 115.1°). Furthermore, residual stress measurement in the rail section (points *a* and *b* in Fig. 2d) is conducted at the diffraction peak of BCC(310), which is located at the diffraction angle of 116.2° (Fig. 6b).

The $sin^2\psi$ method is utilized for stress calculation. Starting from $\psi=0°$ and stepwise adding five equal offsets up to $\psi=45°$, a total of six ψ points are taken into account. The assigned range of diffraction angle for the XRD measurements is $114° \leq 2\theta \leq 118°$ with a stepwise increment of 0.02, where 0.8 seconds per step of counting accumulation is employed. Sliding gravity is used for the peak evaluation, and data correction for Lorentz-polarization background and absorption is undertaken.

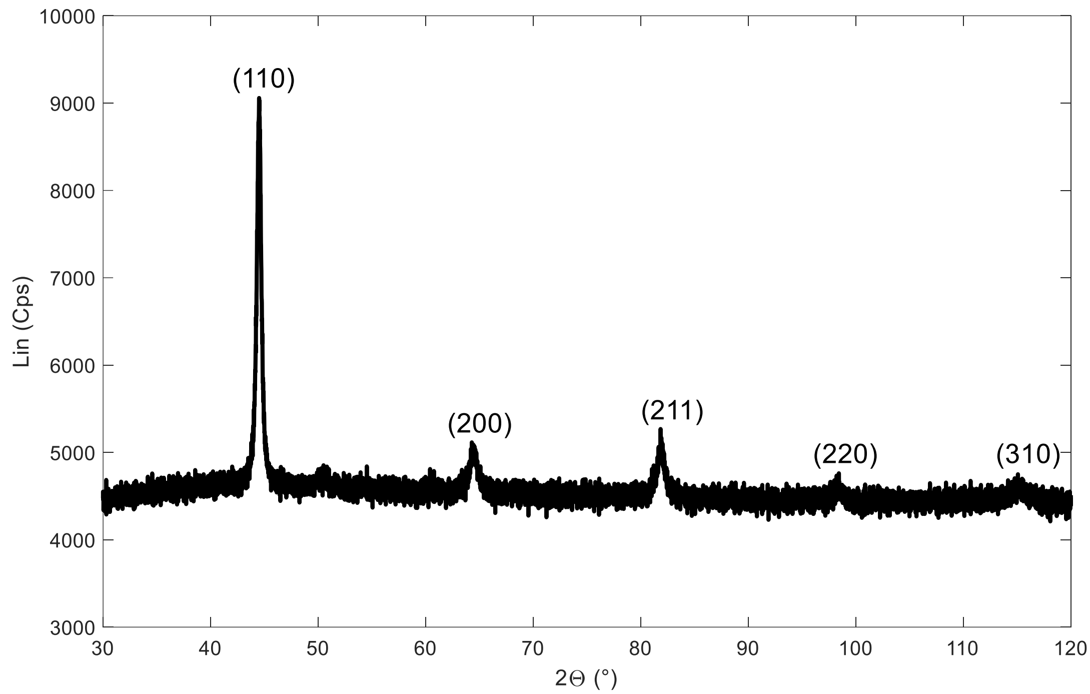

(a)

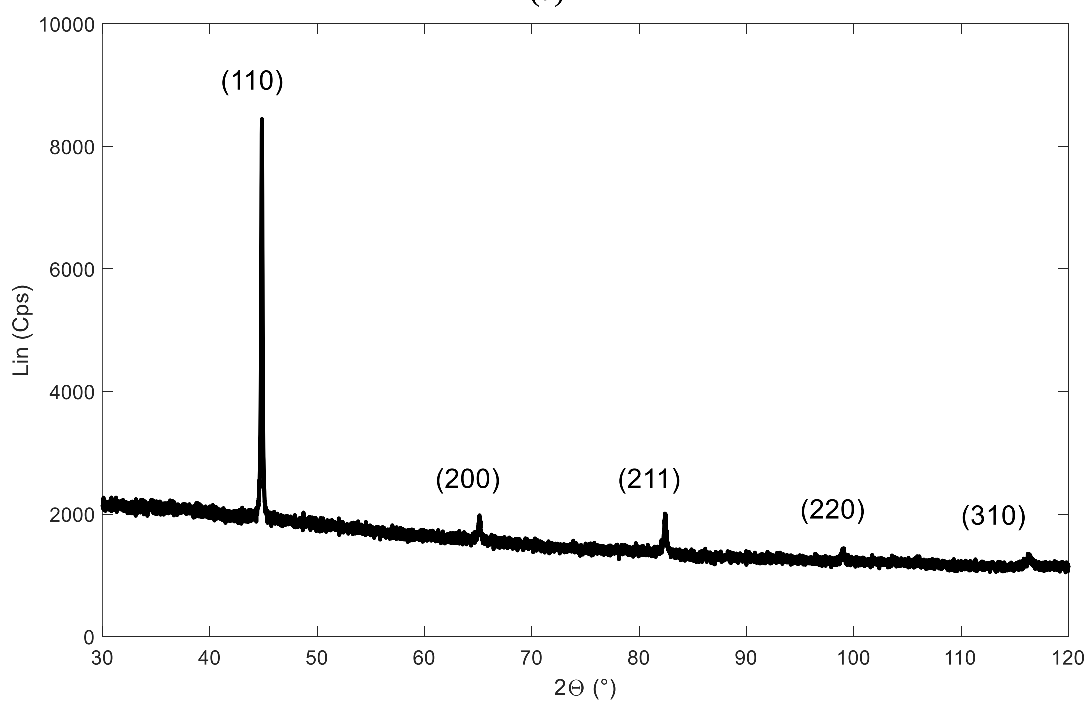

(b)

Figure 10.6 XRD phase scan analysis at the (a) weld section and (b) rail section of the repaired rail

3.1.3. Measurement Verification

The Polished sample (shown in Fig. 2c) is etched in several steps until the measured stress is stabilized. This stabilization happens when further layer removal would not result in sensible changes in the measured stresses. This action is to validate residual stresses measurement using XRD and ensure no additional residual stresses affect the results,

Per Fig. 2d, spot 1 (shown in red) is picked as the base point at which stress measurement is performed at different stages of the specimen. These stages include the As-built stage (A-B in Fig. 7), Polished (P in Fig. 7), and Etched (E1-E5 in Fig. 7, the sample is etched five times after polishing, indicated as E-1 after the first time of etching, E-2 after the second time of etching, and so on. The Depth parameter in Fig. 7 represents the distance of the existing surface of the specimen from the base surface in the As-built condition. For example, polishing removed 750 µm from the As-built surface, and each step of etching removes another 50-µm layer from the specimen surface. The measured in-plane longitudinal and transversal stresses, i.e., S_{xx} and S_{yy} (refer to Fig. 1 to configure the x and y coordination), are shown in Figs. 7a and 7b, respectively. Polishing could cause a shifting of around 45-50% in the measured stress value. The first reason for such an intensive increase in measured stress can be to remove the interrupting surface spikes, let the X-ray beams penetrate enough to the surface, and measure the existing residual stresses instead of scattering them around. The second reason can be inducing the surface's extra residual stresses during polishing. In addition, the sample is also etched to remove that extra portion of the residual stresses, i.e., the one applied through polishing.

Fig. 7 shows that five etching steps could decrease the measured S_{xx} and S_{yy} by 7% and 20%, respectively. A difference between the values of P and E-5 can be seen in this diagram. This difference is technically due to the removing residual stresses caused by polishing. It can be interpreted that Figs. 7a and 7b show no difference between the measured stress in the E-4 and E-5 stages for both the S_{xx} and S_{yy}. Hence, the E-5 specimen is used hereafter for measuring stress at the rest of the spots shown in Fig. 2d.

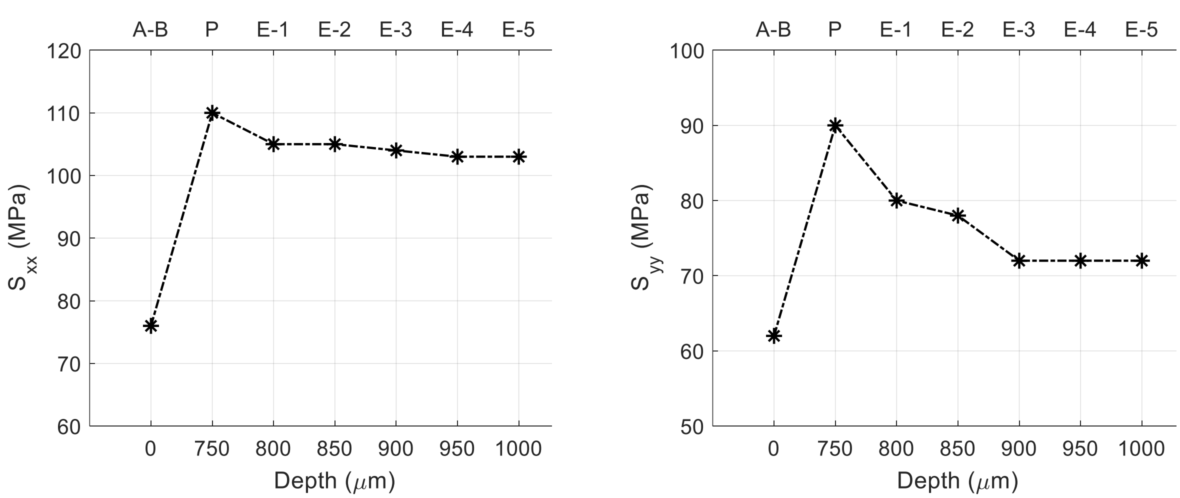

(a) (b)

Figure 10.7 Measured residual stresses using the XRD method at spot 1 (shown in red in Fig. 2d) along the (a) longitudinal and (b) transversal directions at different stages of the specimen; As-built (A-B), Polished (P) and first to fifth time of etching (E-1 to E-5)

3.1.4. Measured stress distribution

Longitudinal and transversal residual stresses, i.e., S_{xx} and S_{yy}, are measured on the E-5 specimen at all the spots shown in Fig. 2d, and Fig. 8 shows their results. The lower *x*-axis shows the distance of each spot from spot 5 (based on Fig. 2d), and the upper *x*-axis marks the corresponding spot number. It should be noted that spots 1 to 5 are located in the weld zone, spot 5 is the farthest, spot 1 is the closest spot to the rail-weld interface, and spots *a* and *b* are in the rail zone, where spot *b* is closer to the rail-weld interface. From the graphs shown in Fig. 8, the rail-weld interface falls somewhere between 16 to 20 mm from spot 5, i.e., between spots 1 and *b*.

According to Fig. 8a, the weld zone carries only tensile S_{xx} with the maximum values of 91 and 103 MPa located at spots 5 and 1, respectively, representing the top surface of the weld and the area near the rail-weld interface, respectively. The minimum tensile S_{xx} of 55 MPa in the weld area is found in the middle section at spot 3. A tensile-to-compressive stress transition happens at the rail-weld interface, i.e., from spot 1 to *b*, where the maximum tensile S_{xx} of 103 MPa in the weld section transforms to the maximum compressive S_{xx} of 10 MPa in the rail section. It is seen that S_{xx} in the lower areas of the rail (i.e., point *a*) switches back to tensile but stays at low and relatively negligible values.

Regarding the transversal stress (S_{yy}) in Fig. 8b, almost the same pattern can be figured out. The maximum tensile S_{yy} values of 78 and 75 MPa in the weld materials are found at spots 5 and 1, respectively. A compressive stress of 2 MPa is located at spot *b*, in the rail area close to the rail-weld interface. A near-zero S_{yy} happens in lower areas of the rail at spot *a*.

At the time of starting the SAW process, a sudden temperature rise happens, which leads to a rapid expansion of the rail surface. However, the deposited weld layer tends to shrink due to fast cooling through convection with the air and conduction with the bulk rail substrate. The collision of the two phenomena causes applied stresses due to expansion-shrinkage interactions. These stresses are tensile from rail to weld and compressive from weld to rail (spots 1 and *b* in Fig. 8, respectively). After depositing the first weld layer, the substrate is already at a high temperature, so depositing other layers will not experience high tensile stress similar to the first layer. This matter explains the lower tensile stresses in the middle layers (spots 2 to 4 in Fig. 8). However, the last weld layer, i.e., the top layer, cools down faster than the lower layers due to direct exposure to the air. Besides, unlike the lower weld layers, the top layer cannot relieve a portion of its residual stress by getting reheated owing to depositing a new layer on the top. That is why the tensile stress grows again in the upper areas of the weld (spot 5 in Fig. 8).

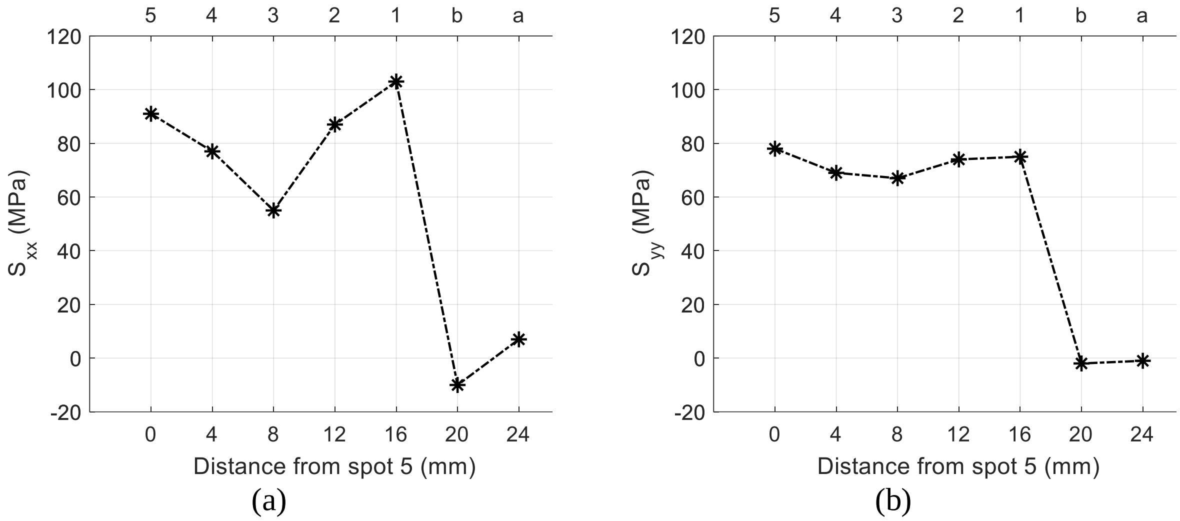

Figure 10.8 Measured (a) longitudinal and (b) transversal residual stresses using XRD on the E-5 specimen at all the spots shown in Fig. 2d; the upper *x*-axis shows the spot numbers, and the lower *x*-axis shows their distance from spot 5

3.2. Microstructural Analysis

Optical Microscope (O.M.) captures from the etched specimen, which is extracted from the repaired rail, are shown in Fig. 9. In Fig. 9a, the etched specimen is divided into three areas of weld, heat-affected zone (HAZ), and rail. It is seen in Fig. 9b that the weld area contains four layers with different compositions/orientations in the microstructure. A closer look into the microstructure of the fourth, third, second, and first weld layers is shown in Figs. 9c, 9d, 9e, and 9f, respectively. Close-up O.M. captures from the HAZ, and rail can be found in Figs. 9h and 9j, respectively. The interfaces between weld and HAZ and between HAZ and rail are in Figs. 9g and 9i, respectively. The distribution of the chemical elements throughout the examined areas in Fig. 9 is given in Table 3.

Fig. 9j shows that a dendritic thin lamellar pearlite microstructure is detectable for the rail. It is obviously seen that the rail microstructure contains coarse, light islands of pro-eutectoid ferrite and dark-etched, dendritic pearlite lamellae that are randomly oriented. Sporadic signs of dissipated carbides are also traceable over the pearlitic-ferritic matrix.

Per the *Fe-Cr* phase diagram shown in Fig. 10, the utilized Lincore 40-S weld wire with around 0.5 weight percentage (*wt.%*) of chromium (referring to Table 1) has a mixture of BCC phases containing *Fe-rich (BCC)* and *Cr-rich (BCC')* alloy compounds at room temperature. The XRD analysis showed the weld material's general BCC phase (Sec. 3.1.2). A linked investigation and four weld layers' chemical distribution resulted in no chance of austenite (γ) formation. The link investigation can be found as a dotted line in Fig. 10. Table 3 also shows weld layers' chemical distributions with a *Cr-wt.%* interval of 0.32 to 0.47. The γ loop falls between 0 to 0.12 *wt.%* of *Cr* content, which is not contained in the current case study. Hence, it is guaranteed that none of the distinguished phases in the O.M. morphology represent any austenite. A close inspection of the weld layers in Figs. 9c to 9f suggest three discernible regions, primarily categorized based on their brightness appearances. The light region represents the Alpha-ferrite (α-*Fe*) phase, the dark network stands for the acicular Alpha-chromium (*α-Cr*) phase, and the brittle sigma (σ) phase appears as a semi-dark zone. A general rule of thumb attributed to the *Fe-Cr* phase diagram is that as the *Cr-wt.%* increases from 0 to 1, a light-etched to dark-etched transition occurs; the austenite with the lightest appearance in an HCL-etched carbon steel nucleates at $0 \leq Cr\text{-}wt.\% < 0.12$, then, at $Cr\text{-}wt.\% \geq 0.12$, a combined *α-Fe* + *α-Cr* phase forms, which starts with the dominancy of the light-etched *α-Fe* at *Cr-wt.%*=12 and smoothly transforms to a dark-etched, *α-Cr*-dominant compound as the *Cr-wt.%* leans towards 1. Table 3 shows a declined flow of *Cr-wt.%* from Layer 1 to 4. The liquidus weld drops at 1600-1700°C, and the preheated railhead surface has a temperature of 200-300°C, so the weld materials start to experience an initially fast cooling procedure down to 500-700°C during the first layer of welding on the railhead surface. The temperature range with a closer tendency to the railhead temperature because of the large amount of bulk material. It then remains at that temperature interval for a while. Anyway, once the second layer is started to weld on top of the first layer, Layer 1 is reheated and has a chance for long exposure at a higher temperature range, i.e., 700-1000°C. In the meantime, Layer 2, with a higher initial substrate temperature (i.e., 500-700°C), remains at elevated temperatures around 700-1000°C until the third layer starts to get welded on top of it. This trend proves that the top layers are exposed to higher ranges of temperature, i.e., higher than 500-800°C. Based on Fig. 10, for the utilized *Fe-Cr* weld alloy where *Cr-wt.%* is measured to be in the 0.32-0.47 range, long exposures to 500-800°C give enough time for $\alpha \rightarrow \sigma$ transition. The longer the exposure time, the higher the fraction of α would have the opportunity to transform to the brittle σ. Besides, higher *wt.%* of *Cr*, i.e., closer to 0.47, leads to a higher chance of complete $\alpha \rightarrow \sigma$ transition at 500-800°C, while lower *Cr-wt.%*, i.e., closer to 0.32, yields to partial $\alpha \rightarrow \sigma$ transformation. In other words, higher *wt.%* of *Cr* results in higher precipitated σ but lower *Cr-wt.%* gives a lower fraction of the brittle σ phase in the final microstructure. This fact clearly explains why the fraction of the semi-dark σ area decreases from Layer 1 (Fig. 9f) to Layer 2 (Fig. 9e), to Layer 3 (Fig. 9d), to Layer 4 (Fig. 9c). Layer 1 with higher reheating opportunities had longer available time to stay at 500-800°C and undertake the $\alpha \rightarrow \sigma$ transformation process. By moving to the upper layers, the number of reheating opportunities decreases, and the length of the 500-800°C exposure time decreases, hence the chance of $\alpha \rightarrow \sigma$ decreases. Therefore, lower fraction of brittle σ remains in the final microstructure at room temperature. Another observable fact is that as the *Cr-wt.%* decreases from Layer 1 to Layer 4 (see Table 3), the volume fraction of the *Cr*-rich α, i.e., *α-Cr*, decreases, and that of the *Fe*-rich α, i.e., *α-Fe*, increases. Therefore, layer 1 (Fig. 9f), with the highest amount of lowest *Cr-wt.%*, contains the highest dark α-Cr volume fraction among the four weld layers. While layer 4 has (Fig. 9c) the lowest amount of this fraction. Another contributor to the increment of the ferrite phase in the upper layers is that the *wt.%* of the ferrite stabilizers (*Mo* and *Si*) has an increasing trend from Layer 1 to Layer 4 (Table 3). So this matter describes the increasing of the light-etched *α-Fe* area from the first layer (Fig. 9f) to the fourth (Fig. 9c).

When layers of materials are welded on the top of a substrate, the sandwiched HAZ, based on the findings of Shen et al. [36], contains a combined mixture of the weld and the substrate materials. On the one hand, based on Fig. 9g, as we go down from weld to the HAZ, the concentration of *α-Cr* increases, and *α-Fe* is dissipated throughout the dark *α-Cr* matrix. Table 3 shows that the ferritizers (i.e., *Mo* and *Si*) experience a significant descent from Layer 1 downwards to the HAZ. Therefore, in their absence, *α-Fe* does not have enough stability and easily dissipates in favor of α-Cr. On the other hand, referring to Fig. 9i, moving upward from rail to the HAZ, the dark pearlite has been segregated and moved on to the HAZ, but a minor fraction of the pro-eutectoid ferrite could successfully migrate through to the HAZ. Hence, the core of the HAZ, as observable in Fig. 9h, mainly consists of pearlite and α-Cr, with dark appearances, and contains a minor fraction of ferrite with light appearance.

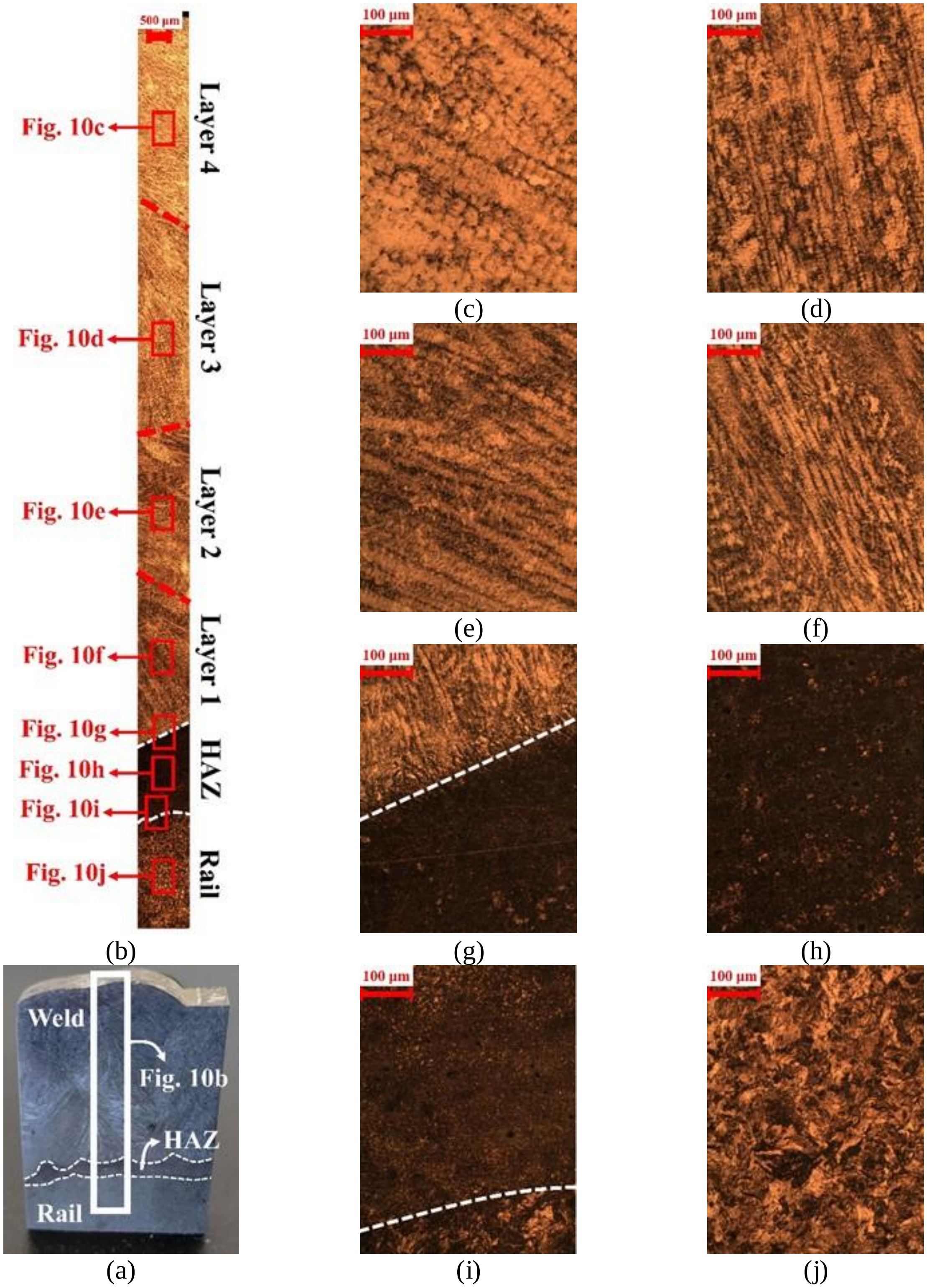

Figure 10.9(a) An etched specimen extracted from the head of the repaired rail, (b) A thorough O.M. capture from the entire weld zone with the four layers deposited, the heat-affected zone (HAZ), and the rail; closer O.M. shots are taken from (c) fourth, (d) third, (e) second, and (f) first weld layers, (g) weld-HAZ interface, (h) HAZ, (i) HAZ-rail interface, and (j) rail

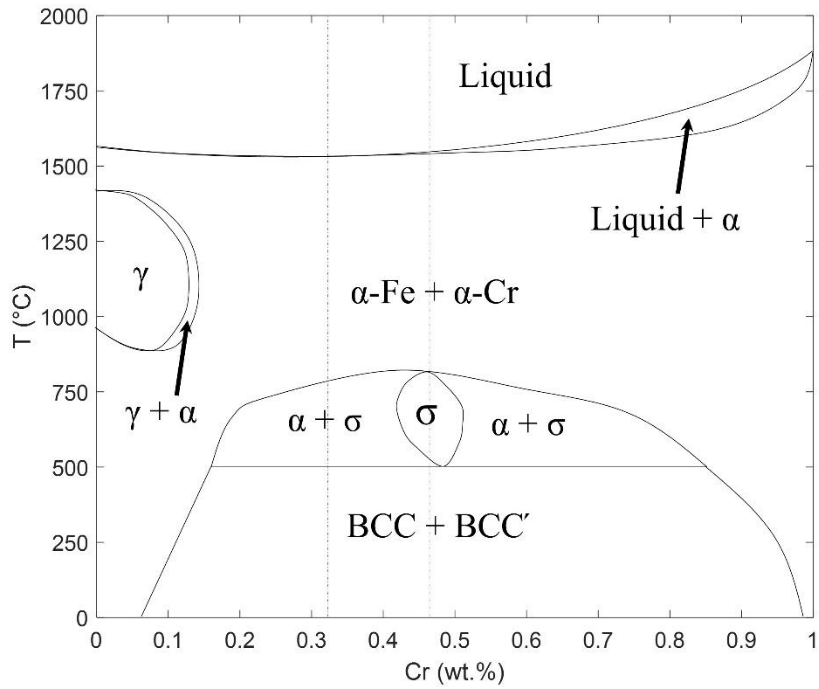

Figure 10.10 Fe-Cr phase diagram for the Lincore 40-S hard-facing wire used in the SAW process

Table 3 Chemical composition (wt.%) of different areas of the repaired rail (Areas are graphically addressed in Fig. 10)

Area	Fe	C	Cr	Mn	Mo	Si
Layer 4	Bal.	0.067 ± 0.007	0.32 ± 0.05	1.25 ± 0.20	0.82 ± 0.03	3.42 ± 0.40
Layer 3	Bal.	0.028 ± 0.007	0.39 ± 0.05	1.93 ± 0.20	0.80 ± 0.03	3.26 ± 0.40
Layer 2	Bal.	0.016 ± 0.007	0.41 ± 0.05	2.55 ± 0.20	0.73 ± 0.03	3.12 ± 0.40
Layer 1	Bal.	0.017 ± 0.007	0.47 ± 0.05	2.19 ± 0.20	0.73 ± 0.03	2.94 ± 0.40
HAZ	Bal.	0.23 ± 0.06	0.12 ± 0.01	1.01 ± 0.20	0.03 ± 0.01	0.53 ± 0.40
Rail	Bal.	0.80 ± 0.06	0.03 ± 0.01	0.23 ± 0.03	-	0.04 ± 0.01

3.3. Hardness Test

Per AREMA regulations [30], the distribution of Hardness along the three lines, shown in Fig. 11a, should be maximum at the surface of the railhead, i.e., points 1, 11, and 25 in Fig. 11a, and then undergo a smooth declination towards the minimum Hardness at the root of the railhead, i.e., point 39 in Fig. 11a.

Fig. 11 gives the hardness distribution along the repaired railhead's left, middle, and right gauges (i.e., Lines 1, 2, and 3, respectively, in Figs. 11b, 11c, and 11d, respectively). The minimum required Hardness assigned by AREMA [30] for heavy 136RE rails, equal to 32 HRC, is shown as a horizontal dash-dot line in all the graphs. The vertical dashed line in each graph locates the rail-weld interface. Therefore, the areas on the left side of the vertical dashed lines in Figs. 11b, 11c, and 11d represent the weld area, and the areas on the right side of them stand for the rail area. It is evident in Figs. 11b-d that the average measured Hardness at the weld zone along Lines 1, 2, and 3 are 54, 59.5, and 60 HRC, respectively. The mean Hardness measured in the rail section along Lines 1, 2, and 3 is 37, 35, and 36 HRC, respectively. Therefore, the overall Hardness in the weld and rail areas is estimated as 58 HRC and 36 HRC, respectively. The results imply that the hardness results meet the standard AREMA requirement: the maximum occurs at the head, and the minimum occurs at the root of the repaired railhead. The Hardness of the repaired rail in almost all the regions is higher than the minimum required 32 HRC. Still, it fails to meet the AREMA standards regarding a smooth declination, from the maximum at the head to the minimum at the root. Graphs in Figs. 11b-d shows a sharp, step decrease of Hardness at the rail-weld interface, moving from the weld area to the rail zone.

The most challenging phase present in the weld material is the brittle σ phase. The sigma phase can significantly increase the Hardness. Unlike martensite, the sigma phase in the railhead microstructure is not against AREMA regulations. However, it substantially affects the material ductility by increasing the brittleness, which raises the chance of premature cracking and failure of the rail under dynamic wheel-rail load. Therefore, while the weld's higher (about 80% higher than the minimum required) seems satisfying, it might make the deposited weld too brittle and hence need some post-heat-treatment (e.g., tempering) to alleviate the Hardness down to some values closer to the minimum 32 HRC. So, not only can the Hardness meet the minimum standards, but also the material becomes more ductile to decrease the chance of early cracking and premature failure. Another contributor phase to getting a high hardness in the weld zone is the *α-Fe* phase. The volume fractions of σ and *α-Fe* respectively decrease and increase in weld layers from the base rail to the top surface (Sec. 3.2). Hence although one of the hardness-increment-contributors (i.e., the volume fraction of σ) decreases, the other contributor (i.e., the volume fraction of *α-Fe*) increases in the upper layers. So this matter explains the almost constant, high Hardness in the weld area (Fig. 11). The Hardness of the weld zone remains between 55 to 60 HRC, and no considerable fluctuation occurs.

As the hard *α-Fe* and the brittle σ phases disappear in the HAZ while the mild-hardness *α-Cr* increases, the Hardness suddenly descends from 55-60 HRC to around 40 HRC. After that, in the rail area with the standard pearlitic-ferritic phase, the hardness values match the standard expected values between 32 to 42 HRC, converging to 32 HRC at the root of the repaired rail (Fig. 11).
Thus, a proper choice of heat treatment, such as tempering, can dissolve the brittle σ phase and help to augment the ferrite phase in the weld zone. This microstructural transformation could make a consistent hardness distribution all over the repaired railhead and aid the weld material's Hardness to reduce to the standard 32-40 HRC interval.

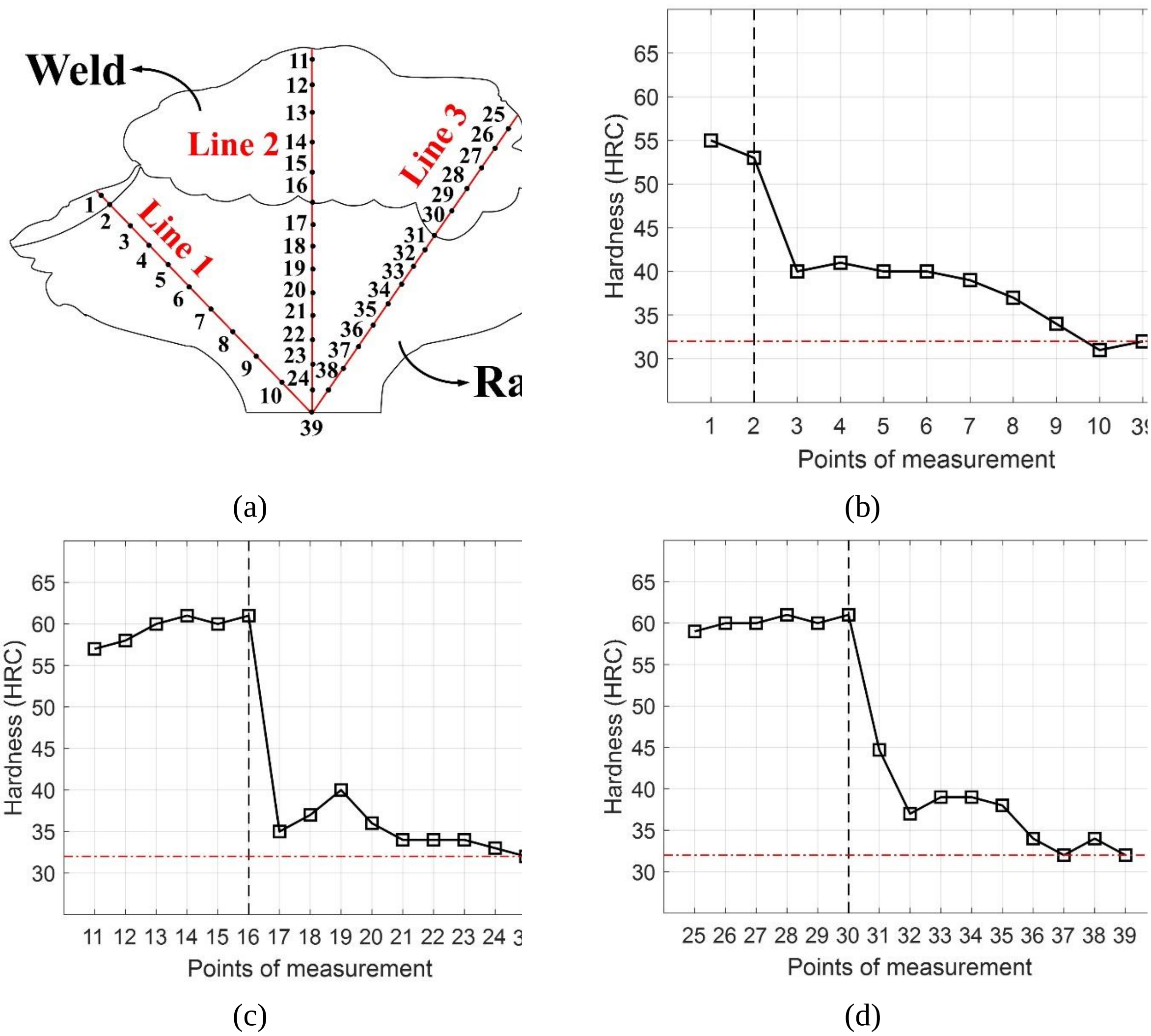

Figure 10.11 Hardness distribution on the head of the repaired rail showing the (a) hardness test plan and hardness distribution along (b) Line 1, (c) Line 2, and (d) Line 3; the vertical dashed line in all of the graphs located the rail-weld interface and the horizontal red dash-dot line shows the minimum acceptable Hardness based on AREMA standards [30]

3.4. Tensile Test

Four specimens were prepared based on the explanation in Sec 2.3.4. Two of them were extracted from the weld area, and the other two from the base area of the rail. The two base samples were used to check the results from the weld samples. The results also assessed to meet the AREMA regulations [30]. Fig. 12 shows the stress-strain diagrams resulting from the samples. The average data used for every two specimens from the weld or base area. Extracted data from the tensile test and, after averaging and removing noises, formed the diagrams shown in Fig. 12.

Failure shape is one of the essential characteristics of each tensile sample. In this regard, fig 13 shows two samples from the weld area broke with a cross-section perpendicular to the tensile axis. This matter is due to the brittle weld metal structure mentioned in Sec. 3.3. In contrast, base area samples showed a ductile form. Fig 12.b. indicates that the base area samples passed the elastic region and went to the plastic part. Although the base samples did not break according to the maximum load tensile machine limitation, these results are still proper to compare with the weld area samples. This matter also approved the previous statement regarding ductility in the base area and being brittle in the weld area (Sec. 3.3.). As was mentioned in Sec. 3.3., a heat treatment process, such as tempering, should be considered in the weld area.

From the diagram of Fig. 12.a., the Ultimate Tensile Strength (UTS) be calculated as 550 MPa. This value can still meet the AREMA regulations [30]. However, as mentioned before, the brittle structure can cause a considerable flaw in the rail surface. The difference between the weld area's behavior and the base area indicates that the weld area can tolerate static loads. However, fatigue and dynamic loads can cause a significant problem. It could be mentioned that Yield Strength (S_y) is 700 MPa by consideration of the 0.2% offset method (shown in Fig. 12.b.).

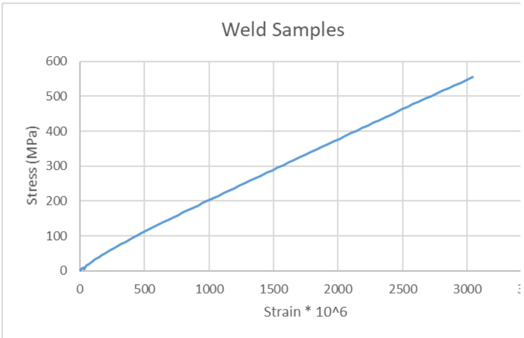

(a)

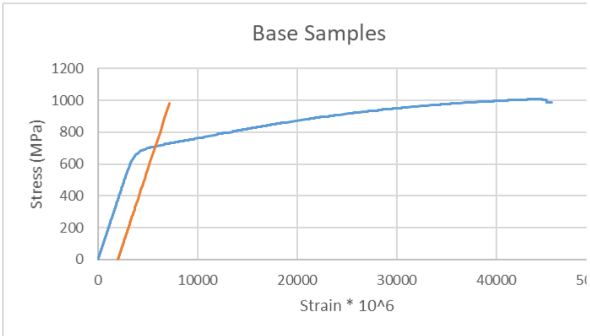

(b)

Figure 10.12 Stress-Strain diagram resulting from tensile tests on samples of (a) weld area and (b) base area

(a)

(b)

Figure 10.13 Failure shapes of the weld area samples

Conclusion and Future Work

The current study has assessed the mechanical and metallurgical properties of a standard U.S. heavy rail repaired using SAW (Submerged Arc Surfaced), focusing on the weld area. Some different experiments have been designed and implemented to investigate the goal of this research, including XRD residual stress measurement, SEM/OM analysis, hardness test, and tensile test.

Through these tests, a comprehensive interpretation has resulted regarding the method of heavy rail repair by SAW welding.

The experiments show that the repaired weld area of the rail can give proper mechanical strength. However, the quality of the repaired area cannot reach the original rail's steel according to the brittle structure of this area. Therefore, the focus needs to be on the improvement of this structure. Progress in this area can help us achieve a reliable method of rail repair and could be beneficial in other heavy steel weld repair applications, such as structures. Some preheating ways, like tempering, seem suitable in this regard, but they still need more study, which can be material for future research.

References

[1] R. Masoudi Nejad, F. Berto, 2022. Fatigue crack growth of a railway wheel steel and fatigue life prediction under spectrum loading conditions, Int. J. Fatigue, 157, 106722. https://doi.org/10.1016/j.ijfatigue.2022.106722

[2] S. Zhang, M. Spiryagin, Q. Lin, H. Ding, Q. Wu, J. Guo, Q. Liu, W. Wang, 2022. Study on wear and rolling contact fatigue behaviours of defective rail under different slip ratio and contact stress conditions, Tribol. Int., 169, 107491. https://doi.org/10.1016/j.triboint.2022.107491

[3] G. Epasto, F. Distefano, L. Gu, H. Mozafari, E. Linul, 2020. Design and optimization of Metallic Foam Shell protective device against flying ballast impact damage in railway axles, Mater. Des., 196, 109120. https://doi.org/10.1016/j.matdes.2020.109120

[4] K. Zhou, H. Ding, W. Wang, J. Guo, Q. Liu, 2022. Surface integrity during rail grinding under wet conditions: Full-scale experiment and multi-grain grinding simulation, Tribol. Int., 165, 107327. https://doi.org/10.1016/j.triboint.2021.107327

[5] R.F. Kral, S.A. Mayhill, M.Q. Johnson, M.E. Rovnyak, D.J. Coomer, 2004. Method of repairing a rail, U.S. Patent, US7520415B2 2004

[6] J.W. Seo, J. Kim, S.J. Kwon, H.K. Jun, 2019, Effects of laser cladding for repairing and improving wear of rails, Int. J. Precis. Eng. Manuf., 20, 1207–1217. https://doi.org/10.1007/s12541-019-00115-y

[7] S.H. Lee, S.H. Kim, Y.S. Chang, H.K. Jun, 2014. Fatigue life assessment of railway rail subjected to welding residual and contact stresses, J. Mech. Sci. Technol., 28, 4483–4491. https://doi.org/10.1007/s12206-014-1016-3

[8] H.K. Jun, J.W. Seo, I.S. Jeon, S.H. Lee, Y.S. Chang, 2016. Fracture and fatigue crack growth analyses on a weld-repaired railway rail, Eng. Fail. Anal., 59, 478–492. https://doi.org/10.1016/j.engfailanal.2015.11.014

[9] Q. Feng, H. Song, 2022. Analysis on the operation methods of rail welding and postweld heat treatment in the track change overhaul of existing railway lines, J. Phys.: Conf. Ser., 2152, 012018. https://doi.org/10.1088/1742-6596/2152/1/012018

[10] P. Chen, L. Chen, J. Xu, S. Huang, Z. Xia, 2021. Formation mechanism of pearlite during thermal cycling in U75V steel rail repaired by laser directed energy deposition, J. Laser Appl., 33, 032017. https://doi.org/10.2351/7.0000446

[11] P. Suwanpinij, T. Thonondaeng, P. Kumma, B. Suksawat, G. Lothongkum, 2022. Control of the bainitic structure for a wear-resisting hard-faced rail track, Mater. Test., 64 (1), 1-10. https://doi.org/10.1515/mt-2021-2076

[12] B. Srikarun, S. Petchsang, P. Muangjunburee, 2021. Study of abrasive wear of railway welding steel repair, grade R260, Princess of Naradhiwas University Journal, 13 (1) , 209–255. https://li01.tci-thaijo.org/index.php/pnujr/article/view/241123

[13] M.N. SaifulAkmal, M.N. Wahab, 2021, Characterization of UIC-54 rail head surface welded by hardfacing using flux-cored steel wire, In: M.N. Osman Zahid et al. (eds), Recent trends in manufacturing and materials towards industry 4.0. Lecture notes in mechanical engineering. https://doi.org/10.1007/978-981-15-9505-9_68

[14] T. Roy, A. Paradowska, R. Abrahams, M. Law, P. Mutton, M. Soodi, W. Yan, 2020. Residual stress in laser cladded heavy-haul rails investigated by neutron diffraction, J. Mater. Process. Technol., 278, 116511. https://doi.org/10.1016/j.jmatprotec.2019.116511

[15] D. De Becker, J. Dobrzanski, Y.M. Goh, L. Justham, 2020. Towards the development of a deposition technology for an automated rail repair system, UKRAS20 Conference: Robots into the Real World Proceedings, 100-102. https://doi.org/10.31256/Vz2Jt4I

[16] E. Kabo, A. Ekberg, M. Maglio, 2019. Rolling contact fatigue assessment of repair rail welds, wear, 436–437, 203030. https://doi.org/10.1016/j.wear.2019.203030

[17] L. Xin, V. Markine, I. Shevtsov, 2018, Analysis of the Effect of repair welding/grinding on the performance of railway crossings using field measurements and finite element modeling. Proc. Inst. Mech. Eng. F: J. Rail Rapid Transit, 232 (3), 798-815. https://doi.org/10.1177/0954409717693960

[18] E. Mortazavian, Z. Wang, H. Teng, 2022, Finite element investigation of thermal-kinetic-mechanical evolutions during laser powder deposition as an innovative technique for rail repair, Int. J. Adv. Manuf. Technol., 118, 319–342. https://doi.org/10.1007/s00170-021-07873-y

[19] E. Mortazavian, Z. Wang, H. Teng, 2021, Effect of heat treatment on microstructure and Hardness of a worn rail repaired using laser powder deposition, Int. J. Transp. Sci. Technol. https://doi.org/10.1016/j.ijtst.2021.05.004

[20] E. Mortazavian, Z. Wang, H. Teng, 2021. Measurement of residual stresses in laser 3D printed train rail using X-ray diffraction technique, Proceedings of the ASME 2021 IMECE, V02AT02A005. https://doi.org/10.1115/IMECE2021-69822

[21] E. Mortazavian, Z. Wang, H. Teng, 2020. Repair of light rail track through restoration of the worn part of the railhead using submerged arc welding process, Int. J. Adv. Manuf. Technol., 107, 3315–3332. https://doi.org/10.1007/s00170-020-05208-x

[22] B.L. Josefson, J.W. Ringsberg, 2009. Assessment of uncertainties in life prediction of fatigue crack initiation and propagation in welded rails, Int. J. Fatigue, 31 (8–9), 1413-1421. https://doi.org/10.1016/j.ijfatigue.2009.03.024

[23] A. Masoudi, M. Davarpanah Jazi, M. Mohrekesh, R. Masoudi Nejad, 2022. An investigation of rail failure due to wear using statistical pattern recognition techniques, Eng. Fail. Anal., 134, 106084. https://doi.org/10.1016/j.engfailanal.2022.106084

[24] H. Desimone, S. Beretta, 2006. Mechanisms of mixed mode fatigue crack propagation at rail butt-welds, Int. J. Fatigue, 28 (5–6), 635-642. https://doi.org/10.1016/j.ijfatigue.2005.07.044

[25] A. Skyttebol, B.L. Josefson, J.W. Ringsberg, 2005. Fatigue crack growth in a welded rail under the influence of residual stresses, Eng. Fract. Mech., 72 (2), 271-285. https://doi.org/10.1016/j.engfracmech.2004.04.009

[26] R. Masoudi Nejad, Z. Liu, W. Ma, F. Berto, 2021. Fatigue reliability assessment of a pearlitic Grade 900A rail steel subjected to multiple cracks, Eng. Fail. Anal., 128, 105625. https://doi.org/10.1016/j.engfailanal.2021.105625

[27] S. Bharathi, A. Arul, M. Moshi, S.R. Sundara Bharathi, R. Rajeshkumar, R. Kumar, 2016. Factors influencing submerged arc welding on stainless steel—a review. APRN J. Eng. Appl. Sci., 11 (2). ISSN: 1819-6608
[28] P.T. Houldcroft, 1989. Submerged-arc welding. Abington Publishing, U.K. ISBN: 1855730022
[29] ASTM International, Designation: E18 – 20, 2020. Standard test methods for Rockwell hardness of metallic materials. https://doi.org/10.1520/E0018-20
[30] AREMA Manual for Railway Engineering, 2020. Chapter 4: Rail. American Railway Engineering and Maintenance-of-way Association.
[31] M. Ghasri-Khouzani, H. Peng, R. Rogge, R. Attardo, P. Ostiguy, J. Neidig, R. Billo, D. Hoelzle, M.R. Shankar, 2017. Experimental Measurement of residual stress and distortion in additively manufactured stainless steel components with various dimensions, Mater. Sci. Eng. A, 707, 689-700. https://doi.org/10.1016/j.msea.2017.09.108
[32] C.Y. Poon, B. Bhushan, 1995. Comparison of surface roughness measurements by stylus profiler, AFM and noncontact optical profiler, wear, 190(1), 76-88. https://doi.org/10.1016/0043-1648(95)06697-7
[33] ASTM International, Designation: E8/E8M – 21, 2021. Standard test methods for tension testing of metallic materials. https://dx.doi.org/10.1520/E0008_E0008M-21
[34] ASTM International, Designation: E190 – 21, 2021. Standard test method for guided bend test for ductility of welds. https://doi.org/10.1520/E0190-21
[35] M.E. Fitzpatrick, A.T. Fry, P. Holdway, F.A. Kandil, J. Shackleton, L. Suominen, 2002. Determination of residual stresses by X-ray diffraction. National Physical Laboratory, Measurement Good Practice Guide No. 52.
[36] L. Shen, J. Zhou, X. Ma, X.Z. Lu, J.W. Tu, X. Shang, F. Gao, J.S. Zhang, 2017. Microstructure and mechanical properties of hot forging die manufactured by bimetal-layer surfacing technology, J. Mater. Process. Technol., 239, 147–159. https://doi.org/10.1016/J.JMATPROTEC.2016.08.020

11. Chapter 11 LAB TESTS ON RAILS WITH ESAB SAW EQUIPMENT

Purpose of the tests

After explorative tests using SAW equipment from Miller and ESAB companies in 2022 and 2023, both demonstrated to be superior than LPD technologies in terms of productivity and cost, while maintaining potentially great printing quality, even though LPD could deliver good rail strength, but the printing speed and volume are too slow for industrial application.

Among the two industry-caliber SAW printers, Miller is less reliable in motion control during 3D printing train rail. In addition, Miller machine is equipped with one printing head only, which ESAB can operate with dual head, that potentially could double the 3D printing productivity. We are also impressed with the ESAB lab capabilities and team, which are not seen from other places.

The focus of this research is now on using ESAB SAW printer to explore parameters such as wire, travel speed, flux, voltage, ampere, pre-heat, and inter-pass, to meet the AREMA requirements for train rail [1], which include yield strength, tensile strength, elongation rate, and hardness. Surely there are other requirements [2,3], but those four are critical and could be lab verified in a few weeks each time.

Test scenarios

The ESAB SAW equipment below (figure1) is used as the 3D printer during test. The machine has a control console on top (figure 2), which can be programmed to print train rail with different parameters layer by layer. Wires are packed in two rolls and mounted on the back of the machine, which automatically feed into the equipment to the printing zone.

Figure 11.1 ESAB SAW equipment

Figure 11.2: Control console

Parameters used in test of heave rails and light rails, such as wire material, wire diameter, flus, layer, pass, travel speed, voltage, ampere, pre-heat, and inter-pass, etc., are given in Table 1 and Table 4, respectively.

Table 1: Test parameter for heavy rail

	1	2	3	4	5	6
Wire	Thermaclad 446	Thermaclad 446	Thermaclad 446	Thermaclad 438	Thermaclad 446	Thermaclad 446G
Wire Diameter	5/32"	5/32"	5/32"	1/8"	5/32"	2024/1/16
Flux	R20	R20	R20	R20	R20	R20
Layer #	I-5	I-8	I-2	63-8	1-8	1-9
Pass #	I-24	I-39	1-11	11-42	1-40	1-19
Polarity	DC+	DC+	DC+	DC+	DC+	DC+
ESO	1.25	1.25	1.25	1	1.25	2024/5/8
Amperage	650	650	650	550	650	
Voltage	32	32	32	30	32	27
Travel Speed	24 ipm	24	24	23	24	
Pre-Heat	650˚F	none	300		650	
Inter-pass	750˚F	800	800		800	

Date	5/10/2024	6/20/2024	6/27/2024	6/27/2024	7/18/2024	7/18/2024
Cooling	Air + ceramic insulation	Air only	Air + ceramic insulation	Air + ceramic insulation	Oven 650F 2hr	Oven 650F 2hr

Table 2: Test parameter for light rails

	1	2a	2b	3	3	4	4	85	66	8
Wire	Thermaclad 446	Thermaclad 446	Thermaclad 446	Thermaclad 446	Thermaclad 438	Thermaclad 446	Thermaclad 438	Thermaclad 446	Thermaclad 446G	Thermaclad 446
Wire Diameter	5/32"	5/32	5/32	5/32	1/8"	5/32	1/8	5/32	1/6	5/32
Flux	R20	R20	R20	R20	R20	R20	R20	R20		R20
Layer #	1-8	1-2	3-7	1-3	4-8	1-3	4-7	1-6	1	1-6
Pass #	1-36	1-10	11-32	1-12	13-33	1-13	14-28	1-30	1	1-30
Polarity	DC-	AC	AC	DC+	DC+	DC+	DC+	DC+	DC+	DC+
ESO	1.25	1.25	1	1.25	1	1.25	1	1.25	5/8/24	1.25
Amperage	650	AC	AC	650	550	650	550	650		650
Voltage	34	35	35	32	30	32	30	32	27	32
Travel Speed	24	24	24	24	23	24	23	24		24
Pre-Heat	650˚F	650	650	650	650	600	600	650	600	650
Inter-pass	750˚F	800	800	800	800	800	800	800	800	800
Date	5/23/2024	5/30/2024	5/30/2024	6/6/2024	6/6/2024	6/13/2024	6/13/2024	7/24/2024	7/29/2024	9/11/2024
Cooling	Air + ceramic insulation	Air + ceramic insulation	Air + ceramic insulation	Air + ceramic insulation	Air + ceramic insulation	Air + ceramic insulation	Air+ ceramic insulation	Oven 650F 2hr	Oven 650F 2hr	Oven 650F 4hr

Six sets of 3D printing configurations for heavy rails (136-lb/yd) and eight sets for light rails (75-lb/yd), as shown in Table 1 and Tale 2, are printed on top of the existing rail surface layer by layer. Results are discussed in the next section. Lab test data are given in the Appendix I.

Table 3 summarizes the requirements for heavy and light rails in terms of yield strength, tensile strength, and elongation rate [1,2], therefore, is used in selecting printing wires. There are only two qualified: Thermaclad 438 and Thermaclad 446, which are capable of delivering tensile strength and yield strength for heavy and light rails. ESAB has two wire diameter options: 1/8" and 5/32", which are all being tested at different voltage and amperage during operation.

The results

Results of six different printing configurations for heavy rails is summarized in Table 3, among them, one set of the 3D printing configuration (data 1) shows it exceeds the AREMA standards for rail yield strength, the tensile strength of the rail is in the range but slightly below the AREMA standards. The rail micro-hardness is much higher (data given in the Appendix I) and rail elongation rate is lower than the standards. More studies are needed on the results.

Results of eight different printing configurations for light rails is summarized in Table 4. Among all sets of test data, three sets of 3D printing configurations are promising, with both rail yield strength and tensile strength exceeding the AREMA standards. However, similar to heavy rails, the rail micro-hardness is higher than standards and the rail elongation rate is low. More analyses are needed on the results as some data were finished in September 2024.

Table 3: Required mechanical properties of rails [1,2]

Mechanical property	(Unit)	Light Rail	Heavy Rail
Yield strength	(MPa)	460	830
Tensile strength	(MPa)	511	980
Elongation	(%)	10	10

Table 4: Summarize test data in for light rails

	Test Data (PSI)			AREMA Standard (PSI)			Note
	Tensile Strength	Yield Strength	Elongation Rate	Tensile Strength	Yield Strength	Elongation Rate	
Heavy rail 1	137,000	122,000	2.6%	142,100	120,350	10%	5/29/2024
Heavy rail 2	77,000	63,100	3.15%	142,100	120,350	10%	7/5/2024
Heavy rail 3	100,000	n/a	0.946%	142,100	120,350	10%	7/19/2024
Heavy rail 4	78,400	59,000	2.79%	142,100	120,350	10%	7/19/2024
Heavy rail 5	99,200	64,300	7.59%	142,100	120,350	10%	7/30/2024
Heavy rail 6	86,400	64,500	3.42%	142,100	120,350	10%	7/30/2024

Note: 1) data in blue exceeds AREMA required standards;
2) data in green is slightly below the AREMA standards.

Table 5: Summarize test data in for heavy rails

	Test Data			AREMA Standard			Note
	Tensile Strength	Yield Strength	Elongation Rate	Tensile Strength	Yield Strength	Elongation Rate	
Light rail 1	426.2 mPa	358.6 mPa	2%	511 mPa (74,100 psi)	460 mPa (66,700 psi)	10%	5/8/2024
Light rail 2	x-ray only	n/a	n/a	74,100 psi	66,700 psi	10%	6/4/2024
Light rail 3	134,000 psi	95,400 psi	2.5%	74,100 psi	66,700 psi	10%	6/28/2024
Light rail 4	110,000	n/a	0.95%	74,100 psi	66,700 psi	10%	6/28/2024
Light rail 5	84,500	n/a	9.75%	74,100 psi	66,700 psi	10%	8/16/2024
Light rail 6	136,000	114,000	1.5%	74,100 psi	66,700 psi	10%	8/16/2024
Light rail 7	86,200	11,500	0.293 %	74,100 psi	66,700 psi	10%	9/11/2024
Light rail 8	157,000	113,000	1.55%	74,100 psi	66,700 psi	10%	9/26/2024

Note: 1) data in green exceeds AREMA required standards;
2) Hardness are tested separately and data are reported in the next section.

Lab test results indicate that 3D printing train rails is capable of achieving both yield strength and tensile strength to the AREMA requirements for light rails. But only the yield strength exceeds the requirement for heavy rails. The tensile strength is slightly below the requirements. However, rail hardness in both cases for heavy and light rails is above the AREMA standards, and the elongation rate is below requirements. To solve the hardness and elongation problems, we applied heat treatment to some of the printed rails, improvements are observed, but the satisfactory procedure and parameters are yet to be developed before the project comes to an end.

Conclusions and recommendation

3D printing technologies has been revolutionizing many industries in the last few decades, however, application in heavy and dynamic loading situation, such as train rail is yet to be developed [4]. Some 3D printing technique offers excellent mechanical properties, such as mechanical strength, but due to its rapid cooling nature, materials after 3D printing exhibits low elongation rate and high hardness.

In our lab tests, parameters in data 1 is capable of printing heavy rail with satisfactory yield strength, but more adjustment in wire is needed to improve tensile strength.

With light rails, multiple successes were achieved in 3D printing with yield strength and tensile strength due to light rail requirements are lower than heavy rail.

In all cases, heat treatment procedure needs to be further investigated. Researchers from South Korea [5] 3D printed train wheel using a well-established tempering process and achieved good results. We are fully aware of that train wheel is different from rail in material composition and property. Therefore, post heat treatment techniques are different accordingly.

SAW technique, by nature, it melts pre-formulated wire with electric arc, and using flux to shield oxygen, nitrogen, and other gases from forming air bubbles in the molten metals as they solidify on top of a worn rail. Therefore, excellent mechanical property is achievable in the printing layers with this technology. However, the molten zone is relatively small in volume and freezing process is rapid, which leads to high hardness, low elongation, and stress formation [6-9]. To overcome these issues, heat treatment needs to be paired with SAW process.

The recommendation for future work is as followings:

1) Heat treatment (tempering) is not often given top priority in 3D printing train rails among many researchers, however, our lab test results prove that it is equally important as 3D printing technology development.
2) 3D printing light train rail is viable in our lab test. Future researchers may focus on light rail first before heavy rail.
3) 3D printing heavy rail is more challenging and therefore, better wires need to be explored to further enhance the mechanical property of the printed rail.
4) Other tests, such as fatigue, are needed once the heat treatment technology is successfully developed.

Overall speaking, 3D printing technology could revolutionize the way how industry fix wear and damage on train rail. This research proves that mechanical strength (tensile and yield) is achievable through 3D printing for train rail, especially for light rail. More work needs to be done for tempering rail after 3D printing and also more research is needed on testing other mechanical properties before it could be commercialized.

Reference for Chapter 11

[1] AREMA Manual for Railway Engineering, Chapter 4: Rail, American Railway Engineering and Maintenance-of-way Association (2020).

[2] M.P. Hughes-Cromwick, M. Dickens, Public Transportation Fact Book. 71st edition, American Public Transportation Association, Washington, DC (2020). https://www.apta.com/wp-content/uploads/APTA-2020-Fact-Book.pdf.

[3] ASTM E18-15, Standard test methods for Rockwell hardness of metallic materials, ASTM international (2015). https://doi.org/10.1520/E0018-15.

[4] E. Mortazavian, Z. Wang, H. Teng, Thermal-mechanical study of 3D printing technology for rail repair, IMECE2018-86315 (2019) V002T02A052. https://doi.org/10.1115/IMECE2018-86315.

[5] Byeong-Choo Coo, and Young-Jin Lee, Railway Vehicle Wheel Restoration by Submerged Arc Welding and Its Characterization, 14 May 2020 (doi: 10.3390/sci2020033)

[6] S. Bharathi, A. Arul, M. Moshi, S. R. Sundara Bharathi, R. Rajeshkumar, and R. Kumar, “Factors Influencing Submerged Arc Welding On Stainless Steel-A Review,” vol. 11, no. 2, 2016, [Online]. Available: www.arpnjournals.com

[7] P.T. Houldcroft, Submerged-arc welding, Abington Publishing (1989) UK. ISBN: 1855730022.

[8] M. Ghasri-Khouzani, H. Peng, R. Rogge, R. Attardo, P. Ostiguy, J. Neidig, R. Billo, D. Hoelzle, M.R. Shankar, Experimental measurement of residual stress and distortion in additively manufactured stainless steel components with various dimensions, Mater. Sci. Eng. A 707 (2017) 689-700. https://doi.org/10.1016/j.msea.2017.09.108

[9] H. Essoussi, S. Elmouhri, S. Ettaqi, E. Essadiqi, Heat treatment effect on mechanical properties of AISI 304 austenitic stainless steel, Proc. Manuf. 32 (2019) 883–888. https://doi.org/10.1016/j.promfg.2019.02.298.

Chapter 12
CONCLUSIONS AND RECOMMENDATIONS

In this study, two different AM repair mechanisms, i.e., SAW and LPD, are investigated for repairing two types of worn rails that are most prevalently used in the U.S. transportation system, i.e., 75-lb/yd light rail and 136-lb/yd heavy rail. To achieve this goal, modification and evaluation of the AM-repair procedures are conducted through both experimental lab measurements and numerical analyses, simultaneously. The goal is to obtain optimum AM-repair process parameters in which the repaired rail gets the highest failure strength, the lowest cracks and pores, and the lowest residual stress.

To summarize, the method for finding the optimum AM-repair process parameters for a specific type of rail and a specific AM technique is as follows:

1. Microstructure morphology, chemical distribution, hardness, and residual stresses in the repaired rail sample are investigated using OM, SEM, EDS, hardness tester, and XRD tools. In this way, the existing drawbacks in the repaired rail (e.g. martensite occupation in the railhead or high residual stresses at the rail-deposition interface) are determined.
2. The under-study AM rail repair process (SAW or LPD) is simulated and modeled using FE analysis. The model predictions in the matter of the distribution of microstructure, hardness, and residual stress are compared against the experimental outcomes in order to verify the FE model.
3. Based on the specified defects of the repaired rail in the experimental evaluation, modification approaches such as preheating, altering the deposition/weld materials, post-heat treatment, and altering the AM-repair process parameters are considered to enhance the repaired rail's properties with ultimate aim of enhancing its fatigue performance.
4. The proposed modification approaches are tried through the validated FE model to find the best combination of parameters, materials, and pre- and post-processes that lead to the strongest repaired rail.
5. The confirmed optimum combination of parameters is tried experimentally to ensure that the satisfactory outcomes are gained in reality as well. Through many hundreds of lab tests, one set of 3D printing configuration with wire composition produced yield strength exceeding the AREMA standards for heavy rail, tensile strength slight below the standard. Three sets of 3D printing configurations with wire composition produced both yield strength and tensile strength exceeding the AREMA standards for light rails. However, 3D printed rail hardness exceeds the AREMA requirement and rail elongation are low. Indicating post heat treatment is equally important in design and development the 3D printing techniques for rail repair. All lab data for heavy and light rails are given in the Appendix I.

This research presents multiple options including the powder/wire material for the SAW/LPD process, the SAW/LPD process parameters, and the pre- and post-process treatments for a typical AM-repairing of a light/heavy rail in a way to gain the highest fatigue strength for the repaired rail. The other valuable outcome of this research is a reliable FE model to allow parametric studies on a rail-repair procedure without the need to further costs for the experimental tests. Microstructural and mechanical characteristics of the modified and un-modified repaired rails are provided and discussed in detail. The utilized equations in developing the FE model along with the validation procedure are presented in details.

This study provides a novel and efficient way of restoring worn rails on site without the need of removing them from the tracks. This approach would save a considerable amount of time and cost for the U.S. railroad industry, specifically in the railway maintenance section.

Appendix I

ESAB Test Data on Submerged Arc Surfaced Rail

WTTI
WWW.WTTI.COM

WELDER TRAINING AND TESTING INSTITUTE
1144 N. GRAHAM ST. · ALLENTOWN, PA 18109 · TEL 610-820-9551 · FAX 610-820-0271

LABORATORY TEST REPORT

LABORATORY TEST NUMBER: 24050697
COMPANY NAME: ESAB Welding & Cutting Products
IDENTIFICATION ON SAMPLE: Delivered Coupon Identified as HR-1
MATERIAL SPECIFICATION: Delivered Material Identified as Unspecified Weld Metal on Unspecified Rail
DIMENSIONS: Approx. 0.625" Overlay
TYPE OF TEST: Test for Information Only

TENSILE TEST RESULTS
IAW TT-1, Current Revision

TEST DATE: 5/29/2024

MINIMUM TENSILE REQUIRED: Not Specified

SPECIMEN ID	*OD (in)*	*THICKNESS (in)*	*AREA (sq in)*	*TENSILE LOAD (lbs)*	*TENSILE STRENGTH (psi)*	*YIELD LOAD (lbs)*	*YIELD STRENGTH (psi)*	*ELONGATION (%)*	*LOCATION & TYPE OF FAILURE*
1	0.2530	0.1265	0.0503	6,900	137,000	6,130	122,000	2.6	BM-Ductile

NOTES: Reduction of Area: 0.3%
FINAL RESULTS: INFO ONLY
TEST(S) CONDUCTED IN ACCORDANCE WITH: ASTM E8
TEST(S) CONDUCTED BY: KRG
REPORT DATE: 5/31/2024
APPROVED BY: Dennis T. Tobash CWI / WTTI

WTTI Job #: JOB34550

SIGNATURE:

QUALITY POLICY STATEMENT

ACCREDITED
TESTING CERT #3430.01

The services reported in this document were performed in accordance with Welder Training and Testing Institute's Quality System, governed by Quality Manual, Rev. 19, 1/4/23 and AWS Accredited Test Facility (Cert. #900201). WTTI is accredited by A2LA to ISO 17025 for the test methods listed on Testing Cert. 3430.01 and 3430.02. The Scope of Accreditation is available at www.wtti.com. This document shall not be modified or reproduced except in full, without written approval of the laboratory.
These recorded results represent only the specimen(s) tested and are in compliance with applicable code(s), standard(s), and/or contract requirement(s). At no point during testing or inspection at WTTI's facility has this item come into direct contact with mercury, mercury compounds, or devices containing single boundary containment of such. The sample tested meets the requirements of the specification listed however measurement uncertainty has not been analyzed to make a statement of conformance for destructive testing.

Page 1 of 1

Figure A1. Lab Report 1: Heavy Rail #1 - 24050697

WTTI

WWW.WTTI.COM

WELDER TRAINING AND TESTING INSTITUTE

1144 N. GRAHAM ST. · ALLENTOWN, PA 18109 · TEL 610-820-9551 · FAX 610-820-0271

LABORATORY TEST REPORT

LABORATORY TEST NUMBER: 24050850
COMPANY NAME: ESAB Welding & Cutting Products
IDENTIFICATION ON SAMPLE: Delivered Coupon Identified as ID: LR1
MATERIAL SPECIFICATION: Delivered Material Identified as Unspecified Carbon Steel
THICKNESS: 1.050" Overlay
TYPE OF TEST: Test for Information Only
OTHER: Unspecified Filler Metal

TENSILE TEST RESULTS

IAW TT-1, Current Revision

TEST DATE: 6/4/2024

MINIMUM TENSILE REQUIRED: Not Specified

SPECIMEN ID	*OD (in)*	*THICKNESS (in)*	*AREA (sq in)*	*TENSILE LOAD (lbs)*	*TENSILE STRENGTH (psi)*	*YIELD LOAD (lbs)*	*YIELD STRENGTH (psi)*	*ELONGATION (%)*	*LOCATION & TYPE OF FAILURE*
1	0.5030	n/a	0.1990	12,286	61,800	10,300	52,000	2	BM-Ductile

NOTES: Reduction of Area: 1.5%

FINAL RESULTS: INFO ONLY

TEST(S) CONDUCTED IN ACCORDANCE WITH: ASTM E8
TEST(S) CONDUCTED BY: KRG
REPORT DATE: 6/4/2024
APPROVED BY: Dennis T. Tobash CWI / WTTI

WTTI Job #: JOB34627

SIGNATURE: DT

QUALITY POLICY STATEMENT

ACCREDITED
TESTING CERT #3430.01

The services reported in this document were performed in accordance with Welder Training and Testing Institute's Quality System, governed by Quality Manual, Rev. 19, 1/4/23 and AWS Accredited Test Facility (Cert. #900201). WTTI is accredited by A2LA to ISO 17025 for the test methods listed on Testing Cert. 3430.01 and 3430.02. The Scope of Accreditation is available at www.wtti.com. This document shall not be modified or reproduced except in full, without written approval of the laboratory.
These recorded results represent only the specimen(s) tested and are in compliance with applicable code(s), standard(s), and/or contract requirement(s). At no point during testing or inspection at WTTI's facility has this item come into direct contact with mercury, mercury compounds, or devices containing single boundary containment of such. The sample tested meets the requirements of the specification listed however measurement uncertainty has not been analyzed to make a statement of conformance for destructive testing.

Page 1 of 1

Figure A2. Lab Report 2: Light Rail #1 – 24050850

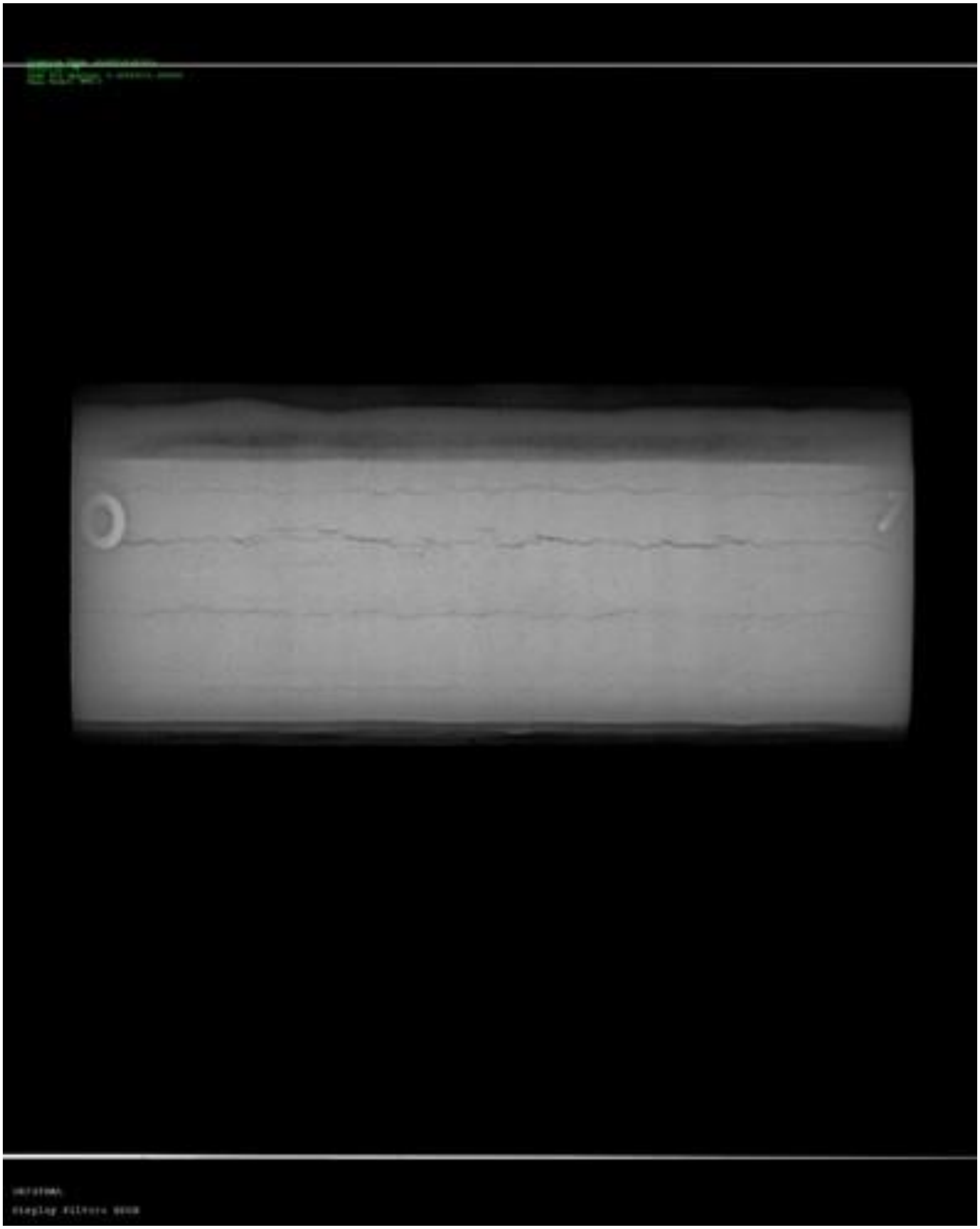

(a)

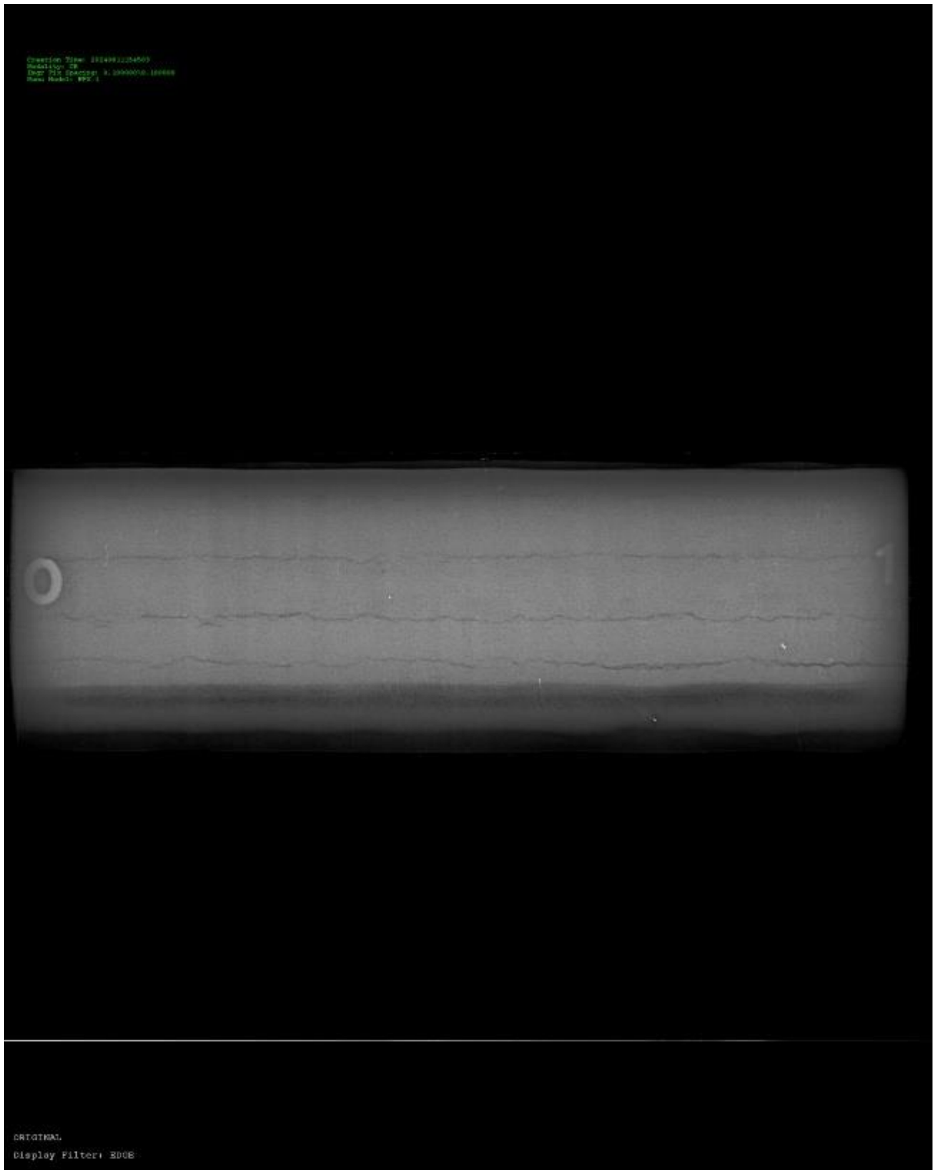

(b)

Figure A3. Lab Report 3: Light Rail #2. No tensile, sample cracked. Here is an X-Ray of the buildup

WTTI
WWW.WTTI.COM

WELDER TRAINING AND TESTING INSTITUTE

1144 N. GRAHAM ST. · ALLENTOWN, PA 18109 · TEL 610-820-9551 · FAX 610-820-0271

LABORATORY TEST REPORT

LABORATORY TEST NUMBER: 24060265
COMPANY NAME: ESAB Welding & Cutting Products
IDENTIFICATION ON SAMPLE: Delivered Coupon Identified as ID: LR3
MATERIAL SPECIFICATION: Delivered Material Identified as Unspecified Carbon Steel
THICKNESS: 0.875" Overlay
TYPE OF TEST: Test for Information Only
OTHER: Unspecified Filler Metal

TENSILE TEST RESULTS

IAW TT-1, Current Revision

TEST DATE: 6/28/2024

MINIMUM TENSILE REQUIRED: Not Specified

SPECIMEN ID	OD (in)	THICKNESS (in)	AREA (sq in)	TENSILE LOAD (lbs)	TENSILE STRENGTH (psi)	YIELD LOAD (lbs)	YIELD STRENGTH (psi)	ELONGATION (%)	LOCATION & TYPE OF FAILURE
1	0.5050	0.2525	0.2000	26,778	134,000	19,100	95,400	2.5	BM-Ductile

NOTES: Reduction of Area: 2.3%

FINAL RESULTS: INFO ONLY

TEST(S) CONDUCTED IN ACCORDANCE WITH: ASTM E8
TEST(S) CONDUCTED BY: KRG
REPORT DATE: 6/28/2024
APPROVED BY: Dennis T. Tobash CWI / WTTI

WTTI Job #: JOB34807

SIGNATURE:

QUALITY POLICY STATEMENT

ACCREDITED
TESTING CERT #3430.01

The services reported in this document were performed in accordance with Welder Training and Testing Institute's Quality System, governed by Quality Manual, Rev. 19, 1/4/23 and AWS Accredited Test Facility (Cert. #900201). WTTI is accredited by A2LA to ISO 17025 for the test methods listed on Testing Cert. 3430.01 and 3430.02. The Scope of Accreditation is available at www.wtti.com. This document shall not be modified or reproduced except in full, without written approval of the laboratory.
These recorded results represent only the specimen(s) tested and are in compliance with applicable code(s), standard(s), and/or contract requirement(s). At no point during testing or inspection at WTTI's facility has this item come into direct contact with mercury, mercury compounds, or devices containing single boundary containment of such. The sample tested meets the requirements of the specification listed however measurement uncertainty has not been analyzed to make a statement of conformance for destructive testing.

Page 1 of 1

Figure A4 Lab Report 4: Light Rail #3 - 24060265

WWW.WTTI.COM

WELDER TRAINING AND TESTING INSTITUTE

1144 N. GRAHAM ST. · ALLENTOWN, PA 18109 · TEL 610-820-9551 · FAX 610-820-0271

LABORATORY TEST REPORT

LABORATORY TEST NUMBER: 24060321
COMPANY NAME: ESAB Welding & Cutting Products
IDENTIFICATION ON SAMPLE: Delivered Coupon Identified as ID: LR4
MATERIAL SPECIFICATION: Delivered Material Identified as Unspecified Carbon Steel with Unspecified Weld Metal Overlay
THICKNESS: 0.875" Overlay
TYPE OF TEST: Test for Information Only
OTHER: Unspecified Filler Metal

TENSILE TEST RESULTS

IAW TT-1, Current Revision

TEST DATE: 6/28/2024

MINIMUM TENSILE REQUIRED: Not Specified

SPECIMEN ID	*OD (in)*	*THICKNESS (in)*	*AREA (sq in)*	*TENSILE LOAD (lbs)*	*TENSILE STRENGTH (psi)*	*YIELD LOAD (lbs)*	*YIELD STRENGTH (psi)*	*ELONGATION (%)*	*LOCATION & TYPE OF FAILURE*
1	0.5080	0.2540	0.2030	22,371	110,000	n/a	n/a	0.95	BM-Ductile

NOTES: Yield Strength would not obtain during testing.
Reduction of Area: 0.0%

FINAL RESULTS: INFO ONLY
TEST(S) CONDUCTED IN ACCORDANCE WITH: ASTM A 370
TEST(S) CONDUCTED BY: KRG
REPORT DATE: 6/28/2024
APPROVED BY: Dennis T. Tobash CWI / WTTI

WTTI Job #: JOB34851

SIGNATURE:

QUALITY POLICY STATEMENT

ACCREDITED
TESTING CERT #3430.01

The services reported in this document were performed in accordance with Welder Training and Testing Institute's Quality System, governed by Quality Manual, Rev. 19, 1/4/23 and AWS Accredited Test Facility (Cert. #900201). WTTI is accredited by A2LA to ISO 17025 for the test methods listed on Testing Cert. 3430.01 and 3430.02. The Scope of Accreditation is available at www.wtti.com. This document shall not be modified or reproduced except in full, without written approval of the laboratory.
These recorded results represent only the specimen(s) tested and are in compliance with applicable code(s), standard(s), and/or contract requirement(s). At no point during testing or inspection at WTTI's facility has this item come into direct contact with mercury, mercury compounds, or devices containing single boundary containment of such. The sample tested meets the requirements of the specification listed however measurement uncertainty has not been analyzed to make a statement of conformance for destructive testing.

Page 1 of 1

Figure A5 Lab Report 5: Light Rail #4 - 24060321

WTTI
WWW.WTTI.COM

WELDER TRAINING AND TESTING INSTITUTE

1144 N. GRAHAM ST. · ALLENTOWN, PA 18109 · TEL 610-820-9551 · FAX 610-820-0271

LABORATORY TEST REPORT

LABORATORY TEST NUMBER: 24060473
COMPANY NAME: ESAB Welding & Cutting Products
IDENTIFICATION ON SAMPLE: Delivered Coupon Identified as ID: HR2
MATERIAL SPECIFICATION: Delivered Material Identified as Unspecified Carbon Steel with Unspecified Overlay
THICKNESS: 0.750" Overlay
TYPE OF TEST: Test for Information Only

TENSILE TEST RESULTS
IAW TT-1, Current Revision

TEST DATE: 7/5/2024

MINIMUM TENSILE REQUIRED: Not Specified

SPECIMEN ID	OD (in)	THICKNESS (in)	AREA (sq in)	TENSILE LOAD (lbs)	TENSILE STRENGTH (psi)	YIELD LOAD (lbs)	YIELD STRENGTH (psi)	ELONGATION (%)	LOCATION & TYPE OF FAILURE
1	0.5040	0.2520	0.1990	15,337	77,000	12,600	63,100	3.15	WM-Ductile

NOTES: Reduction of Area: 1.5%

FINAL RESULTS: INFO ONLY

TEST(S) CONDUCTED IN ACCORDANCE WITH: ASTM E8
TEST(S) CONDUCTED BY: TRR
REPORT DATE: 7/5/2024
APPROVED BY: Dennis T. Tobash CWI / WTTI

WTTI Job #: JOB35014

SIGNATURE:

QUALITY POLICY STATEMENT

ACCREDITED
TESTING CERT #3430.01

The services reported in this document were performed in accordance with Welder Training and Testing Institute's Quality System, governed by Quality Manual, Rev. 19, 1/4/23 and AWS Accredited Test Facility (Cert. #900201). WTTI is accredited by A2LA to ISO 17025 for the test methods listed on Testing Cert. 3430.01 and 3430.02. The Scope of Accreditation is available at www.wtti.com. This document shall not be modified or reproduced except in full, without written approval of the laboratory.
These recorded results represent only the specimen(s) tested and are in compliance with applicable code(s), standard(s), and/or contract requirement(s). At no point during testing or inspection at WTTI's facility has this item come into direct contact with mercury, mercury compounds, or devices containing single boundary containment of such. The sample tested meets the requirements of the specification listed however measurement uncertainty has not been analyzed to make a statement of conformance for destructive testing.

Page 1 of 1

Figure A6 Lab Report 6: Heavy Rail #2 – 24060473

WTTI
WWW.WTTI.COM

WELDER TRAINING AND TESTING INSTITUTE

1144 N. GRAHAM ST. · ALLENTOWN, PA 18109 · TEL 610-820-9551 · FAX 610-820-0271

LABORATORY TEST REPORT

LABORATORY TEST NUMBER: 24070039
COMPANY NAME: ESAB Welding & Cutting Products
IDENTIFICATION ON SAMPLE: Delivered Coupon Identified as ID: HR3
MATERIAL SPECIFICATION: Delivered Material Identified as Unspecified Carbon Steel with Unspecified Weld Metal Overlay
THICKNESS: 1.125" Weld Overlay
TYPE OF TEST: Test for Information Only

TENSILE TEST RESULTS

IAW TT-1, Current Revision

TEST DATE: 7/19/2024

MINIMUM TENSILE REQUIRED: Not Specified

SPECIMEN ID	OD (in)	THICKNESS (in)	AREA (sq in)	TENSILE LOAD (lbs)	TENSILE STRENGTH (psi)	YIELD LOAD (lbs)	YIELD STRENGTH (psi)	ELONGATION (%)	LOCATION & TYPE OF FAILURE
1	0.5030	0.2515	0.1990	19,910	100,000	n/a	n/a	0.946	BM-Brittle

NOTES: Reduction of Area: 0.6%
Specimen did not display a discernable yield point during testing.

FINAL RESULTS: INFO ONLY

TEST(S) CONDUCTED IN ACCORDANCE WITH: ASTM E8
TEST(S) CONDUCTED BY: KRG
REPORT DATE: 7/19/2024
APPROVED BY: Dennis T. Tobash CWI / WTTI

WTTI Job #: JOB35061

SIGNATURE:

ACCREDITED
TESTING CERT #3430.01

QUALITY POLICY STATEMENT

The services reported in this document were performed in accordance with Welder Training and Testing Institute's Quality System, governed by Quality Manual, Rev. 19, 1/4/23 and AWS Accredited Test Facility (Cert. #900201). WTTI is accredited by A2LA to ISO 17025 for the test methods listed on Testing Cert. 3430.01 and 3430.02. The Scope of Accreditation is available at www.wtti.com. This document shall not be modified or reproduced except in full, without written approval of the laboratory.
These recorded results represent only the specimen(s) tested and are in compliance with applicable code(s), standard(s), and/or contract requirement(s). At no point during testing or inspection at WTTI's facility has this item come into direct contact with mercury, mercury compounds, or devices containing single boundary containment of such. The sample tested meets the requirements of the specification listed however measurement uncertainty has not been analyzed to make a statement of conformance for destructive testing.

Page 1 of 1

Figure A7 Lab Report 7: Heavy Rail #3 - 24070039

WTTI

WWW.WTTI.COM

WELDER TRAINING AND TESTING INSTITUTE

1144 N. GRAHAM ST. · ALLENTOWN, PA 18109 · TEL 610-820-9551 · FAX 610-820-0271

LABORATORY TEST REPORT

LABORATORY TEST NUMBER: 24070097
COMPANY NAME: ESAB Welding & Cutting Products
IDENTIFICATION ON SAMPLE: Delivered Coupon Identified as ID: HR4
MATERIAL SPECIFICATION: Delivered Material Identified as Unspecified Carbon Steel with Unspecified Weld Metal Overlay
THICKNESS: 1.00" Weld Overlay
TYPE OF TEST: Test for Information Only

TENSILE TEST RESULTS

TEST DATE: 7/19/2024

IAW TT-1, Current Revision

MINIMUM TENSILE REQUIRED: Not Specified

SPECIMEN ID	OD (in)	THICKNESS (in)	AREA (sq in)	TENSILE LOAD (lbs)	TENSILE STRENGTH (psi)	YIELD LOAD (lbs)	YIELD STRENGTH (psi)	ELONGATION (%)	LOCATION & TYPE OF FAILURE
1	0.5030	0.2515	0.1990	15,581	78,400	11,700	59,000	2.79	BM-Ductile

NOTES: Reduction of Area: 2.5%

FINAL RESULTS: INFO ONLY

TEST(S) CONDUCTED IN ACCORDANCE WITH: ASTM E8
TEST(S) CONDUCTED BY: KRG
REPORT DATE: 7/19/2024
APPROVED BY: Dennis T. Tobash CWI / WTTI

WTTI Job #: JOB35126

SIGNATURE:

QUALITY POLICY STATEMENT

ACCREDITED
TESTING CERT #3430.01

The services reported in this document were performed in accordance with Welder Training and Testing Institute's Quality System, governed by Quality Manual, Rev. 19, 1/4/23 and AWS Accredited Test Facility (Cert. #900201). WTTI is accredited by A2LA to ISO 17025 for the test methods listed on Testing Cert. 3430.01 and 3430.02. The Scope of Accreditation is available at www.wtti.com. This document shall not be modified or reproduced except in full, without written approval of the laboratory.
These recorded results represent only the specimen(s) tested and are in compliance with applicable code(s), standard(s), and/or contract requirement(s). At no point during testing or inspection at WTTI's facility has this item come into direct contact with mercury, mercury compounds, or devices containing single boundary containment of such. The sample tested meets the requirements of the specification listed however measurement uncertainty has not been analyzed to make a statement of conformance for destructive testing.

Page 1 of 1

Figure A8 Lab Report 8: Heavy Rail #4 – 24070097

WTTI

WWW.WTTI.COM

WELDER TRAINING AND TESTING INSTITUTE

1144 N. GRAHAM ST. · ALLENTOWN, PA 18109 · TEL 610-820-9551 · FAX 610-820-0271

LABORATORY TEST REPORT

LABORATORY TEST NUMBER: 24070238
COMPANY NAME: ESAB Welding & Cutting Products
IDENTIFICATION ON SAMPLE: Delivered Coupon Identified as ID: HR5
MATERIAL SPECIFICATION: Delivered Material Identified as Unspecified Carbon Steel with Unspecified Weld Metal Overlay
THICKNESS: 1.00" Weld Overlay
TYPE OF TEST: Test for Information Only

TENSILE TEST RESULTS

IAW TT-1, Current Revision

TEST DATE: 7/30/2024

MINIMUM TENSILE REQUIRED: Not Specified

SPECIMEN ID	OD (in)	THICKNESS (in)	AREA (sq in)	TENSILE LOAD (lbs)	TENSILE STRENGTH (psi)	YIELD LOAD (lbs)	YIELD STRENGTH (psi)	ELONGATION (%)	LOCATION & TYPE OF FAILURE
1	0.5010	n/a	0.1970	19,547	99,200	12,700	64,300	7.59	BM-Ductile

NOTES: Reduction of Area: 9.5%

FINAL RESULTS: INFO ONLY

TEST(S) CONDUCTED IN ACCORDANCE WITH: ASTM E8
TEST(S) CONDUCTED BY: KRG
REPORT DATE: 7/31/2024
APPROVED BY: Dennis T. Tobash CWI / WTTI

WTTI Job #: JOB35241

SIGNATURE:

QUALITY POLICY STATEMENT

ACCREDITED
TESTING CERT #3430.01

The services reported in this document were performed in accordance with Welder Training and Testing Institute's Quality System, governed by Quality Manual, Rev. 19, 1/4/23 and AWS Accredited Test Facility (Cert. #900201). WTTI is accredited by A2LA to ISO 17025 for the test methods listed on Testing Cert. 3430.01 and 3430.02. The Scope of Accreditation is available at www.wtti.com. This document shall not be modified or reproduced except in full, without written approval of the laboratory.
These recorded results represent only the specimen(s) tested and are in compliance with applicable code(s), standard(s), and/or contract requirement(s). At no point during testing or inspection at WTTI's facility has this item come into direct contact with mercury, mercury compounds, or devices containing single boundary containment of such. The sample tested meets the requirements of the specification listed however measurement uncertainty has not been analyzed to make a statement of conformance for destructive testing.

Page 1 of 1

Figure A9 Lab Report 9: Heavy Rail #5 - 24070238

WTTI

WWW.WTTI.COM

WELDER TRAINING AND TESTING INSTITUTE

1144 N. GRAHAM ST. · ALLENTOWN, PA 18109 · TEL 610-820-9551 · FAX 610-820-0271

LABORATORY TEST REPORT

LABORATORY TEST NUMBER: 24070239
COMPANY NAME: ESAB Welding & Cutting Products
IDENTIFICATION ON SAMPLE: Delivered Coupon Identified as ID: HR6

MATERIAL SPECIFICATION: Delivered Material Identified as Unspecified Carbon Steel with Unspecified Weld Metal Overlay

THICKNESS: 1.00" Weld Overlay
TYPE OF TEST: Test for Information Only

TENSILE TEST RESULTS

IAW TT-1, Current Revision

TEST DATE: 7/30/2024

MINIMUM TENSILE REQUIRED: Not Specified

SPECIMEN ID	OD (in)	THICKNESS (in)	AREA (sq in)	TENSILE LOAD (lbs)	TENSILE STRENGTH (psi)	YIELD LOAD (lbs)	YIELD STRENGTH (psi)	ELONGATION (%)	LOCATION & TYPE OF FAILURE
1	0.5010	n/a	0.1970	17,041	86,400	12,700	64,500	3.42	BM-Ductile

NOTES: Reduction of Area: 2.9%

FINAL RESULTS: INFO ONLY

TEST(S) CONDUCTED IN ACCORDANCE WITH: ASTM E8
TEST(S) CONDUCTED BY: KRG
REPORT DATE: 7/31/2024
APPROVED BY: Dennis T. Tobash CWI / WTTI

WTTI Job #: JOB35241

SIGNATURE:

QUALITY POLICY STATEMENT

ACCREDITED
TESTING CERT #3430.01

The services reported in this document were performed in accordance with Welder Training and Testing Institute's Quality System, governed by Quality Manual, Rev. 19, 1/4/23 and AWS Accredited Test Facility (Cert. #900201). WTTI is accredited by A2LA to ISO 17025 for the test methods listed on Testing Cert. 3430.01 and 3430.02. The Scope of Accreditation is available at www.wtti.com. This document shall not be modified or reproduced except in full, without written approval of the laboratory.
These recorded results represent only the specimen(s) tested and are in compliance with applicable code(s), standard(s), and/or contract requirement(s). At no point during testing or inspection at WTTI's facility has this item come into direct contact with mercury, mercury compounds, or devices containing single boundary containment of such. The sample tested meets the requirements of the specification listed however measurement uncertainty has not been analyzed to make a statement of conformance for destructive testing.

Page 1 of 1

Figure A10 Lab Report 10: Heavy Rail #6 - 24070239

WTTI
WWW.WTTI.COM

WELDER TRAINING AND TESTING INSTITUTE

1144 N. GRAHAM ST. · ALLENTOWN, PA 18109 · TEL 610-820-9551 · FAX 610-820-0271

LABORATORY TEST REPORT

LABORATORY TEST NUMBER: 24080089
COMPANY NAME: ESAB Welding & Cutting Products
IDENTIFICATION ON SAMPLE: Delivered Coupon Identified as LR5
MATERIAL SPECIFICATION: Delivered Material Identified as Unspecified Carbon Steel with Unspecified Overlay
DIMENSIONS: 0.650"
TYPE OF TEST: Test for Information Only

TENSILE TEST RESULTS
IAW TT-1, Current Revision

TEST DATE: 8/16/2024

MINIMUM TENSILE REQUIRED: Not Specified

SPECIMEN ID	WIDTH (in)	THICKNESS (in)	AREA (sq in)	TENSILE LOAD (lbs)	TENSILE STRENGTH (psi)	YIELD LOAD (lbs)	YIELD STRENGTH (psi)	ELONGATION (%)	LOCATION & TYPE OF FAILURE
1	0.5030	0.2515	0.1990	16,788	84,500	n/a	n/a	9.75	WM-Ductile

NOTES: Reduction of Area: 9.7%

FINAL RESULTS: INFO ONLY

TEST(S) CONDUCTED IN ACCORDANCE WITH: ASTM E8
TEST(S) CONDUCTED BY: KRG
REPORT DATE: 8/28/2024
APPROVED BY: Dennis T. Tobash CWI / WTTI

WTTI Job #: JOB35439

SIGNATURE:

QUALITY POLICY STATEMENT

ACCREDITED
TESTING CERT #3430.01

The services reported in this document were performed in accordance with Welder Training and Testing Institute's Quality System, governed by Quality Manual, Rev. 19, 1/4/23 and AWS Accredited Test Facility (Cert. #900201). WTTI is accredited by A2LA to ISO 17025 for the test methods listed on Testing Cert. 3430.01 and 3430.02. The Scope of Accreditation is available at www.wtti.com. This document shall not be modified or reproduced except in full, without written approval of the laboratory.
These recorded results represent only the specimen(s) tested and are in compliance with applicable code(s), standard(s), and/or contract requirement(s). At no point during testing or inspection at WTTI's facility has this item come into direct contact with mercury, mercury compounds, or devices containing single boundary containment of such. The sample tested meets the requirements of the specification listed however measurement uncertainty has not been analyzed to make a statement of conformance for destructive testing.

Page 1 of 1

Figure A11 Lab Report 11: Light Rail #5 - 24080089

WWW.WTTI.COM

WELDER TRAINING AND TESTING INSTITUTE

1144 N. GRAHAM ST. · ALLENTOWN, PA 18109 · TEL 610-820-9551 · FAX 610-820-0271

LABORATORY TEST REPORT

LABORATORY TEST NUMBER: 24080090
COMPANY NAME: ESAB Welding & Cutting Products
IDENTIFICATION ON SAMPLE: Delivered Coupon Identified as LR6
MATERIAL SPECIFICATION: Delivered Material Identified as Unspecified Carbon Steel with Unspecified Overlay
DIMENSIONS: 0.700"
TYPE OF TEST: Test for Information Only

TENSILE TEST RESULTS

IAW TT-1, Current Revision

TEST DATE: 8/16/2024

MINIMUM TENSILE REQUIRED: Not Specified

SPECIMEN ID	WIDTH (in)	THICKNESS (in)	AREA (sq in)	TENSILE LOAD (lbs)	TENSILE STRENGTH (psi)	YIELD LOAD (lbs)	YIELD STRENGTH (psi)	ELONGATION (%)	LOCATION & TYPE OF FAILURE
1	0.5020	0.2510	0.1980	26,862	136,000	22,600	114,000	1.5	WM-Ductile

NOTES: Reduction of Area: 2.2%

FINAL RESULTS: INFO ONLY

TEST(S) CONDUCTED IN ACCORDANCE WITH: ASTM E8
TEST(S) CONDUCTED BY: KRG
REPORT DATE: 8/28/2024
APPROVED BY: Dennis T. Tobash CWI / WTTI

WTTI Job #: JOB35439

SIGNATURE:

QUALITY POLICY STATEMENT

ACCREDITED
TESTING CERT #3430.01

The services reported in this document were performed in accordance with Welder Training and Testing Institute's Quality System, governed by Quality Manual, Rev. 19, 1/4/23 and AWS Accredited Test Facility (Cert. #900201). WTTI is accredited by A2LA to ISO 17025 for the test methods listed on Testing Cert. 3430.01 and 3430.02. The Scope of Accreditation is available at www.wtti.com. This document shall not be modified or reproduced except in full, without written approval of the laboratory.
These recorded results represent only the specimen(s) tested and are in compliance with applicable code(s), standard(s), and/or contract requirement(s). At no point during testing or inspection at WTTI's facility has this item come into direct contact with mercury, mercury compounds, or devices containing single boundary containment of such. The sample tested meets the requirements of the specification listed however measurement uncertainty has not been analyzed to make a statement of conformance for destructive testing.

Page 1 of 1

Figure A12 Lab Report 12: Light Rail #6 - 24080090

WWW.WTTI.COM

WELDER TRAINING AND TESTING INSTITUTE

1144 N. GRAHAM ST. · ALLENTOWN, PA 18109 · TEL 610-820-9551 · FAX 610-820-0271

LABORATORY TEST REPORT

LABORATORY TEST NUMBER: 24080456
COMPANY NAME: ESAB Welding & Cutting Products
IDENTIFICATION ON SAMPLE: Delivered Coupon Identified as LR7
MATERIAL SPECIFICATION: Delivered Material Identified as Unspecified Carbon Steel with Unspecified Overlay
DIMENSIONS: 0.750"
TYPE OF TEST: Test for Information Only

TENSILE TEST RESULTS
IAW TT-1, Current Revision

TEST DATE: 9/11/2024

MINIMUM TENSILE REQUIRED: Not Specified

SPECIMEN ID	OD (in)	THICKNESS (in)	AREA (sq in)	TENSILE LOAD (lbs)	TENSILE STRENGTH (psi)	YIELD LOAD (lbs)	YIELD STRENGTH (psi)	ELONGATION (%)	LOCATION & TYPE OF FAILURE
1	0.3530	0.1765	0.0979	8,433	86,200	1,120	11,500	0.293	BM-Ductile

NOTES: Reduction of Area: 0.5%

FINAL RESULTS: INFO ONLY

TEST(S) CONDUCTED IN ACCORDANCE WITH: ASTM E8
TEST(S) CONDUCTED BY: KRG
REPORT DATE: 9/11/2024
APPROVED BY: Dennis T. Tobash CWI / WTTI

WTTI Job #: JOB35674

SIGNATURE:

ACCREDITED
TESTING CERT #3430.01

QUALITY POLICY STATEMENT

The services reported in this document were performed in accordance with Welder Training and Testing Institute's Quality System, governed by Quality Manual, Rev. 19, 1/4/23 and AWS Accredited Test Facility (Cert. #900201). WTTI is accredited by A2LA to ISO 17025 for the test methods listed on Testing Cert. 3430.01 and 3430.02. The Scope of Accreditation is available at www.wtti.com. This document shall not be modified or reproduced except in full, without written approval of the laboratory.
These recorded results represent only the specimen(s) tested and are in compliance with applicable code(s), standard(s), and/or contract requirement(s). At no point during testing or inspection at WTTI's facility has this item come into direct contact with mercury, mercury compounds, or devices containing single boundary containment of such. The sample tested meets the requirements of the specification listed however measurement uncertainty has not been analyzed to make a statement of conformance for destructive testing.

Page 1 of 1

Figure A13 Lab Report 13: Light Rail #8

ESAB

Micro/Macro-Hardness Test Report

Date: 26-06-2024
Tester: Francis LeClaire
Program: UNLV Light Rail 4
Job: Test job # 1

Job data

Mean	Minimum	Maximum	Range	Std. deviation
415.2	275.0	485.3	210.3	70.8

Hardness Trace

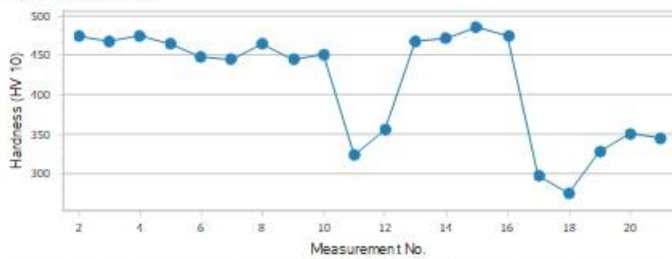

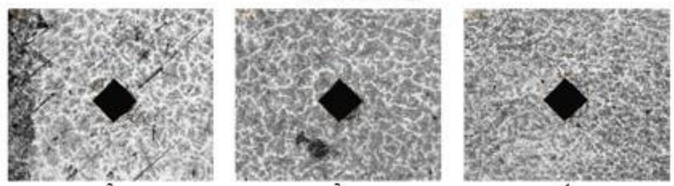

2 3 4

Wilson www.buehler.com Page 1 of 4

Figure A14 Lab Report 14: Hardness Test

UNLV Rail Project

ThermaClad 446 Wire

5/29/2024

	Heavy Rail-SubArc DCEP	**Converted**	**Specification**
Ultimate Tensile Strength (psi)	137,000	944.6 N/mm2	980 N/mm^2 Minimum (980MPa)
Yield Strength (psi)	122,000	841.2 N/mm2	511 N/mm^2 Minimum (830MPa)
% Elongation	2.60	2.6	10% minimum
% Reduction of Area	0.395	0.395	None
		Converted Avg.	
Microhardness HV10-Layer 5	389.4, 402.8	378	310 HB min (318Hv)
Microhardness HV10-Layer 4	394.7, 389.4	375	310 HB min
Microhardness HV10-Layer 3	422.9, 417.0	399	310 HB min
Microhardness HV10-Layer 2	461.2, 465.3	435	310 HB min
Microhardness HV10-Layer 1	584.7, 552.3	514	310 HB min

Figure A15 Lab Report 15: Heavy Rail strength and hardness

Figure 16 Lab Report 16: Printing zone 1

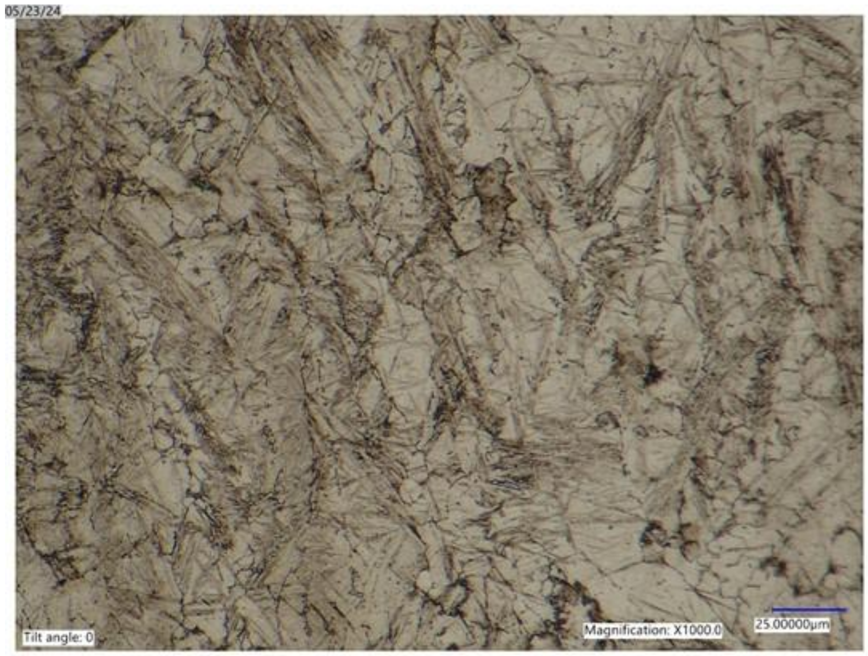

Figure A17 Lab Report 17: Printing zone 2

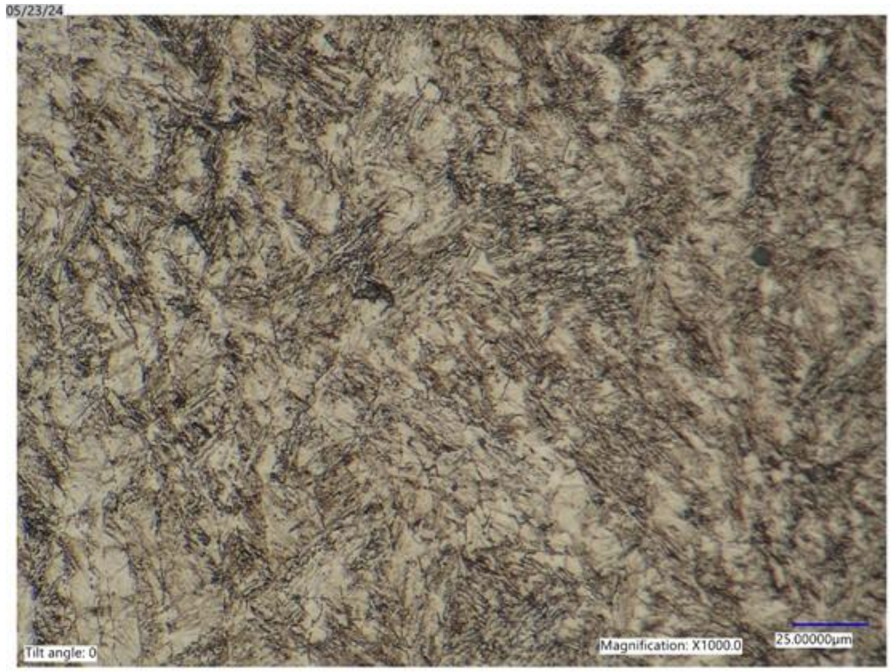

Figure A18 Lab Report 18: Printing zone 3

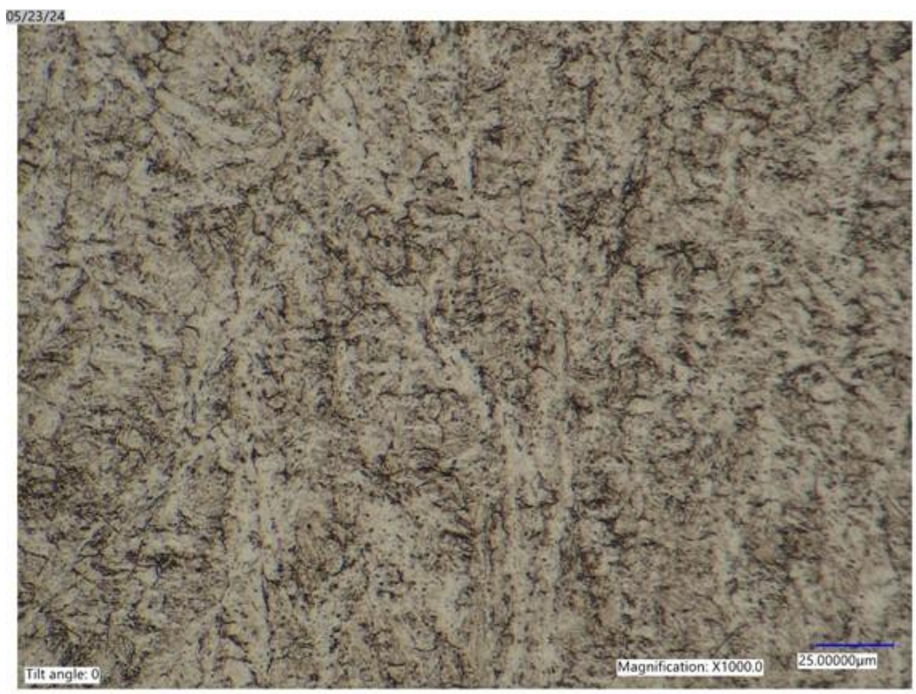

Figure 19 Lab Report 19: Printing zone 4

Figure 20 Lab Report 20: Printing zone 5

ACKNOWLEDGEMENTS

This study was conducted with the support from the USDOT Tier 1 University Transportation Center on Railroad Sustainability and Durability.

ABOUT THE AUTHOR

Mr. Ershad Mortazavian was a graduate student when he worked on this project. He has his master's and bachelor's degrees in mechanical engineering from the University of Kashan and University of Kashan, respectively.

Mr. Arman Ali Mohammadi was a graduate student when he worked on this project. He obtained his master's and bachelor's degrees in mechanical engineering from the University of Tehran and Isfahan University of Technology, respectively.

Dr. Zhiyong Wang is an associate professor in the Department of Mechanical Engineering at the University of Nevada, Las Vegas. His research interests include 3D printing heavy metals and bio materials, advanced material manufacturing, and CVD process for mono crystal materials. He has a Ph.D. in mechanical engineering from the Harbin Institute of Technology.

Dr. Hualiang (Harry) Teng is a professor in the Department of Civil and Environmental Engineering and construction. His expertise includes railroad engineering and management, intelligent transportation systems, highway safety, and air quality analysis. He was the director of the Railroad University Transportation University at UNLV.